ISSN 2683-9288

Science Reviews from the end of the world

Volume 2
Number 3
October 2023

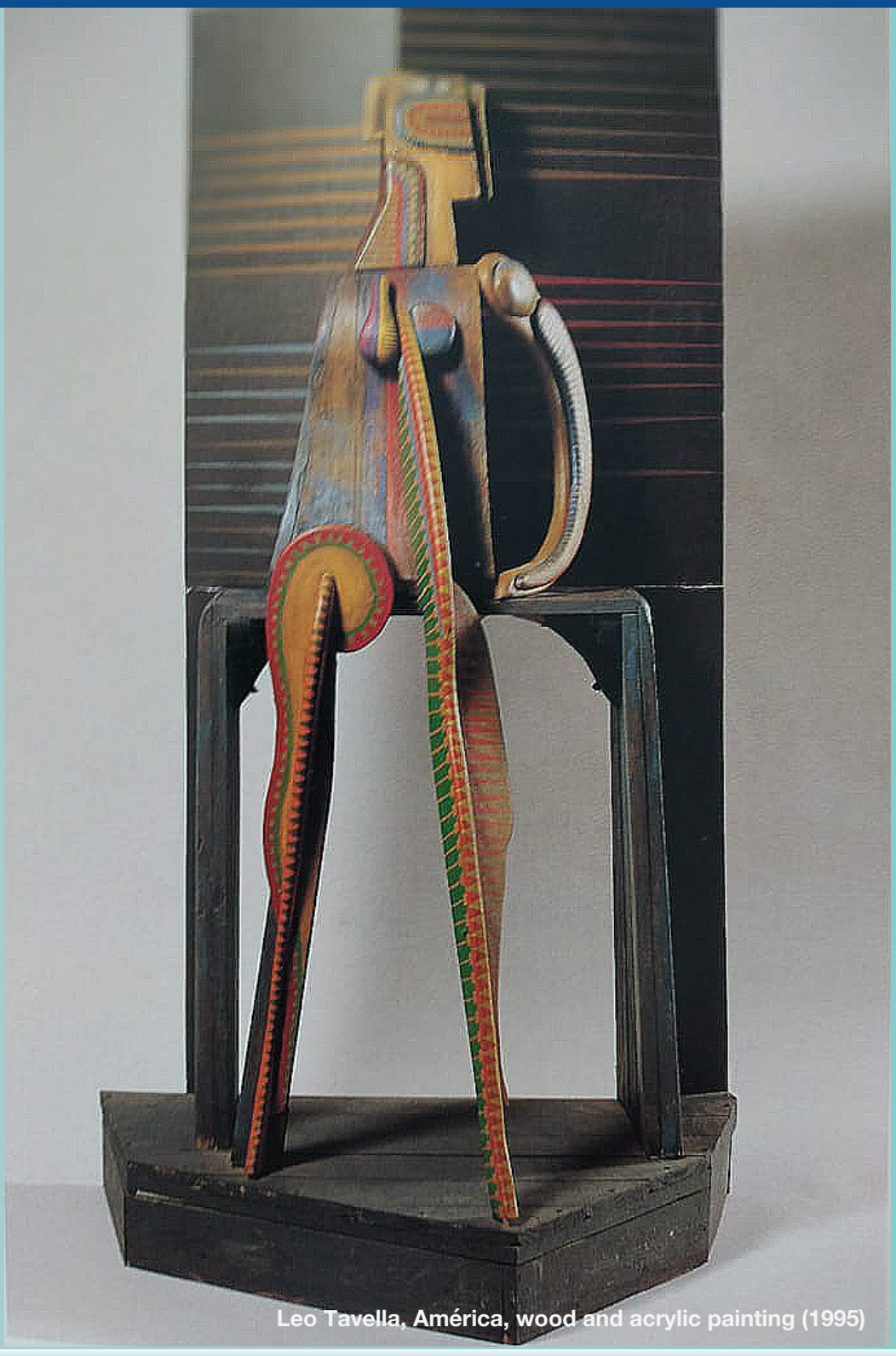

Leo Tavella, América, wood and acrylic painting (1995)

Science Reviews
from the end of the world

Science Reviews - from the end of the world **is a quarterly publication that aims at providing authoritative reviews on hot research topics developed mainly by scientists that carry out their work far away from the main centers of science. Its research reviews are short, concise, critical and easy-reading articles describing the state of the art on a chosen hot topic, with focus on the research carried out by the authors of the article. These articles are commissioned by invitation and are accessible not only to hardcore specialists, but also to a wider readership of researchers interested in learning about the state-of-the-art in the reviewed subject. The reviews cover all fields of science and are written exclusively in English. They are refereed by peers of international prestige and the evaluation process follows standard international procedures.**

Centro de Estudios sobre Ciencia, Desarrollo y Educación Superior
538 Pueyrredón Av. - 2° C – Second building
Buenos Aires, Argentina - C1032ABS
(54 11) 4963-7878/8811
sciencereviews@centroredes.org.ar
www.scirevfew.net

Vol. 2, No. 3
October 2023

ISSN 2683-9288

Leo Tavella, América, wood and acrylic painting (1995). Exposición Permanente de Artistas Plásticos con la Ciencia, Comisión Nacional de Energía Atómica, Centro Atómico Constituyentes (By permission).

Science Reviews
from the end of the world

Table of Contents

INTRODUCTION

IN THIS ISSUE

ARTICLES

INSTRUCTIONS FOR AUTHORS

Science Reviews
from the end of the world

Vol. 2, No. 3, October 2023 //

EDITORIAL

Encuentro de Superficies y Materiales Nanoestructurados - NANO 2022: An open window to the last news in nanotechnology applications

With more than two decades of existence, the "Encuentro de Superficies y Materiales Nanoestructurados" remains a national benchmark for the scientific and technological prowess of Argentina's "Nano" community. The event began in 2001 at the National Atomic Energy Commission in Bariloche and developed into what it is today: on the one hand, a national gathering that brings together a wide range of disciplines to discuss and disseminate the most recent findings in nanoscience and nanotechnology; on the other hand, a place where friends and colleagues can talk freely and honestly about a wide range of topics related to research, management, transfer to industry, and education in this vibrant field of science and technology. The event took place in San Carlos de Bariloche until 2010. Following then, it was held in Córdoba (2012), Mar del Plata (2013), Bariloche (2014), Rosario (2015), Buenos Aires (2016), Bariloche (2017), La Plata (2018), Buenos Aires (2019), and Mar del Plata (virtual in 2021). The National University of Río Cuarto, along with participants from the CONICET-UNRC institutes IITEMA, IDAS, and INBIAS, organized NANO 2022 during August 9–11, 2022. The great supervision work of the coordinator of the meeting, Dr. María Molina and the efforts of teachers, researchers, and students belonging to the organizing committee were reflected in the wonderful group of representatives of the academic, scientific, and productive sectors gathered to discuss the challenges and advances in the different areas of Nanoscience and Nanotechnology. Various research fields, including self-assembly and synthesis of nanomaterials, micro and nanofabrication, surfaces, condensed matter physics, nano-bio interfaces and biological processes, and optical, electrical, and magnetic properties, were represented among the speakers at the meeting. In this issue, thanks to the organizing committee and the generosity of the outstanding speakers who attended, we have five papers from this event that provide a broad and interesting overview of what the meeting was and will continue to be for the entire country. These papers highlight the novelty, depth, rigor, and impact of the work being done by all the national institutes that are dedicated to this fascinating and transversal field of knowledge, as well as the sharing of experiences and challenges and the establishment of new cooperation programs and training opportunities for young professionals. In closing, I would like to invite you to keep taking part in this event in upcoming editions and to thoroughly enjoy these great and inspirational lectures.

Cristina Hoppe

Mar del Plata, October 2023

Bio

Cristina Hoppe

Was born in Buenos Aires, Argentina, in 1975. She graduated in Chemistry (2000) at the University of Mar del Plata, where she also received her Ph.D. in Materials Science (2004) working on polymer dispersed liquid crystals (PDLC) under the supervision of Prof. Roberto J. J. Williams (Institute of Materials Science and Technology, INTEMA, UNMdP/CONICET). In 2004 she was awarded a Postdoctoral Antorchas fellowship and she moved to the University of Santiago de Compostela (Nanotechnology and Magnetism group), Spain, where she worked with Prof. Arturo López Quintela in the synthesis and characterization of metal and oxide nanoparticles. After one year she was awarded a Marie Curie European Postdoctoral Fellowship (International Incoming Fellowship, 6th framework Programm) to work

in the arrangement of nanoparticles in polymer multiphasic systems. She returned to Argentina in December 2007.

She is currently working at INTEMA (Polímeros Nanoestructurados group) as staff researcher (Investigadora Principal de CONICET). She has leaded several research projects in the field of polymer materials and nanomaterials, including the Argentinian node of a four-year European mobility project in vitrimers (Project VIT, RISE call from the EU started on September 2021). She has been working on the design of vitrimers, covering topics ranging from the design and chemistry of the networks to their rheological and technological properties related to self-healing, shape memory and recycling capacity. She has also participated as Argentina representative in international cooperation official missions to USA, Portugal, Italy, Mexico and South Africa in the framework of I+D cooperation agreements in Nanoscience and Nanotechnology. Her main research interests are related with the design and application of functional polymers and nanocomposites.

IN THIS ISSUE

Science Reviews
from the end of the world

Vol. 2, No. 3, October 2023 // pp. 7-20 /

Fe-based high-temperature superconductivity: Impact of atomic defects in the electronic states

Yanina Fasano[1, 2, 3]

[1] Instituto de Nanociencia y Nanotecnología, CNEA and CONICET,
Nodo Bariloche, Avenida Bustillo 9500, 8400 Bariloche, Argentina
[2] Centro Atómico Bariloche and Instituto Balseiro,
CNEA and Universidad Nacional de Cuyo, Avenida Bustillo 9500, 8400 Bariloche, Argentina
[3] Leibniz Institute for Solid State and Materials Research, Helmholtzstraße 20, 01069 Dresden, Germany (Dated: January 19, 2023)

E-mail: yanina.fasano@cab.cnea.gov.ar

Abstract

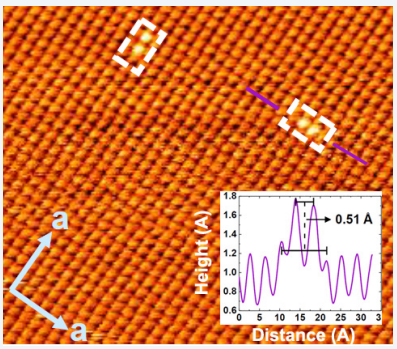

A brief review on the impact of atomic defects in the electronic properties of Fe-based super conductors is hereby presented, focusing in particular on the FeSe family of superconductors. This family of compounds captured the attention of the scientific community during the last decade since its simple crystal structure seemed to be an advantage in understanding the microscopic mechanisms mediating high-temperature superconductivity in Fe-based superconductors. Now, more than 14 years of intense research around the world have elapsed since the discovery of the so-called iron age of superconductivity, and nevertheless it is still debated which is the origin of superconductivity in these compounds. One thing stands for certain in all the enquiries: There is a subtle interplay between defects or local variations in the crystal structure and the electronic states in Fe-based superconductors. This review presents an overview on the main contributions of the community in this interplay in the particular case of the FeSe family and provides a critical discussion on some of the points that still need to be studied in order to provide a thorough quantitative understanding of this issue.

Keywords: Fe-based superconductors; electronic states; atomic defects

I. Introduction

The first family of high-temperature superconductors was revealed back in 1986[1–3] and very rapidly several cuprate compounds with critical temperatures exceeding the boiling point of nitrogen were discovered.[4,5] For 15 years subsequent to this discovery, these family of complex oxides of copper seemed to be the only high-temperature superconductors. However, 2008 witnessed the advent of the so-called iron-age of high temperature superconductivity.[6] The Fe-based pnictides and chalcogenides are thus the second family of un conventional high-temperature superconductors that renewed the hopes on discovering materials with technically relevant critical temperatures. Superconductivity with a critical temperature of $T_c = 26$ K was first reported in the $LaO_{1-x}F_xFeAs$[6] and was followed by numerous reports in several members of the Fe-based superconductors family.[7–11] Within this family, iron chalcogenides, and particularly the 11 phase material FeSe,[7] has attracted much attention due to its simple crystal structure of stacks of superconducting layers. Within these layers, a square/tetrahedral planar lattice of Fe cations are tetrahedrally coordinated with Se atoms located above and below the plane at a distance z_{Se}, see Fig. 1 (a). This compound is also considered as the prototype for studying the origin of unconventional super conductivity in the whole Fe-based superconductors fam ily.[12]

FeSe is also special since it puzzles the identification of the microscopic mechanisms giving rise to high temperature superconductivity in the Fe-based family. Most of the compounds of this family develops a magnetic order apparently connected to the emergence of superconductivity.[12,13] However, FeSe presents no static magnetic order at ambient pressure.[13–15] This compound also undergoes a tetragonal-to-orthorhombic transition on cooling around $T_s \sim 90$ K[16] without presenting any magnetic transition.[17,18] This transition is also considered a nematic transition since the C4 symmetry of the crystal structure and of the electronic properties are both broken at T_s.[19] In addition, applying pressure or doping FeSe with chalcogen atoms alters significantly the phase diagram[20] and enhances magnetic instability.[21] Indeed, the idea that spin fluctuations have a relevant role in the superconducting pairing mechanism of Fe-based superconductors is suggested by spectroscopic information provided by scanning tunneling microscopy (STM).[22–24] Then, in the paradigmatic material FeSe the crystal structure and electronic properties such as superconductivity and magnetism are tightly enmeshed.

In the quest for enhancing the T_c of Fe-based super conductors, FeSe provided valuable information. In its pristine form, FeSe has a T_c of 8 K, but it can be enhanced up to 37 K by applying hydrostatic pressure,[25,26] or up to 30 K by intercalation of alkali metals between the layers.[27] For instance, Fig. 1 (b) shows the increase of T_c with hydrostatic pressure reported in Ref. 26. These enhanced critical temperatures in FeSe are within the largest values for binary superconducting compounds in general. In addition, there has been a considerable amount of work in many pnictogen and chalcogen sys tems in order to find a correlation between T_c and the Fe anion height.[28] All these efforts revealed that there exists an optimum value of the Fe-anion height of $_{\sim 1.38}$ Å that maximizes the T_c for many compounds of the Fe-based superconductors as shown in Fig. 1 (c) and discussed in detail in Ref. 28 Thus, the value of the Fe-anion height is a critical parameter in order to tune T_c.

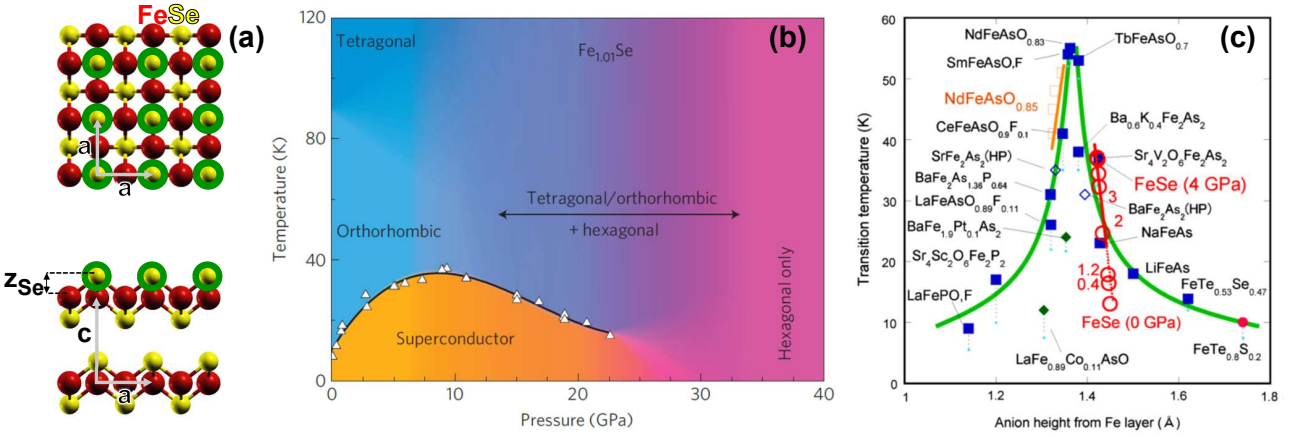

Figure 1. (a) Schematic representation of the FeSe crystal structure in the tetragonal phase at $T > 90$ K. The $a = 3.77$ Å and $c = 5.52$ Å unit cell vectors as well as the Fe-anion height z_{Se} are indicated. Reprinted from 43. (b) Evolution of the critical temperature (white points) and the electronic phase diagram of FeSe with hydrostatic pressure. The highest value of $T_c = 36.7$ K is reached at a pressure of 8.9 GPa. For no applied pressure the compound undergoes a tetragonal-to-orthorhombic transition on cooling through 90 K. Reprinted from 26. (c) Variation of T_c with the Fe-anion height for several compounds of the Fe-based superconductors family. Data for the paradigmatic FeSe compound are shown in open red circles and labelled with the value of the applied hydrostatic pressure between 0 and 4 GPa. Color points correspond to T_c values for several compounds as labelled. Full points are measured at ambient pressure whereas open points are measured at the optimal pressure (tiny diamonds) and at high pressures (open squares). Reprinted from 28.

In real samples, local crystal deformations and atomic scale defects are unavoidably present. If these deformations and defects entail local variations of z_{Se}, then a significant impact in the critical temperature and electronic states of the compounds is expected. In addition, the crystal structure deformations induced by introducing chemical pressure in the material by isovalently substituting Se with another chalcogen element[29] also affect the critical temperature of the compounds.[20] A remark able example on how crystal structure and electronic properties are finely intertwined in FeSe is the important enhancement of T_c when growing strained mono layer films on top of $SrTiO_3$ substrates[30], or when coating the samples with K adatoms.[31] Thus, understanding the impact of atomic-scale defects and deformations in the electronic structure of Fe-based superconductors is of key importance for assessing how critical is the occurrence of these features for the establishment of superconductivity in these compounds.

In addition, understanding their identity is fundamental to try to develop an engineering of superconducting/non-superconducting regions in Fe-based superconductors for nanoscale applied devices. Furthermore, a precise local control

of the location of atomic-scale defects would allow the tuning of electronic properties of the materials for applications as for instance achieved in other condensed matter systems such as in the case of dopants in semiconductors[32] and silicon.[33] From a more general perspective, atomic defects in Fe based superconductors are determinant in the control of their critical temperature[6,34] and the enhancement of their critical current by increasing vortex pinning.[35,36] Local atomic defects in Fe-based superconductors can also be used as probes for testing the possible pairing symmetry in these compounds.[37]

Here we review some of the most prominent experimental evidences on the impact of atomic-scale defects in the electronic properties of Fe-based superconductors focusing on compounds of the simplest FeSe family. Data available in the literature for this family is revisited and a recent experimental approach applied to obtain complementary atomic-scale and nanometer-thick bulk in formation on the topic is finally presented. Section II presents a critical discussion on the previous atomic-scale evidence from STM data in FeSe compounds. Section III overviews the findings obtained in an end-of-the-world research center on how the atomic-scale defects affect the bulk electronic core states by combining STM and XPS measurements. Finally, the Section IV is devoted to the conclusions and open questions on the topic with the aim of identifying the particular issues that deserve to be studied in order to better quantify how the un avoidable presence of atomic scales defects in Fe-based superconductors tailor its electronic properties and may eventually lead to locally or globally spoiling superconductivity in these compounds.

II. Previous atomic-scale evidence from STM data in FeSe

There is plenty of evidence obtained with scanning tunnelling microscopy (STM) that atomic-scale crystal structure modifications such as defects do play a role in the electronic and superconducting properties of materials.[38,39] The scanning tunnelling microscope is a suitable tool to study these issues since it probes the electronic density of states in real space with atomic spatial resolution. In a STM experiment the spatially-mapped tunnel current is proportional to the convolution of the local density of states of the sample and the tip, and to an exponential multiplicative term that grows with decreasing the tip-sample distance.[38] Topographic images acquired either at constant height or current are proportional to the integration of the local density of states of the sample up to the regulation voltage as well as to the mentioned exponential factor,[38] and thus brighter features where the tunnel current is larger result from a region with a larger apparent height and/or a larger local density of states. Measuring a larger local density of states can arise from a local electronic inhomogeneity with an inherent larger value of this magnitude and/or from a protrusion of the local electronic clouds towards the STM tip that results in a smaller tip-sample distance.

One of the first works reporting on the impact of atomic defects in the superconducting properties of Fe based superconductors was published with the main aim of studying the thickness-dependence of the T_c of FeSe films grown by molecular beam epitaxy (MBE) on top of bilayer graphene substrates.[40] The authors find that T_c scales inversely with the film thickness and that a superconducting gap is detected in in-situ STM measurements for the thinnest studied film made of two c-axis unit cells of FeSe. The work presents a study on how the temperature of the substrate during the growing is determinant for the films being superconducting: Only when this temperature is larger than 420 C the films present a superconducting phase. Figure 2 shows examples of atomic-resolution STM topographies of non superconducting (a) and superconducting (b) FeSe films grown in bilayer graphene substrates kept at 390 and 450 C, respectively, during the MBE growing process. In these images each round-like brighter spot corresponds to an apical Se atom located above the Fe plane (atoms highlighted in green in Fig. 1). The films grown with a substrate temperature larger than 420 C present a depletion of the STM-measured tunneling conductance at low temperatures, even for films with a thickness $d = 2$ c-axis unit cells, see Fig. 2 (d). This tunneling conductance is proportional to the local density of states of the system and its depletion around zero bias is a manifestation of a finite superconducting gap that inhibits the tunneling of electrons from the sample to the tip since they are bounded in superconducting Cooper pairs. On increasing temperature this depletion fills in and disappears at the critical temperature T_c as expected for a superconducting material.

On addition to these findings on the optimization of the growing conditions for having superconducting very thin FeSe films, this work also presents evidence on the dramatic impact of dumbbell-type atomic defects on super conductivity. A dumbbell defect is observed as a brighter pair of contiguous Se atoms, as for instance clearly visible in the topography of the FeSe film shown in Fig. 2 (a). This type of defects was ubiquitously observed in sub sequent works applying STM in FeSe films and crystals.[29,37,41–43] The authors of this work do not investigate via first principle calculations on the nature of these defects, but they only speculate that they are associated to excess Se. Nevertheless, they show that the density of dumbbell defects can be controlled by the growing conditions of the film and by subsequent annealing at high temperatures. More importantly, they report that no depletion of the tunnelling conductance is detected for FeSe films presenting a concentration of dumbbell defects at the surface larger than 2.5 %. Further support to this statement is invoked from previous evidence obtained in thicker MBE-grown FeSe films within the same research group.[19] Thus, in the case of very thin FeSe films super conductivity is spoiled on increasing the dumbbell defect concentration above a relatively low critical value.

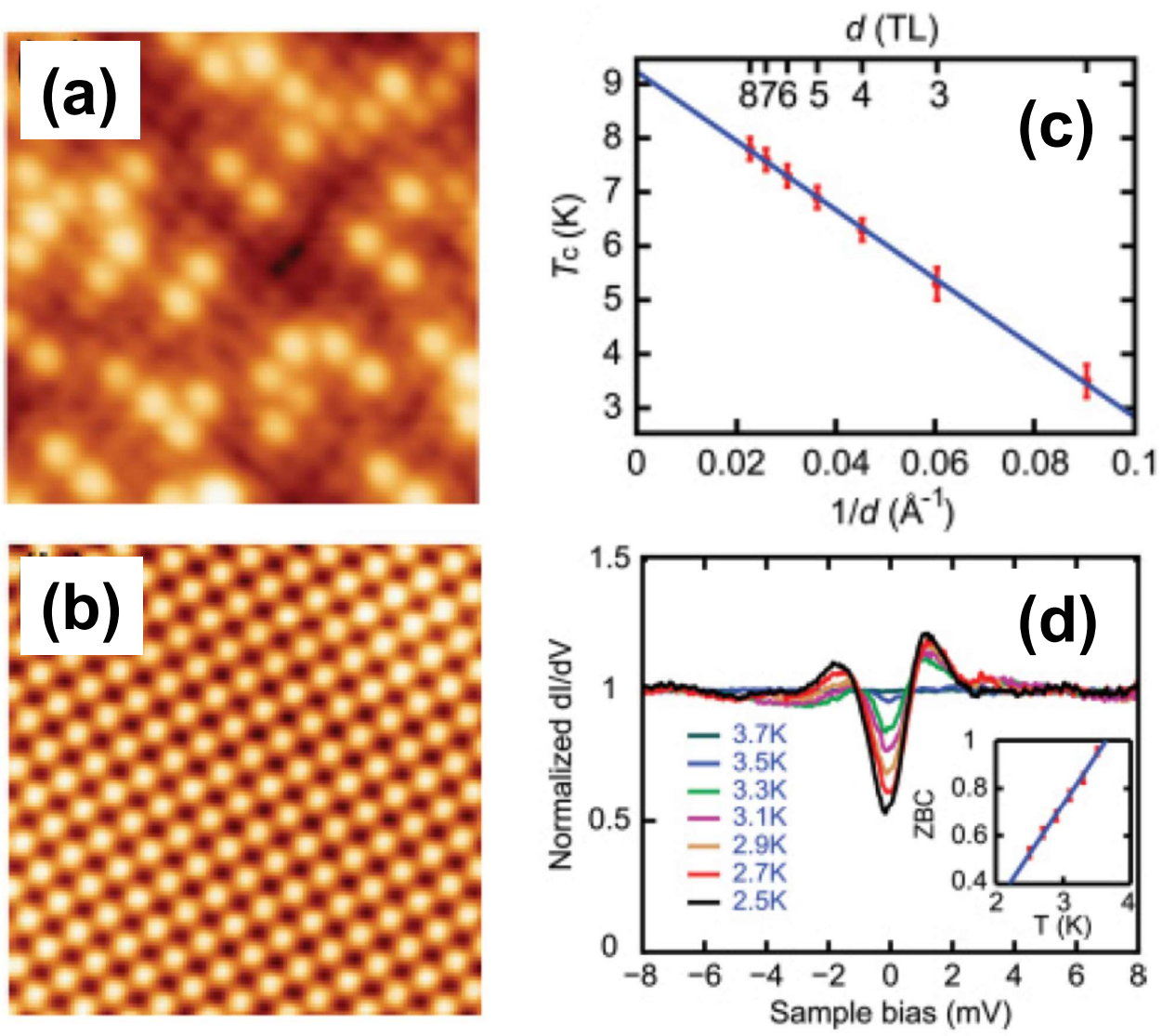

Figure 2. Atomic-resolution STM topographies of the surface of FeSe films grown by MBE at substrate temperatures of (a) 390 and (b) 450 C. The images survey an area of 5 × 5 nm^2. Brighter atomic sites in (a) are associated to dumbbell defects in the crystal structure. (c) Inverse dependence of the critical temperature T_c with the film thickness d in units of c-axis unit cells (TL). (d) Normalized tunneling conductance curves at various temperatures for the thinnest film with d = 2 c-axis unit cells. The depletion of the tunnel conductance associated to the superconducting gap as well as the coherence peaks are observed up to 3.7, K. Insert: On increasing temperature within the superconducting phase the zero-bias conductance ZBC enhances. Reprinted from 40.

The nature of dumbbell defects was later studied in an experimental and theoretical work also studying MBE grown FeSe films.[41] By conducting a STM and an exhaustive first-principles theoretical investigation of candidate defect configurations the authors of this work show that the dumbbell defects are induced by a vacancy in the site of Fe located below the two brighter Se atoms detected in topographies. By means of a density functional theory (DFT) analysis of the formation energies of different types of defects, this work shows that this is the most energetically favorable defect, overthrowing previous spec ulations[19,40] of the dumbbell defects being associated to Se adsorbates or substitutions. In addition, they use STM to identify and estimate the defect concentration and compare the results with the DFT simulations in order to characterize the local electronic modifications entailed in these defects. Furthermore, this work studies experimentally and theoretically the previously reported removal and ordering of Fe vacancies (dumbbell defects) via annealing. Even though the authors resolve the chemical identity of these defects, they do not shed light on the question on how a large concentration of defects destroy superconductivity in FeSe films.

Figure 3 summarizes the main results obtained in the work of Huang *et al.*[41] that are relevant for characterizing the chemical nature of dumbbell defects and some hints on their impact on the local electronic properties of superconducting FeSe. As in previous works,[19,40] dumb bell defects in the studied FeSe films are observed as pairs of brighter Se atoms in atomic-resolution STM topographies of the surface. The studied FeSe films have thick nesses of a few c-axis unit cells and are grown by MBE on two different substrates, SiC and $SrTiO_3$. For example, Fig. 3 (a) shows a topographic image measured in the orthorhombic phase (84 K) of a few-layer-thick film grown on SiC. This as grown surface presents a notice able density of pairs of brighter Se atoms associated to dumbbell defects. These defects can be removed by annealing, as observed in Fig. 3 (b) that shows a topography of the same film presented in (a) after annealing at 450 C for 2.5 h. By performing nudged elastic band calculations and 2D random walk simulations the authors of this work explain this effect showing that during vacuum annealing the Fe vacancies can diffuse to the edge of the atomic terraces and thus in the main part of the terraces the dumbbell defect density is reduced. Since the Fe vacancy site can be located in a site where a pair of Se atoms at the top layer is aligned along the a-axis or else in a site such that the pair of Se atoms is aligned along the b-axis, see Fig. 1 (a), dumbbell defects appear aligned in both crystal directions, as indicated with orange and yellow lines in Fig. 3 (c).

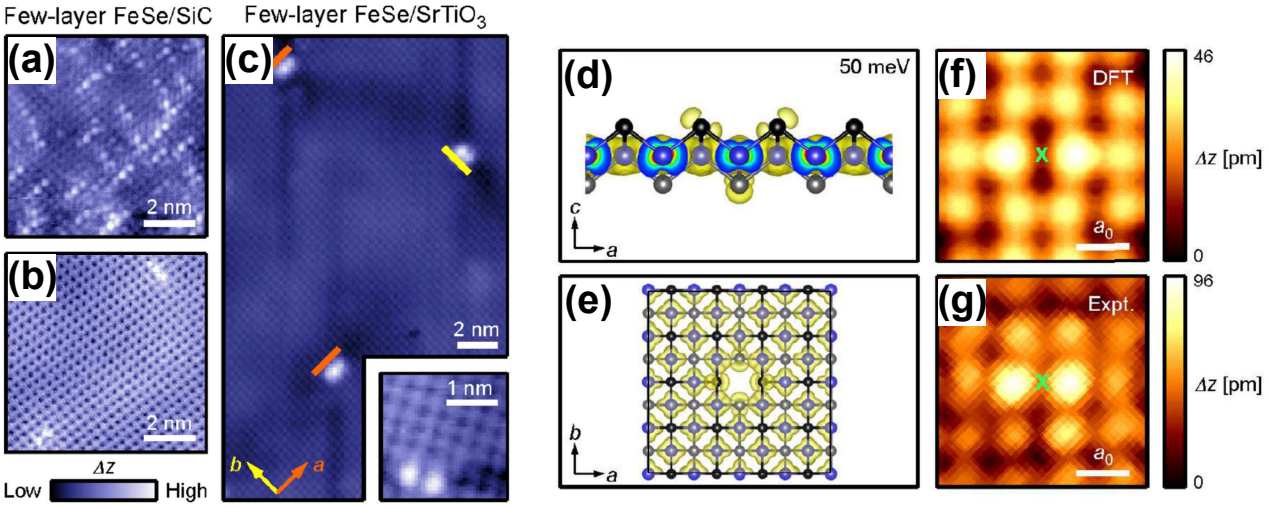

Figure 3. Dumbbell defects observed as pairs of brighter Se atoms in atomic-resolution STM topographies of the surface of FeSe films with thickness of few c-axis unit cells grown by MBE on different substrates. (a) Film grown on SiC measured at 84 K. (b) Topographic image obtained in the same film after annealing at 450 C during 2.5 h. (c) Film grown on $SrTiO_3$ and measured at ~ 6 K. Orange and yellow lines indicate the two possible orientations of dumbbell defects, parallel to the a and b unit cell vectors of the FeSe orthorhombic structure.(d) Charge density isosurface obtained with DFT simulations of bilayer FeSe in the c - a plane in the vicinity of a dumbbell defect induced by an Fe vacancy. Se atoms are shown in blue whereas Fe atoms are black. The electronic clouds associated to every atom are highlighted in yellow. The protrusion towards outside of the surface of the electronic clouds of the Se atoms adjacent to the Fe vacancy is evident. Image obtained integrating the density of states from the Fermi energy up to 50 meV. (e) Same calculation than in (d) but plotted in the a - b plane where the Fe vacancy producing the dumbbell defect is more clearly observed. (f) Topography obtained from the same simulations in the vicinity of the Fe vacancy indicated with a green cross. The neighbor Se atoms of the top surface show the brighter lobes producing the dumbbell signature. (g) Experimental STM topography of a single-layer FeSe film grown on $SrTiO_3$ in the neighborhood of a dumbbell defect. Reprinted from 41.

By modelling the local density of states of FeSe with DFT calculations the authors of this work[41] provide important evidence on how the Fe vacancy perturbs the electronic cloud of the neighboring Se sites and thus produce the dumbbell signature imaged by STM. Figure 3 (d) depicts the charge density isosurface obtained with DFT simulations of a slab of FeSe in the c - a plane in the vicinity of a dumbbell defect. In this figure Se atoms are shown in blue whereas Fe atoms are black. The electronic clouds associated to every atom are highlighted in yellow. The Se atoms adjacent to the Fe vacancy present electronic clouds with a protrusion towards outside of the surface. Figure 3 (e) shows the result of the same calculation but plotted in the a - b plane where the Fe vacancy producing the dumbbell defect is more clearly observed. When measuring with an STM tip this spatial orientation of the electronic cloud of a pair of Se atoms will produce an enhancement of the tunnelling current since due to the protrusion of their orbitals the effective tip sample distance is smaller at atomic scale. This results in the pair of Se atoms adjacent to the Fe vacancy be ing observed as brighter than the rest. This explanation is further supported by the topographic image obtained from the same simulations in the vicinity

of the Fe vacancy indicated with a green cross in Fig. 3 (f). The neighbor Se atoms of the top surface show the brighter lobes producing the dumbbell signature. This simulated topography is in excellent agreement with the experimental STM topographies measured in the neighborhood of dumbbell defects observed in several FeSe films, as for example the one of Fig. 3 (g) corresponding to a single layer film grown on $SrTiO_3$. Whether the apical distance between the Se atoms and the Fe plane in the vicinity of a dumbbell defect is affected is not discussed in Ref. 41. In order to perform this study, DFT simulations should take into account the van der Waals interaction between adjacent Se and Fe planes as well as the correct magnetic order of Fe atoms in the FeSe material. These two issues were not considered in the work of Huang *et al*. Their consideration is of critical importance in order to have quantitative information on how atomic-scale dumbbell defects affect the local superconducting properties of the material.

Regarding this issue, phenomenological information was later provided by means of STM spectroscopy measurements with atomic resolution in the superconducting phase of FeSe single crystals.[37] In this work, the authors measure with atomic resolution the local density of states in the vicinity of dumbbell defects. In a superconducting material, the *dI/dV* tunnelling conductance measured by STM, proportional to the local density of states of the quasiparticle excitation spectrum, presents a depletion between energies ±Δ around the Fermi level. This depletion is flanked by two coherence peaks located at energies around the superconducting gap for which the number of electrons tunnelling from the sample to the tip is maximized since this energy is around the value Δ re quired to break the superconducting Cooper pairs of electrons. Thus, the energy location of the coherence peaks in *dI/dV* STM curves is of the order of the superconduct ing gap. Conventional superconductors are expected to present symmetric peaks with the same height for occupied and empty sample states. Nevertheless, many materials present asymmetric *dI/dV* spectra produced by an asymmetry in the hole and electron bands of the materials,[44] as is for instance the case in FeSe according to angle/resolved photoemission spectroscopy data.[20] In the case of the spectra measured in FeSe crystals in Ref. 37, both away and close to the dumbbell defects the coherence peaks are asymmetric, see panels (c) and (d) of Fig. 4. In regions far away of the dumbbell defects, $\Delta \sim 2$ meV consistent with a $T_c = 0.46\Delta/k_B \sim 8$ K according to the BCS ratio for conventional superconductors. In contrast, on the sites of the Se atoms the peaks at 2 meV broaden and two extra peaks are detected at energies smaller than the superconducting gap, see Fig. 4 (d). These asymmetric peaks are rather sharp, sharper than what remains of the peaks at 2 meV, and are detected around 0.6 meV. The authors of this work state that these peaks located at smaller energies are bound states inside the superconducting gap. They perform DFT simulations in a slab of FeSe considering an Fe vacancy and show that the dumbbell defect is non-magnetic. Then they use this result to claim that the in-gap bound states emerging from a nonmagnetic defect-induced pair breaking suggest a sign-changing pairing state in FeSe.

Even though this can be concluded from the spin polarized DFT calculations presented in Ref. 37, as the same authors mention in the paper, they can not rule out the possibility that the in-gap coherence peaks in the vicinity of a dumbbell results from the spatial super imposition of the tunnelling response at the defect and the superconducting bulk. ON top of this possibility, I consider that the in-gap peaks can also have another origin due to technical issues of the STM measurements. In particular, even though the images of Fig. 4 have atomic resolution, since the image is not focused in the dumbbell region with high spatial resolution, and has a size larger than 20 times the area of the defect, it might be that the local *dI/dV* curves are collecting electrons tunnelling from the neighbor Se atomic sites that are not affected by the dumbbell defect. In order to discard this possibility, spectroscopic images with finer spatial resolution in the sub lattice spacing range are required. This information is not presented in Ref. 37. Thus, as the same authors mention, due to technical reasons of the STM technique, it is also quite likely that the extra in-gap peaks can be interpreted as due to a partial suppression of superconductivity at the defect site. This is consistent with coherence peaks located at smaller energies since that will yield a $\Delta \propto T_c$ smaller and then a local depletion of the superconducting critical temperature within the dumb bell. On top of STM data with finer and high spatial resolution in the vicinity of the dumbbell, more realistic DFT calculations than the ones presented in Refs. 37 and 41 are required to clarify this issue. In particular, these simulations should search for the possibility of the apical Se height being reduced in the vicinity of the dumbbell defect which will be in agreement with a reduction of T_c as ubiquitously observed in many Fe-based superconductors.[28]

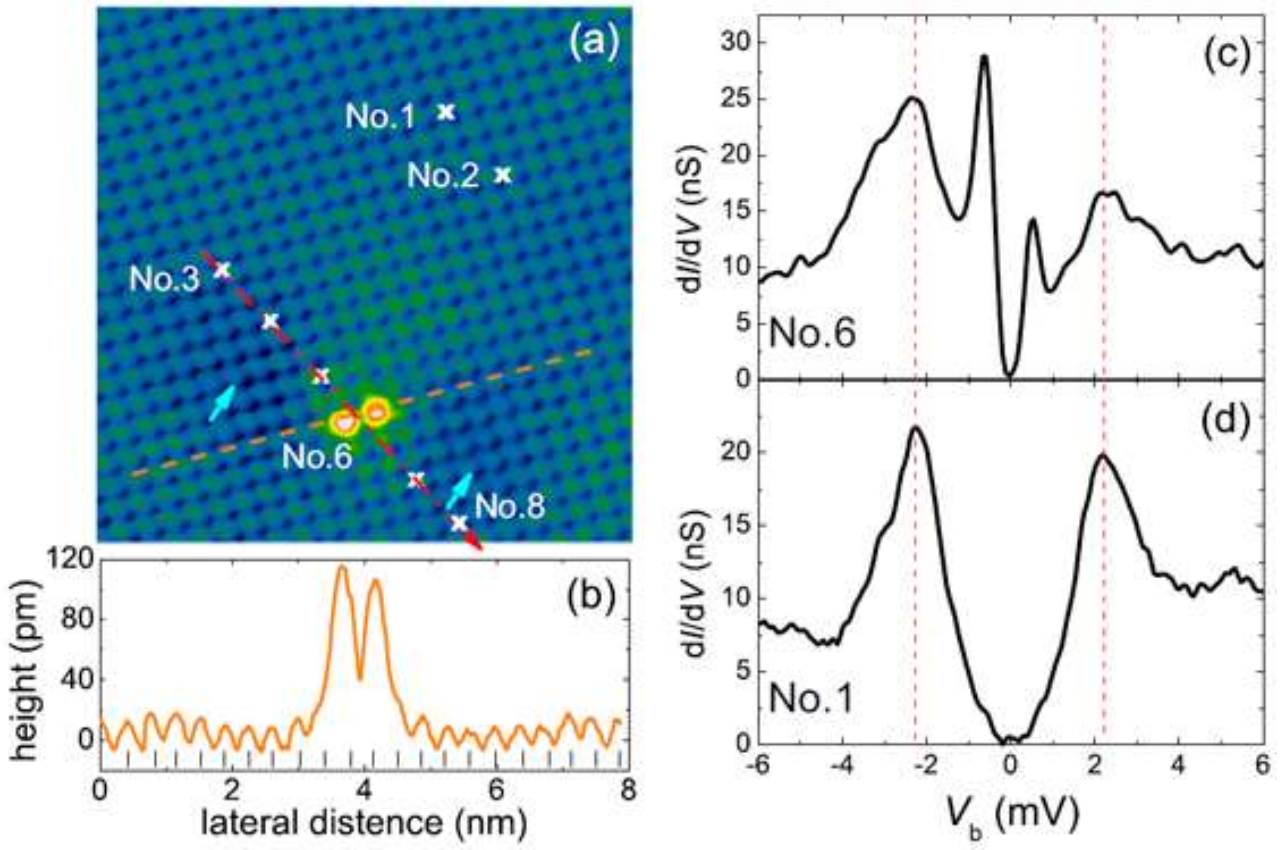

Figure 4. STM topographic and spectroscopic measurements in an FeSe single crystal performed in the superconducting phase at 350 mK. (a) Topographic image showing the Se atoms of the topmost layer in green. A dumbbell defect is imaged as brighter white Se atoms in the bottom-left part of the image. White crosses with numbers indicate the location where *dI/dV* tunnel spectra were measured. (b) Line-scan of apparent sample height measured along the red-dashed line going through the dumbbell defect in panel (a). (c) *dI/dV vs.* bias voltage V_b tunnel spectra measured close to the dumbbell defect (indicated with cross No. 6) and away from it at the location indicated with cross No. 1. The vertical lines in (c) and (d) indicate the energy location of the coherence peaks in the position away of the dumbbell defect at around 2 meV. Reprinted from 37.

III. Impact of dumbbell defects in the core electronic states of FeSe

After reviewing the more prominent results of the international community in the impact of atomic-scale de fects in the electronic structure of Fe-based superconductors, it is rather clear that understanding this issue is of key importance for assessing how critical is the occurrence of these features for the establishment of superconductivity in these compounds. With the aim of studying this impact, a recent work combining real-space topographic imaging with STM and characterization of the electronic core states with X ray photoemission spectroscopy (XPS) brings new and relevant evidence on this issue.[43] This work, performed at the Centro Atómico Bariloche of Argentina, makes a qualitative connection between the occurrence of atomic-scale dumbbell defects imaged by means of STM and the spectral shape of electronic states revealed via XPS.

The study combines these two surface sensitive techniques to study high-quality single crystals[45] of $FeSe_{1-x}S_x$ with T_c = 9.6 K for x = 0 and 10 K for the x ~ 0.03 samples studied. Several structural studies in these crystals[43,45] indicate that the samples do not show any detectable trace of spurious phases, an issue that is very relevant for a technique like XPS that is sensitive to the topmost layers of the sample but unlike STM collect information on a millimeter-size area of the sample and not locally. Transport data presented in this work for the temperature range in the vicinity of the tetragonal to-orthorhombic transition also provide evidence on the absence of any detectable spurious non-superconducting phases in the studied high-quality crystals.

Figure 5 show examples of STM topography images of the $FeSe_{1-x}S_x$ crystals studied in the tetragonal phase (normal state) of Ref. 43. The topmost Se atoms located above the top Fe plane and exposed by cleaving are shown as white

spots. These atoms are highlighted in green in the schematic crystal structure of Fig. 5 (e). Topographic images for pure and S-doped samples show a ubiquitous feature: Pairs of brighter Se atoms aligned in the a directions, see dashed-white frames in Figs. 5 (a) and (b). These brighter atoms are dumbbell defects and as in previous reports are observed as higher atomic peaks in traces of profile height, see Fig. 5 (c). Statistics in several areas of different samples show that the distribution of dumbbell defects is quite diluted, representing 4.2(0.6) and 3.8(0.6) % of the STM-imaged Se atoms in the pure and S-doped samples, respectively. Fig. 5 (f) schematically recalls the modifications on the electronic clouds of Se and Fe atoms surrounding a dumbbell defect predicted by DFT simulations:[41] the 2 Se atoms located above the Fe plane and imaged as brighter by STM (orange) show electronic clouds protruding out of the surface of the sample, and the electronic clouds of the 2 Se atoms located below the plane (magenta) and the 4 first-neighbor Fe atoms (turquoise) are assymetric. The schematics of the charge density isosurfaces in the plane, see right part of Fig. 5 (f), highlights the asymmetry in the shape of the electronic clouds of these 8 atoms with respect to the symmetric ones expected for atoms located further away from the defect (4 Fe atoms with red clouds). As previously discussed, these protrusions of the electronic cloud result in an apparent larger height (brighter spots) of the Se atoms entailed in the dumbbell defect. It is important to point out that although the density of dumbbell defects imaged by STM is small, this technique only reveals defects at the sample surface and such defects can certainly occur in every FeSe plane of the crystal. For dumbbell defects located in the bulk of the sample instead than in the surface, it may be quite likely that the protrusion and the assymetry in the charge distribution has a lesser magnitude. This is something that deserves further theoretical investigation by means of DFT simulations of defects in a bulk or at least a trilayer sample instead of in a monolayer as studied in Ref. 41. These simulations are probably not yet feasible with state-of the-art simulation clusters. Even though the magnitude of the modifications of the electronic clouds of dumbbell defects located in the bulk can not be quantified yet, the Se atoms with altered electronic environment surrounding the dumbbell defects surely have a small but maybe noticeable impact in the bulk electronic properties of the samples.

This work[43] shows that for S-doped samples, another prominent topographic feature is also imaged in several locations. This feature consists in a local depletion of the apparent sample height associated to darker chalcogen atoms. Height profiles along these features indicate that in the darker areas there is a height depletion of roughly 25 % with respect to neighbor Se atoms, see for example Fig. 5 (d). These features are not detected in measurements in pure FeSe crystals from different origin.[29,41–43] These defects were also observed in STM topographies of S-doped crystals with an occurrence that grows with the S concentration.[29] Given that S has a smaller atomic radius than Se, it can be assumed that S atoms are imaged by STM as these darker features entailing a local height depletion.[43] Irrespective of the nature of the defects introduced by S doping, these results indicate that crystal disorder is more important in S-doped samples than in pure ones.

The connection between these atomic defects and the electronic core states is performed in Ref. 43 by means of detailed fits of the peaks detected in XPS spectra. XPS measurements provide information on the energy spectrum of the core levels of the different elements composing the material. As discussed in Ref. 43, in the XPS spectra measured in the studied $FeSe_{1-x}S_x$ crystals the Fe and Se contributions are detected at energies close to the ones corresponding to the tabulated peaks for the different core levels for the pure elements.[46] The S peaks are not clearly observed in the XPS spectra since they come from a small amount of S and are maybe hindered by the superimposition with the Se 3p peaks detected at closer energies than expected for S 2p, and also present a photoemission cross section 3 times smaller than those Se peaks. In addition, Ref. 43 discusses on the importance of analyzing XPS spectra of samples cleaved in-situ under UHV conditions since else extra peaks and deformations of peaks associated to the Fe levels are observed due probably to the oxidation of the topmost layer of the sample if not cleaved in-situ. This was also pointed out in a more recent paper studying ageing effects in air-cleaved FeSe crystals.[47]

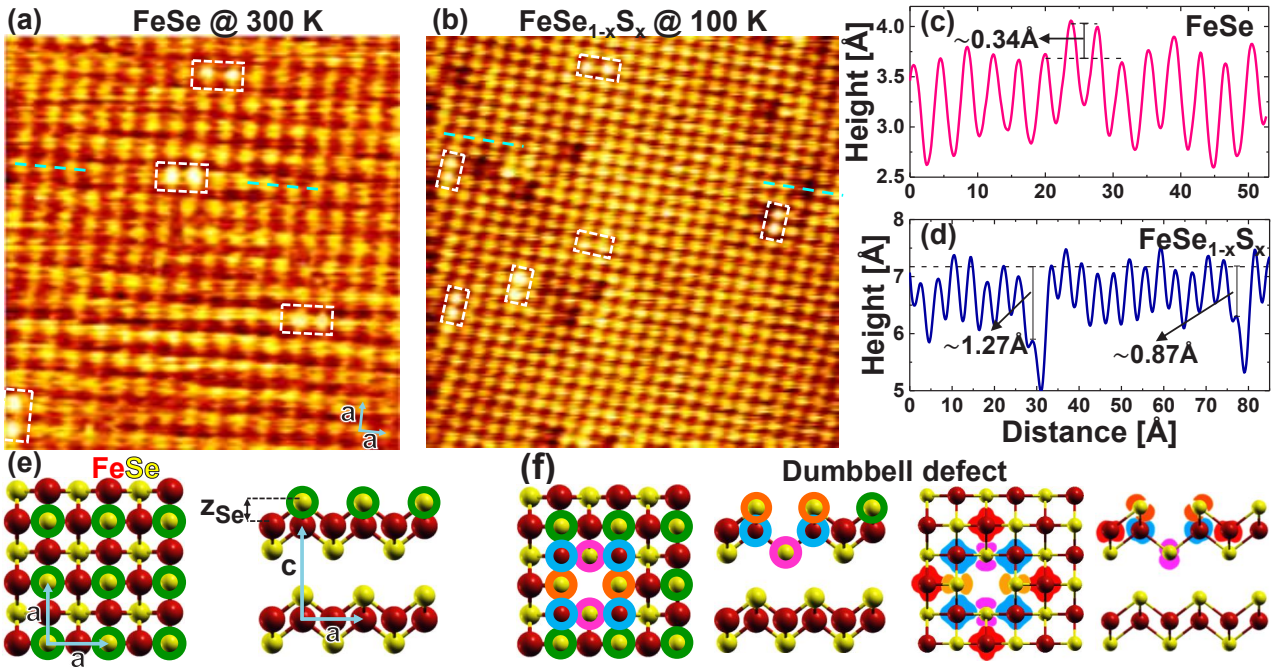

Figure 5. STM topography images and crystal structure of $FeSe_{1-x}S_x$ in the high-temperature tetragonal phase. (a) Topography of a single crystal with $x = 0$ where the exposed Se atoms are observed as bright spots. Dumbbell defects (see white dashed frames) are observed as two bright Se atoms oriented along the a-axis directions. (b) Topography of a crystal with x ~ 0.03 where local depletions of the sample height (darker chalcogen atoms) are presumably generated by smaller S dopant atoms. Dumbbell defects are also indicated with dashed-white frames. (c) Height-profile in FeSe along the trace indicated (partially) with a turquoise dashed line in panel (a) where a dumbbell defect is evident. (d) Height-profile in the S-doped crystal along the trace indicated with the turquoise line in panel (b). Local minima in the surface height are detected in the darker features. (e) Schematic representation of the FeSe crystal structure in the tetragonal phase with the measured $a = 3.77$ Å and $c = 5.52$ Å unit cell vectors indicated. When cleaving the samples to perform STM measurements, the Se atoms located above the top Fe plane are imaged (highlighted in green). (f) Schematic of a dumbbell defect associated with an Fe vacancy: Atomic positions (left) and charge density isosurfaces (right) of the atoms entailed in the defect. The atomic clouds of the neighbouring Se and Fe atoms are schematically reproduced from the DFT calculations of Ref.[41]. Reprinted from 43.

Figure 6 shows the most intense Se peaks of the XPS spectra reported in Ref. 43, the Se 3d doublet with two broad peaks centered at approximately 54 and 55 meV of binding energy for both the pure and S-doped samples. The study focus on the details of the XPS spectra in this energy range to ascertain both, if there is a surface contribution, and to describe the electronic states via fits of the data. Panel (a) of this figure presents the XPS spectra obtained for pure FeSe samples for two different detection angles for the photoemited electrons. The shape of the measured spectra is almost independent of the detection angle within the noise level, implying that the measured spectra are not affected by possible surface states and are representative of the electronic levels in the bulk of a nanometer-thick top layer as probed by XPS. Panels (b) and (c) present data (color dots) measured in pure and S-doped samples, respectively. The spectral shape in this energy range for both types of samples are alike. Both present two sharp peaks corresponding to the Se $3d_{5/2}$ and $3d_{3/2}$ core levels and a broad peak around 53 eV associated with the Fe $3p_{3/2}$ and Fe $3p_{1/2}$ core levels are observed as a shoulder in the low-energy flank of the Se 3d peaks. The authors of this work fit these spectra considering: (a) Shirley background associated to the photoemission process of secondary electrons (black dashed line), (b) a pair of Voigt-like peaks for the Fe 3p doublet (full red lines), (c) two pairs of Voigt-like peaks for the Se 3d doublet (full green and magenta lines). The authors stress that it is compulsory to consider two pairs of Se 3d spin-orbit doublets, instead of one, in order to properly fit the data. In this fitting procedure, the corresponding spin-orbit splitting and statistical intensity ratios theoretically expected for both peaks of the doublet were left fixed, while the energy location of the pairs of peaks are allowed to vary. The main component corresponding to the green spin-orbit doublet is centered at exactly the same energies where the peaks are detected in the experimental spectra. This component represents 86 % (85 %) of the area under the curve of the Se 3d peaks fit in pure (S-doped) samples. The second contribution (magenta lines) is shifted 0.64 eV towards larger binding energies with respect to the experimentally detected peaks. The consideration of these minor contribution with an area under the curve of 14 % (15 %) is compulsory in order to properly fit the data in both, pure and S-doped FeSe samples.

The need of considering a second contribution to the Se 3d levels in order to properly fit the XPS data in both pure and S-doped samples indicates that a signifi cant amount of Se atoms, roughly 14 %, has a different electronic environment than the rest of Se atoms. Since curves obtained in measurements performed at different detection angles are rather coincident, the authors rule out the origin of this second component on a surface associated state.[43] Based on a detailed analysis of X-ray, XPS and resistitivy data that show no detectable traces of spurious phases[48] the authors rule out the possibility of this second component coming from intergrowths in the samples. The second component is thus only associated with local variations of charge transfer that occur in the nanometer-thick bulk of the samples probed by XPS.

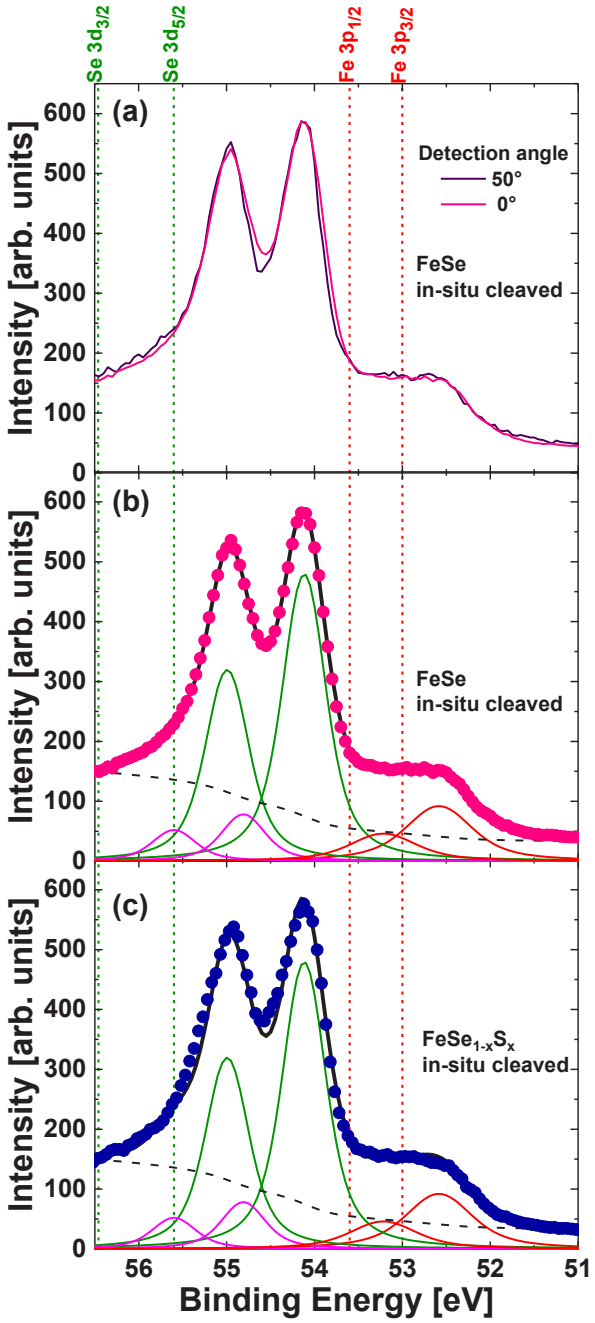

Figure 6. (a) XPS spectra in the energy region of the Se 3d and Fe3p peaks for a pure FeSe sample. Measurements performed at two different detection angles of photoemited electrons. (b) Pink points: same data than in panel (a) for a detection angle of 0 ˚(normal incidence). Full black line: Fit of the experimental data with a convolution of doublets of Voigt-like peaks after subtraction of a Shirley background (see black dashed line). The broad peak observed around 53 eV associated to the Fe 3p core levels is fitted with a spin-orbit doublet (see red lines). Two pairs of peaks shown with green and magenta lines come from a principal and a minor doublet contribution associated with the Se 3d core levels. (c) Same analysis than in panel (b) for the XPS spectra measured in the S-doped crystal at normal incidence. In all panels dashed vertical lines correspond to the tabulated values for the core level energies in the pure elements. Reprinted from 43.

Recalling that the atomic resolution images of $FeSe_{1-x}S_x$ shown in Fig. 5 as well as previous works in films and crystals of FeSe [29,41,42] present Fe vacancy induced dumbbell defects, the authors of Ref. 43 propose the second component in XPS spectra comes from the Se atoms with electronic clouds modified by the Fe vacancy at the dumbbell. Indeed, according to the DFT calculations of Huang *et al.*[41], every dumbbell defect entails changes in the electronic environment of the 4 Se atoms surrounding the Fe vacancy. The experimentally detected density of Se atoms participating in dumbbell defects of roughly 3 %, and the area under the curve of the second Se 3d component in the XPS spectra, are roughly the same for pure and S-doped FeSe samples. This finding points on the second XPS component having the same electronic origin in both types of samples. In addition, the energy location of the doublet of the second component is at larger binding energies than the main component, a fact that is in agreement with the second component coming from a minority of Se atoms having an electronic environment with less charge produced by the lacking Fe atom at the dumbbell. Therefore, by combining local topographic imaging techniques and nanometer-thick bulk electronic measurements, this work[43] probes that in the Fe-based superconductor $FeSe_{1-x}S_x$ dumbbell-type atomic defects have an important effect on the electronic properties of the compounds.

IV. Summary and perspective

In conclusion, the experimental and theoretical works discussed in the previous two sections show that STM revealed local atomic-scale defects in the crystal structure of the simplest Fe-based superconductor have a noticeable impact in the electronic properties of the material. This effect is evidenced in the superconducting phase of the material[19,37] as well as in the normal state phase,[40,41,43] irrespective of the samples being crystals or few-layer thick films. A recent work goes further on this qualitative assertion and quantifies the impact of atomic scale defects in the core electronic states measured by XPS.[43] The authors show that a minor second component in the Se 3d doublet is compulsory to properly fit the spectral shape of XPS data. Since the area under the curve of this component is small and its energy location goes towards larger binding energies, implying a loss of charge in the Se induced by the Fe vacancy associated to the dumbbell defects, the authors propose that the second component is associated with the modification of the electronic cloud of the minority of Se atoms surrounding these defects.

Yet, several questions remain open as to completely settle the issue on the details of this interplay. For instance, the question on whether the height of the apical Se atoms neighbouring the dumbbell defect is affected by the Fe vacancy is very relevant. As mentioned in the introduction, most of the compounds of the broad Fe based superconductors family presents an optimal value of its critical temperature for a given value of this apical height.[28] This issue is particularly relevant since in the case of few-layer-thick FeSe films when dumbbell defects proliferate above a relatively small amount,[40] superconductivity is spoiled. Thus, more insight in the impact of atomic scale defects in the superconducting proper ties will be gained by performing DFT simulations that search for possible changes in the apical height of the Se atoms surrounding the dumbbell defects. Also, a careful study on this issue on increasing the defects density will allow to have an idea on the details on how super conductivity might be degraded in the FeSe compound. These simulations consume an extremely large computational time and are not affordable by regular simulation clusters, but certainly new studies would point in that direction in the future.

In addition, another issue that deserves further investigation to have a better quantitative understanding of the impact of dumbbel defects in FeSe is to correlate the area under the curve of the second component of the Se 3d levels and the amount of Se atoms that have a modified electronic cloud in the vicinity of the defects. Regarding this point, I would like to stress that it is possible that the Fe vacancy of a dumbbell affects the orbitals of more than the 4 Se surrounding atoms as proposed by Huang *et al.* Further DFT calculations appropriately considering the van der Waals intra and inter-layers interaction, and the stripe-antiferromagnetic magnetic state of the Fe atoms in this compound[49] are important to quantitatively asses the possibility of the electronic cloud of more than 4 Se atoms being affected by the Fe vacancy producing the dumbbell defect. The consideration of these two important issues in DFT simulations would also give more realistic information on the possible modification of the Se apical height around the dumbbell defects dis cussed above. In addition, further all-electron calculations are required in order to connect the information obtained with experimental STM imaging and first principle simulations as the DFT ones discussed here, with the shifting of a second component towards larger binding energies.

Ultimately, all the results presented in this review as well as the open questions highlight the impact of atomic defects in the binding energy and spectral shape of the core levels in $FeSe_{1-x}S_x$. The experimental and theoretical results discussed here in this family of compounds are just a notable example of the subtle interplay between the crystal structure and the electronic states in Fe-based superconductors in general.

Acknowledgments

I thank J. Aragón Sánchez, G. L. Nieva, M. L. Amigó, E. Gayone E. Martínez and C. Ventura for insightful discussions. Work supported by the Argentinean ANPCyT through grants PICT 2017-2182 and 2018-1533, by Con icet through grant PIP 2021-1848 and by the Universidad Nacional de Cuyo research grants 06/C566 and 06/C575. The author also acknowledges funding from the Alexan der von Humboldt Foundation of Germany through the Georg Forster Research Award.

References

[1] Bednorz, J G and M ”uller, K A, Z. fur Physik B - Condensed Matter 64, 189 (1986).

[2] Chu, P. C. W, Proc. Nat. Acad. Sciences 84, 4681 (1987).

[3] Takagi H, Uchida S, Kitazawa K and Tanaka S, Jpn. J. Appl. Phys. 26, 123 (1987).

[4] Ginzburg V L, Soviet Physics Uspekhi 34, 283 (1991).

[5] Chu P C W, Scientific American, 162 (1995).

[6] Kamihara Y, Watanabe T, Hirano M. and Hosono, H, J. Am. Chem. Soc. 130, 3296 (2008).

[7] Hsu F C, *et al.*, Proc. Nat. Acad. Sciences 105, 38 (2008).

[8] Rotter M, Tegel M and Johrendt M, Phys. Rev. Lett. 101, 107006 (2008).

[9] Tapp J H, Tang Z, Lv B, Sasmal K, Lorenz B, Chu P C W, Guloy A M, Phys. Rev. B 78, 060505 (2008).

[10] Pitcher M J, Parker D R, Adamson P, Herkelrath S J C, Boothroyd A T, Ibberson R M, Brunelli M and Clarke S J, Chem. Commun. 45, 5918 (2008).

[11] Wang X C, Liu Q Q, Lv Y X, Gao W B, Yang L X, Yu R C, Li F Y and Jin C Q, Solid State Commun.148, 538 (2008).

[12] Norman M R, Physics 1, 21 (2008).

[13] Búchner B and Hess C, Nature Materials 8, 615 (2009).

[14] Bohmer A E and Kreisel A, J. Phys. Condens. Matter 30, 023001 (2018).

[15] Chen T, Yi M and Dai P, Frontiers Phys. 8, 00314 (2020).

[16] Margadonna S, Takabayashi Y, McDonald M T, Kasperkiewicz K, Mizuguchi Y, Takano Y, Fitch A N, Suarde E and Prassides K, Chem. Comm. 43, 5607 (2008).

[17] McQueen T M, Huang Q, Ksenofontov V, Felser C, Xu Q, Zandbergen H, Hor Y S, Allred J, Williams A J, Qu D, Checkelsky J, Ong N P and Cava R J, Phys. Rev. B 79, 014522 (2009).

[18] Bendele M, Amato A, Conder K, Elender M, Keller H, Klauss H-H, Luetkens H, Pomjakushina M, Raselli A and Khasanov R, Phys. Rev. Lett. 104, 087003 (2010).

[19] Song C-L *et al.*, Science 332, 1410 (2011).

[20] Watson M D, Kim T K, Haghighirad A A, Blake S F, Davies N R, Hoesch M, Wolf T and Coldea A I, Phys. Rev. B 92, 121108 (2015).

[21] Imai T, Ahilan K, Ning F L, McQueen T M and Cava R J, Phys. Rev. Lett. 102, 177005 (2009).

[22] Fasano Y, Maggio-Aprile I, Zhigadlo N D, Katrych S, Karpinski J and Fischer Ø, Phys. Rev. Lett. 105, 167005 (2010).

[23] Hoffman J E, Rep. Prog. Phys. 74, 124513 (2011).

[24] Chi S, Grothe S, Liang R, Dosanjh P, Hardy W N, Burke S A, Bonn D A, and Pennec A, Phys. Rev. Lett. 109, 087002 (2012).

[25] Margadonna S, Takabayashi Y, Ohishi Y, Mizuguchi Y, Takano Y, Kagayama T, Nakagawa T, Takata M and Pras sides M, Phys. Rev. B 80, 064506 (2009).

[26] Medvedev S, McQueen T M, Troyan I A, Palasyuk T, Eremets M I, Cava R J, Naghavi S, Casper F, Ksenofontov V, Wortmann G and Felser C, Nature Materials 8, 630 (2009).

[27] Krzton-Maziopa A, Svitlyk V, Pomjakushina E, Puzniak R and Conder K, J. Phys.: Condens. Matter 28, 293002 (2016).

[28] Mizuguchi Y, Hara Y, Deguchi K, Tsuda S, Yamaguchi T, Takeda K, Kotegawa H, Tou H, and Takano Y, Supercond. Sci. Technol. 23, 054013 (2010).

[29] Hanaguri T, Iwaya K, Kohsaka Y, Machida T, Watashige T, Kasahara K, Shibauchi T and Matsuda Y, Sci. Adv. 4, eaar6419 (2018).

[30] Ge J-F, Liu Z-H, Liu C, Gao C-L, Qian D, Xue Q-K, Liu Y and Jia J-F, Nat. Mat. 14 285 (2014).

[31] Miyata Y, Nakayama K, Sugawara K, Sato T and Taka hashi T, Nat. Mat. 14 775 (2015).

[32] Kitchen D, Richardella A, Tang J-M, Flatt´e M E, Yazdani A, Nature 442, 436 (2006).

[33] Weber B *et al.*, Science 335, 64 (2012).

[34] Yeh K-W *et al.*, Eur. Phys. Lett. 84, 37002 (2008).

[35] Yin Y, Zech M, Williams T L, Wang X F, Wu G, Chen X H, Hoffman J. E., Phys. Rev. Lett. 102, 097002 (2009).

[36] Demirdiş S, van der Beek C J, Fasano Y, Cejas Bolecek N R, Pastoriza H, Colson D, Rullier-Albenque F, Phys. Rev. B 84, 094517 (2011).

[37] Jiao L, Rö*β*ler S, Koz C, Schwarz U, Kasinathan D, Rö*β*ler U K, Wirth S, Phys. Rev. B 96, 094504 (2017).

[38] Fischer Ø, Kugler M, Maggio-Aprile I, Berthod C, Renner Ch, Rev. Mod. Phys. 79, 353 (2007).

[39] Jenkins N, Fasano Y, Berthod C, Maggio-Aprile I, Piriou A, Giannini E, Hoogenboom B W, Hess C, Cren T, Fischer Ø, Phys. Rev. Lett. 103, 227001 (2009).

[40] Song C-L, Wang Y-L, Jiang Y-P, Li Z, Wang L, He K, Chen X, Ma X-C and Xue Q-K, Phys. Rev. B 84, 020503 (2011).

[41] Huang D, Webb T A, Song C-L, Chang C-Z, Moodera J S, Kaxiras E and Hoffman J E, Nano Lett. 16, 4224 (2016).

[42] Putilov A V, Di Giorgio C, Vadimov V L, Trainer D J, Lechner E M, Curtis J L, Abdel-Hafiez M, Volkova O S, Vasiliev A N, Chareev D A, Karapetrov G, Koshelev A E, Aladyshkin A Y, Mel'nikov A S, Iavarone M, Phys. Rev. B 99, 144514 (2019).

[43] Aragón Sánchez J, Amigó M L, Belussi C H, Ale Crivillero M V, Suárez S, Guimpel J, Nieva G, Gayone J E, Fasano Y, J. Phys. Mater. 5, 044008 (2022).

[44] Berthod C, Fasano Y, Maggio-Aprile I, Piriou A, Giannini E, Levy de Castro G, Fischer Ø, Phys. Rev. B 88, 014528 (2013).

[45] Amigó M L, Ale Crivillero V, Franco D G, and Nieva G, Journal of Phys.: Conf. Series 568, 022005 (2014).

[46] Moulder J F, Stickle W F, Sobol P E and Bomben K D, *Handbook of X-Ray Photoelectron Spectroscopy*, Min nesota: Perkin-Elmer Corporation (1992).

[47] Lanoël L, Rozas G, Bruchhausen A E, Amig´o M L, Ale Crivillero M V, Hofer J A, Villafuerte M, Bridoux G, Bengió S, Nieva G, Phys. Rev. B 106, 214507 (2022).

[48] Yamasaki A *et al.*, Phys. Rev. B 82, 184511 (2010).

[49] Lochner F, Eremin I M, Hickel T and Neugebauer J, Phys. Rev. B 103, 054506 (2021).

Bio

Yanina Fasano

Yanina Fasano performs research in the field of experimental condensed matter at low temperatures, focusing on superconductivity and vortex matter studied by means of spectroscopic techniques with atomic resolution. She received her PhD in Physics from the Instituto Balseiro at Bariloche, Argentina, in 2003. After a postdoctoral appointment at the University of Geneva, Switzerland, she joined the Low Temperatures Lab at the Centro Atómico Bariloche of the Atomic National Commission as a tenured researcher of Conicet. In 2021 she became assistant professor at the Instituto Balseiro. She received the Houssay prize of the Ministry of Science, Technology and Innovation of Argentina in 2022 and was honored with the Georg Forster Research Prize from the Alexander von Humboldt Foundation in 2021.

Science Reviews
from the end of the world

Vol. 2, No. 3, October 2023 // pp. 21-38 /

Membrane-peptide interaction: Focusing on membrane properties

Natalia Wilke[a,b*], Dayane S. Alvares[c], Matías A. Crosio[a,b], Matías A. Via[d], Mariela R. Monti[a,b], L. Stefanía Vargas Velez[a,b], Sofía V, Amante[e], Pablo E. Scurti[e], Valeria Rulloni[e]

[a] *Universidad Nacional de Córdoba, Facultad de Ciencias Químicas, Departamento de Química Biológica Ranwel Caputto, Córdoba, Argentina*
[b] *CONICET, Universidad Nacional de Córdoba, Centro de Investigaciones en Química Biológica de Córdoba (CIQUIBIC), Córdoba, Argentina*
[c] *UNESP/IBILCE, São Paulo State University, Department of Physics, São José do Rio Preto, Brazil*
[d] *Arla Foods a.m.b.a. Aarhus, Denmark.*
[e] *Universidad Nacional de Córdoba, Facultad de Ciencias Exactas, Físicas y Naturales, Córdoba, Argentina*

** Corresponding author. E-mail: natalia.wilke@unc.edu.ar*

Abstract

Cellular membranes compartmentalize cells, comprise a permeability barrier, and are the starting place for several signaling cascades and processes in which lateral diffusion of molecules is a key factor. Although it has been shown that organisms adapt the lipid composition of their membranes in order to maintain these in a mainly fluid state, several studies point to the coexistence of regions with different compositions and mechanical properties. In this context, while proteins have been related to solid docks, sterols are accepted as liquid-ordered phase state inducers. Thus, the current model for membranes is a patchwork-like surface, with the different regions being highly variable in size and very dynamic.

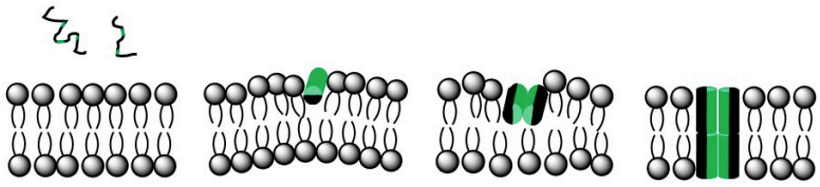

Many peptides, like cationic antimicrobial peptides and cell penetrating peptides, target cell membranes. The affinity of these soluble peptides to membranes depends on membrane features such as composition, charge density, compaction, and fluidity. As a consequence of the patchwork-like character of the membrane, regions with a broad spectrum of properties are available to interact with these peptides. Therefore, it is important to know how peptide-membrane interaction depends on membrane properties, and also what happens with the membranes after the interaction.

Here, we summarize our contribution to understanding how the interaction of peptides with membranes is modulated by membrane properties. The influence of the phase state, electrostatics, and chemical composition of the membrane on peptide binding is described using biomimetic systems. The effect of peptide association on membrane properties is also revisited. Finally, possible extrapolations to cells are discussed.

Keywords: Membrane adaptation, membrane physicochemical properties, Antimicrobial alternative drugs, Membrane-active peptides, pore formation

Introduction

Cell membranes are composed of lipids and proteins, and the accepted model proposes that they are formed by a lipid matrix in which proteins insert. This model dates from 1972 [1] and is known as the Fluid-Mosaic Membrane (FMM) model[1]. It was envisioned as a basic framework model for cell membranes that could explain existing data on the behavior of membrane proteins and lipid structures, and their dynamics. Within a few years of its introduction, it became obvious that the FMM model needed to be modified to reflect the emerging data on extracellular and intracellular mechanisms. Therefore, with the FMM model as a basis, novel cell membrane models emerged, proposing a much less homogeneous view.

The current model considers the interaction of the extracellular matrix and membrane-associated cytoskeletal components with cell membranes, and their potential influence on the mobility and distribution of trans-membrane glycoproteins, as well as the possibility that less mobile lipid-protein or lipid-lipid domains might exist in membranes, like frozen or semi-frozen islands of less mobile lipids in a sea of fluid phospholipids [2]. This model has been tested in recent decades with single particle tracking experiments and super-resolution microscopy, among other techniques, and it has been concluded that, although fluidity is detected at the mesoscale, membranes are very heterogeneous and dynamic, and several obstacles hinder the free motion of the membrane components [3].

The plasma membrane forms a dynamic multi-dimensional architecture that can quickly respond to intracellular (and extracellular) events. Kusumi et al. have proposed that plasma membranes are organized for this purpose into dynamic hierarchical structures [3]. Within these hierarchical structures, membrane components (macroscopically) diffuse from 5 to 50 times slower than when the same components are reconstituted into artificial membranes without membrane-associated cytoskeletal or other structures. Conversely, the macroscopic diffusion rates can also be increased (20-fold) through disruption of membrane-associated cytoskeletal networks.

Thus, cell membrane properties are variable in time and space, making them very plastic in the sense that they can change local properties in order to rapidly adapt to a specific requirement. The presence of transient heterogeneities also implies that the environment interacts with membranes with a great variety of compositions, and consequently, different characteristics.

Of particular interest are the mechanical properties. Membranes cannot be too easily deformable, nor too rigid. They may have to change from rigid to soft depending on the environment or cell metabolism. Three different kinds of deformations of mechanical properties must be distinguished. Membranes can be considered as a quasi-two-dimensional system that can be compressed or expanded (changes in the area), can be deformed (shear stress), or curved (bending stress) [4]. Each kind of stress may have an immediate and a delayed response, since membranes are usually viscoelastic.

In our research group, we have studied membrane rigidity/softness under the presence of membrane active peptides (MAPs). MAPs are able to translocate membranes or permeabilize them by pore/defect formation, and even cause membrane rupture through different mechanisms [5]. Briefly, in the carpet model, peptides disrupt the lipid bilayer, forming lipid-peptide soluble aggregates. Peptides can also insert into the membrane and aggregate to form toroidal or barrel pores. Membrane permeation may also be increased by an electroporation-like mechanism, driven by the adsorption of highly charged peptides on the lipid-solution interface, or by locally thinning the membrane. Finally, peptides can translocate through the formation of a lipid-peptide complex inside the membrane, which is known as the adaptative mechanism.

Two kinds of MAPs can be distinguished: Cell-Penetrating Peptides (CPPs) and Anti-Microbial Peptides (AMPs). The difference between these is mainly functional [6], since AMPs induce membrane rupture at low proportions, while CPPs are able to translocate the membrane without damaging it [7,8]. Due to their ability to translocate cell membranes, CPPs are used as a tool for incorporating molecules inside cells as cargoes bound to the peptide (CPP-molecule chimeras).

AMPs are proposed as substitutes for traditional antibiotics as bacteria do not acquire resistance to these as easily as to traditional antibiotics. The reason for this is that the target of peptide action is the lipid region of the membranes, and thus bacteria have to change lipid composition in order to become resistant [9]. However, changes in lipid composition lead to changes in membrane properties, and these properties have to remain within an optimal range for cells to survive [10].

MAPs may have a high positive charge or be slightly charged, and they may be amphipathic, or completely hydrophilic. Conversely, many peptides that act at lipid-water interfaces assume an amphipathic secondary structure, induced by the anisotropy of the interface. In recent years, there has been increasing interest in this kind of peptide, and much effort has been put into analyzing the peptide properties that optimize membrane-peptide interaction and the subsequent translocation/pore formation/lysis. However, less work has been done in understanding the membrane factors that modulate the processes. Even fewer studies have examined the effect of the peptide on the membrane properties at sublytic doses.

The studies performed so far indicate that the specific mechanism, as well as the fate of the membrane after peptide-membrane interactions, is commanded by both peptide and membrane characteristics. Since membranes are heterogeneous and in constant change, a clear picture of which membrane properties are key, as well as which properties may change, is crucial. Therefore, we aim to understand which of the membrane properties are able to direct peptides towards the target membrane, and which are the main properties of the membrane that become affected by the peptide-membrane interaction. The results found up to now are summarized here.

This review has been structured into five sections. The first gives a brief description of the biomimetic systems that can be used for membrane-peptide interaction studies. The second to fourth sections focus on the findings about the influence of electrostatics, phase state, and lipid composition of the membrane. The final section includes possible extrapolations to cell membranes. Results with two peptides are presented: the poly-arginine KR9C (net charge +10, see Figure 1) as a CPP example [11,12], and Polybia-MP1 (or simply, MP1) peptide (IDWKKLLDAAKQIL-NH_2, net charge +2, see Figure 1) as an AMP example [13]Polybia-CP: I L G T I L G L L K S L-NH2 (1239.73 Da.

The poly-arginine peptide is hydrophilic and does not acquire secondary structure or amphipathicity upon binding to membranes [11,12,14]. MP1 is also unfolded in solution, but acquires an alpha helix structure in contact with lipid bilayers, with the corresponding secondary amphipathicity [15,16].

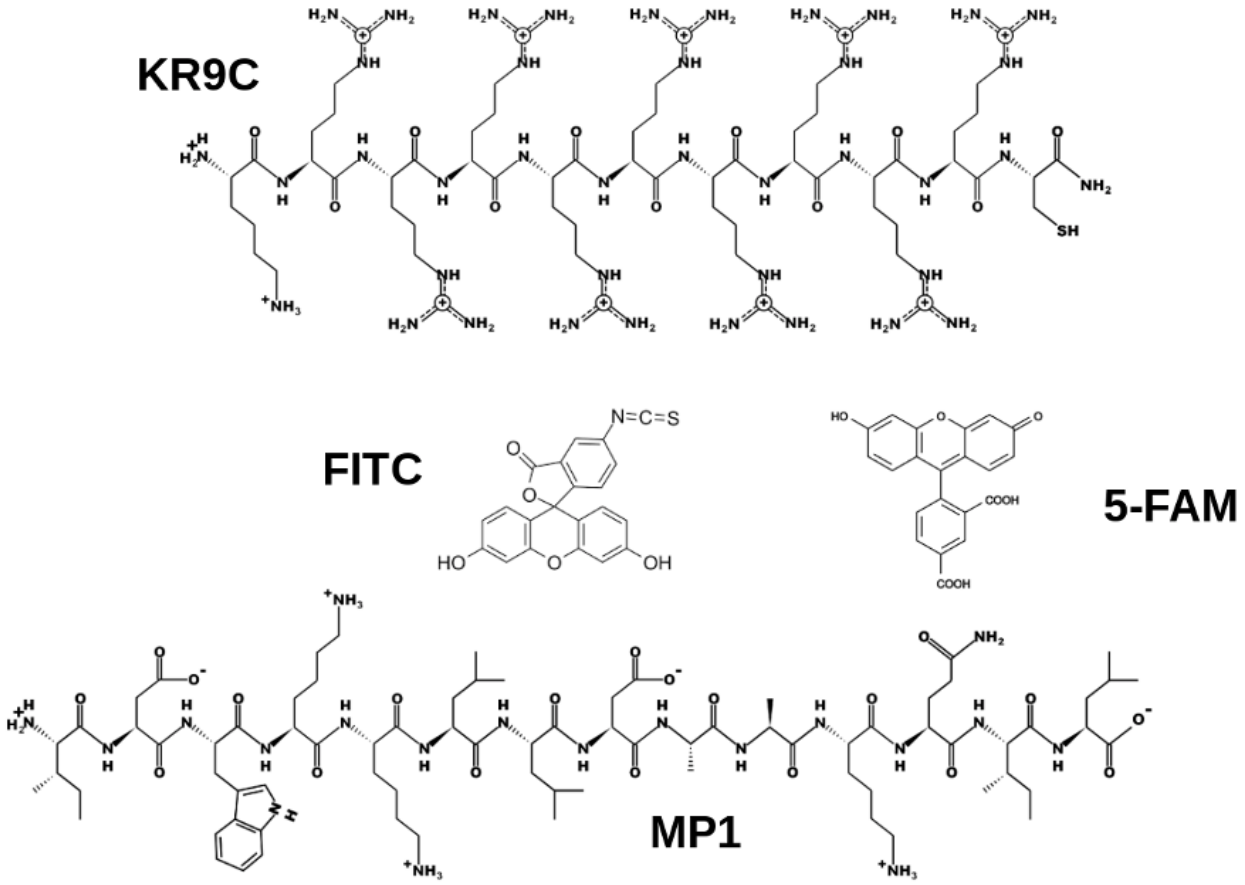

Figure 1 Chemical structures of the peptides used (KR9C and MP1) and the fluorescent moieties (FITC and 5-FAM).

1- Biomimetic systems and techniques used for studying peptide-lipid interactions

Biological membranes are complex open systems and, due to their dynamic composition, understanding the principles that rule their lateral organization and the relation with their functioning is a challenging task. However, with the revolutionary work of Mueller et al. creating ‘‘black lipid membranes’’ [17] and the discovery of liposomes by Bangham et al. [18], the

study of lipid bilayer properties has grown at an exponential rate, and many other areas have been developed from the application of these model membrane systems [19].

Several lipid systems have been successfully used as model membranes for studies on peptide-lipid interactions. All of them are oversimplifications of the real cell membrane, since the only perturbation performed on the system is the presence of the peptide. In a cell membrane, different processes occur simultaneously with the one studied, making interpretation difficult. Therefore, performing experiments in simplified artificial membranes is a very useful tool for understanding membrane-peptide interaction, despite the extrapolation of the results to systems *in-vivo* not being straightforward.

Each model system has certain advantages and disadvantages, depending on the situation in which it is more suitable to be used. Related to this, cell membranes in biological systems cannot necessarily be considered similar to free-standing bilayers, since they are often interacting with (and supported by) cytoskeletal proteins, neighboring membrane stacks, and extracellular matrices, with these interactions affecting the native lipid phase behavior. Therefore, in order to fully exploit the existing membrane model systems to retrieve biologically relevant information, it is important to have as clear as possible an understanding of the influence of preparation conditions on the lipid film.

It was demonstrated that results obtained with different models may be compared qualitatively, but not always quantitatively [20,21]. Even when working with a simple phospholipid mixture, the properties of the phases change between the different model membranes. Therefore, it is always desirable to use as many model systems as possible, with the choice of a given biomimetic system depending on which property is under study.

Having said that, we will now briefly describe the techniques and systems used for the results and summarize them here, along with the information that can be obtained from the results in relation to peptide-membrane interactions.

Aqueous peptides first interact with the external hemilayer of the membrane, adsorb, and eventually incorporate into the hydrophobic region. Afterward, membrane disruption by the peptide or peptide translocation without membrane rupture may occur.

The first step in peptide-membrane interaction can be followed using Langmuir monolayers, that is, a monomolecular film at the air-water interface. Langmuir films can be compressed, and thereby the molecular density can be varied, while the surface tension (γ) and electrostatic potential (ΔV) are registered. Additionally, the membrane can be simultaneously observed by Brewster angle microscopy or fluorescence microscopy [22,23]. The electrostatic potential determined in Langmuir monolayers is calculated as the change in the Volta potential difference of the air relative to the aqueous solution after generating the monomolecular film. For this determination, two electrodes are used: a reference electrode inside the aqueous solution, and a second electrode in the air. Two methods exist for determining electrostatic potential, depending on the characteristics of this second electrode: a radioactive electrode is used in the ionizing method, and a vibrating electrode in the kelvin method [24,25].

Since the only change in the system before and after generating the monolayer is the presence of the film at the air-water interface, changes in Volta potential differences are assigned to changes at the interface. Therefore, the DV has contributions from the water molecules and ions that orient around the lipid polar head-group, and from the molecular dipoles that orient perpendicular to the interface.

The interaction of the monolayer with soluble peptides is usually studied by adding the molecule to the solution underneath the film, which is previously prepared at the desired molecular density. The film compaction is defined by the surface pressure $\pi=\gamma_0-\gamma$, where γ_0 is the surface tension of the clean interface and g is the surface tension in the presence of the amphiphile.

Surface tension decreases (and thus, π increases) when the peptide penetrates the monolayer, with the change in π ($\Delta\pi$) being a measure of the strength of the perturbation promoted by the peptide on the film. It is important to remark here that $\Delta\pi$ depends on both the degree of peptide penetration and the compressibility of the host film. In a stiff monolayer, a small change in the area caused by peptide insertion will promote high changes in π, while in a more compressible film, lower π changes may be recorded as a consequence of the same area change. Therefore, to obtain a film parameter independent of the host film stiffness, changes in film area (ΔA) can be calculated from $\Delta\pi$. This is performed assuming that the film can be tessellated into two types of region: those where the peptide penetrates and disrupts the monolayer structure, forming a lipid-peptide structure, and those that are formed by pure lipids. Thus, the pure lipid regions get progressively compressed as the peptide penetrates and a peptide-lipid structure is formed. ΔA corresponds to the compaction of the lipid molecules inside the pure lipid regions, which is a better parameter than $\Delta\pi$ for comparing different monolayers [26].

Another important parameter that can be obtained from experiments of peptide adsorption into lipid monolayers is the exclusion surface pressure (π_e), which is the maximal surface pressure at which peptides penetrate the film. This

parameter can be obtained from extrapolations to $\Delta\pi$=0 mN/m of $\Delta\pi$ plots as a function of the initial surface pressure of the film (corresponding to the molecular density of the lipids before the addition of the peptide). High π_e indicates that the peptide is included in the film even at high compaction. In order to compare the results found with monolayers with those in bilayers, it has to be considered that the molecular density of the lipids in bilayers is similar to that in monolayers at high surface pressures (30 mN/m or higher) [27,28].

Some peptides adsorb to the membrane in the polar head-groups region without deeply penetrating the monolayer, resulting in no detectable changes in surface pressure. This behavior can be detected following the reflectivity of the interface at the Brewster angle, which depends on the interface thickness [26], or through ΔV measurements for charged peptides [26].

Aside from peptide adsorption and penetration from the solution into monolayers, premixed lipid-peptide films can be prepared and studied. These experiments allow the effect of a controlled amount of peptide on film properties to be studied and the maximal surface pressure at which peptide stays at the interface to be determined. However, these experiments have the drawback that only one hemilayer is present in the system. Therefore, the peptide structure in these experiments may differ from that in a bilayer. Langmuir films cannot be used for peptide translocation, or for measuring changes in membrane parameters such as permeability or bending rigidity.

Peptide-membrane interactions can also be studied using vesicles of different sizes. Large unilamellar vesicles (LUVs) enable the determination of zeta potential, which is the potential at the slipping plane. This potential is sensitive to the net charge at the membrane-solution interface under conditions of low ionic strength. Therefore, the adsorption of charged peptides to LUV surfaces can be followed by changes in the zeta potential under these conditions [29].

Giant unilamellar vesicles (GUVs) have the advantage of being large enough to be observed with optical microscopy. Using peptides labeled with a fluorescent moiety (FITC, 5-FAM, etc.), peptide adsorption can be followed in GUVs using confocal microscopy [29,30]. With GUVs combined with labeled peptides, the internalization of the peptide into the vesicle lumen can also be followed [30]. For these experiments, the GUVs must be large enough for the signal from the membrane to be split from that from the lumen. The drawback of this method is that it requires a labeled molecule, and the size of the fluorophore is not negligible in comparison with the peptide size for small peptides like those described in this review (Figure 1). To minimize this effect, a low amount of the labeled peptide is used, combined with unlabeled peptide. Experiments can be performed with different labeled/unlabeled ratios to check the influence of the fluorophore.

Deformations of the GUV's shape can be used for studies of membrane deformability, as will be explained in Section 5. Permeability can be conveniently studied using GUVs filled with sucrose and immersed in glucose. In these experiments, the loss of contrast is followed using transmission microscopy. The contrast is due to the sucrose/glucose gradient that leads to a different refractive index in the GUV's lumen compared to the exterior. This gradient is lost when the membrane becomes permeable [31].

Alternatively, permeability can be determined in LUVs pre-loaded with carboxyfluorescein [30,32,33], which is a fluorescent molecule that self-quenches at high concentrations. In these experiments, the detection of emitted fluorescence indicates a dilution of carboxyfluorescein due to its escape from the vesicle's lumen. Since the loss of content of the vesicle also occurs when the vesicle breaks, controls of vesicle size using dynamic light scattering are mandatory. The results obtained with a fluorometer following the loss of carboxyfluorescein in LUVs come from a vesicle population, while loss of contrast in sucrose-filled GUVs corresponds to single-vesicle data, thus requiring the observation of several vesicles.

Translocation of charged peptides can be detected as ion currents induced by the application of an electric field using black lipid membranes (BLMs). In this system, the conductivity of the membrane is determined as the slope of current vs potential difference plots. Current is originated from the migration of charged species through the BLM formed in a micro-metric hole that separates two chambers in an electrochemical cell [29].

In summary, several membrane models coupled with different techniques can be used for determining the different parameters of interest. We now describe the influence of different membrane properties on membrane-peptide interaction, using results from all the above systems.

2- The influence of membrane electrostatics in peptide-membrane interactions

Membranes can be characterized by three different electrostatic potentials: transmembrane potential (Ψm), surface potential (Ψs), and dipole potential (Ψd). These potentials have been previously described and their effect has been discussed in detail [25,34,35].

We give a brief description here, using the scheme in Figure 2A. Ψm is the difference in Volta potential between the aqueous solutions at both sides of the membrane. It depends on the ionic composition of the solutions and is one of the driving forces for ionic conductance through the membrane.

Ψs is caused by the presence of charges in lipids and proteins at the membrane surface and is screened by the ions in the solutions. Ions are attracted by the electric field generated by the charged membrane, but are also subjected to thermal motion, giving rise to a diffuse layer of ions that generate a drop in potential (Ψdl, the diffuse layer potential). Gouy-Chapman or Stern models are used to describe this potential drop, and the Debye length (λ_D) emerges as an important parameter, being the distance at which the electric potential decreases in magnitude by 1/e.

Finally, a nonlinear change in electrostatic potential occurs inside the membrane, defining Ψd. This is due to the presence of highly ordered molecules with a charge distribution characterized by a dipole or higher order multipoles inside the membrane.

It is important to clarify here that the electrostatic potential determined in Langmuir film experiments is usually called "surface potential". However, since it is a change in Volta potential differences, ΔV has contributions from all the electrostatic changes induced by the presence of the film. As previously mentioned, ΔV includes potential changes due to the dipoles from the water molecules. These molecules change their orientation from that at the clean air-water interface to that adopted when they hydrate the lipid polar head-groups. Ions also adopt different orientations in the presence of the film, especially for charged lipids, where Ψdl develops. When the film is composed of charged surfactants, Ψs contributions are also included in the electrostatic potential measured. Finally, the surfactant molecules orient their dipoles, generating Ψd, and contributing to the change measured in Volta potential difference.

The interaction of soluble ions with membranes may be affected in different manners by all the potentials mentioned. Surface potentials foster the adsorption of cationic peptides to membranes, as expected. This is demonstrated in Figure 2B for lipid monolayers and KR9C. This figure shows that the poly-arginine peptide induces higher perturbations in charged monolayers (pH > 7) than in neutral monolayers (pH < 6) [26]. This was also observed for the less charged MP1 peptide. As shown in Figure 2C, the maximal surface pressure at which the peptide inserts into monolayers (exclusion surface pressure) is higher for lipids with charged polar head groups (PS) than for neutral lipids (PC), considering the same hydrocarbon chains [36]. This preferential interaction was observed under conditions at which the Debye length is large, and thus, the surface charge is screened at large distances from the membrane, for instance, in pure water (red bars in Figure 2C), λ_D = 300 nm, implying that at 300 nm the potential is 1/e times that of the surface. The attractive effect of the membrane charge is reverted in the presence of salt. At 150 mM NaCl (green bars in Figure 2C), λ_D decreases to less than 1 nm, and the electrostatics becomes negligible, so that other effects emerge (phase state in this case, as will be discussed in the next section).

Regarding the transmembrane potential, computational simulations demonstrated that an imbalance caused by changes in the ionic composition of the aqueous solutions bathing the membrane promotes the translocation of a cationic peptide [37,38]. This is in line with the effect promoted by externally applied potentials using electrodes. The application of a potential difference between each side of a membrane promotes the migration of charged species through the membrane. The velocity of ion migration is determined by measuring the current, and the membrane conductivity is obtained, which depends on the particular ion, the membrane composition, and phase state.

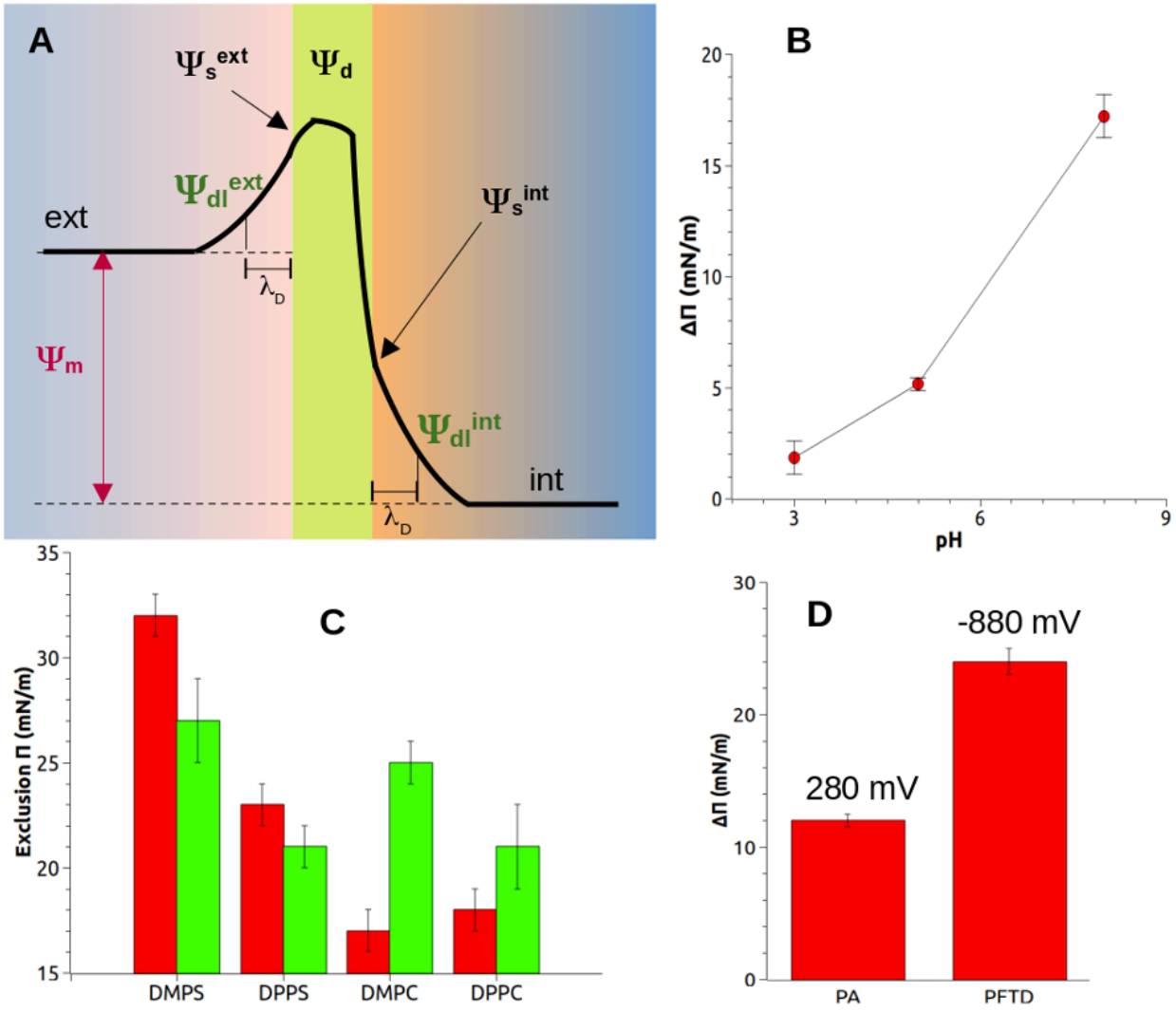

Figure 2. Membrane electrostatics and peptide-membrane interaction. A) Scheme indicating the transmembrane potential (Ψm), surface potential (Ψs), dipole potential (Ψd), potential drop at the diffuse layer (Ψdl), and Debye length (l_D). B) Increase in surface pressure due to the insertion of KR9C peptide into monolayers of palmitic acid, initially at 10 mN/m as a function of the pH of the aqueous solution. Adapted from [26]"ISSN":"15205827","abstract":"Cell-penetrating peptides (CPPs, with permission. C) Exclusion surface pressure for the peptide MP1 in monolayers of the indicated lipids over water (red) or NaCl 150 mM (green). Adapted from [36], with permission. D) Increase in surface pressure due to the insertion of KR9C peptide into monolayers of ionized palmitic acid or perfluorotetradecanoic acid initially at 20 mN/m. Adapted from [26]"ISSN":"15205827","abstract":"Cell-penetrating peptides (CPPs, with permission.

Both potentials discussed so far (transmembrane and surface potentials) markedly affect the adsorption and translocation of cationic peptides, as expected due to basic electrostatics. The influence of the dipole potential, however, has been less studied, despite it being known since 1969 that the permeation of hydrophobic cations and anions is affected by this potential [25]. Liberman and Topaly [39] compared the conductivity changes induced by the addition of fat-soluble anions or cations and discovered that to increase the conductivity of the membrane to a certain value required an approximately 10^5 times greater concentration of cations than anions. They attributed this very significant difference to the partition coefficient of fat-soluble ions, the coefficient for anions being 10^5 greater than that for cations, and hypothesized that the inner part of the bilayer membrane must be positively charged. Now it is accepted that the interior of lipid bilayers has a more positive charge density than the region of the polar headgroups, i.e., that Ψs have positive values for all lipid bilayers, which should be unfavorable for the insertion of cationic peptides. In order to test this, the insertion of KR9C into monolayers of different dipole potentials was studied. Figure 2D shows the increase in surface pressure due to peptide insertion into monolayers formed by two different fatty acids with similar surface charges and compaction. PA is a hydrogenated fatty acid, with dipole potentials of 200 – 300 mV, while PFTD is a perfluorinated

fatty acid, with negative values of the dipole potential (-200 – -900 mV) [38]. The results show that this little-explored membrane parameter largely affects peptide insertion, and thus, should be studied in depth. Dipole potential depends on membrane composition, phase state, and compaction.

3- Influence of membrane phase state in peptide-membrane interactions

In lipid bilayers, molecules interact through Van der Waals, hydrogen bonding, electrostatic and steric interactions, giving rise to an optimal molecule-molecule distance. Depending on the strength profile of the interaction, which defines the intermolecular spacing, the hydrocarbon chain and the polar head group may move and rotate to a greater or lesser degree, defining membrane mechanical properties such as fluidity, compressibility, and deformability [40,41]. Lipids with a long and saturated hydrocarbon chain (16 C or more) and an intermediate-sized polar head group, such as DPPS, DPPC, DPPG, or DPPA, form very compact bilayers, with low lateral motion and low fluctuation in the positions of the carbon atoms in the hydrocarbon chains. These membranes are in the so-called gel phase (G) at room temperature and have melting temperatures (Tm) from G to liquid-disordered (LD) phases of 40°C or higher (see Tables for Tm on the web page of Avanti Polar Lipids). In contrast, unsaturated lipids such as DOPC, or those with short saturated hydrocarbon chains (such as DLPG), form LD fluid phases at room temperature, with Tm values lower than 20°C.

In the presence of most sterols (cholesterol, ergosterol or phytosterols), membranes are also fluid but very compact, giving rise to the so-called liquid-ordered (LO) phase state. The characteristics of this phase state have been described [42]. Briefly, these membranes are fluid, with the diffusion coefficient of lipids being similar to those in the LD phase, but are very difficult to compress or bend, presenting low permeability. Hopanoids, a family of lipids synthesized only by some bacteria, are also able to induce a LO phase state in these sterol-lacking bacteria, and are thus sterol surrogates [43].

Soluble molecules are generally observed to be less prone to penetrate G or LO membranes than LD membranes, since the inclusion of the molecule implies a local compression of the membrane. This explains the low values for the exclusion pressures of MP1 into DPPS monolayers when the electrostatic attraction is screened (green bars in Figure 2C), as DPPS monolayers are very stiff with Tm = 54°C. Similarly, KR9C showed higher exclusion pressures for DPPC than for DOPC monolayers [29].

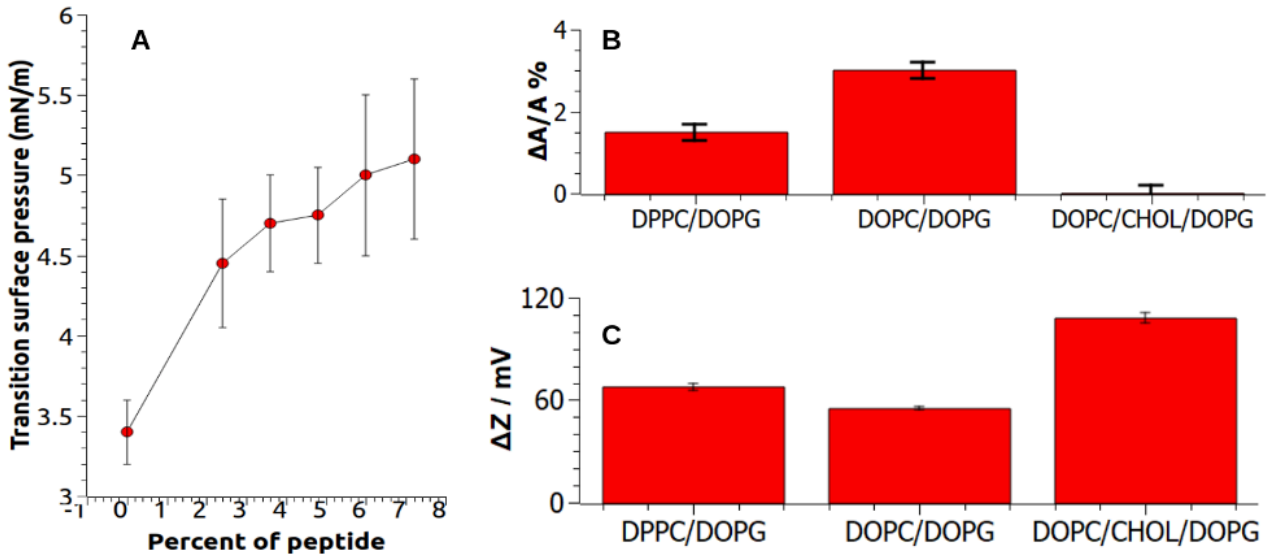

Figure 3. Membrane phase state and peptide-membrane interaction. A) Increase in surface pressure for the phase transition from a fluid to a rigid phase state induced by compression of DPPC monolayers with increasing amounts of MP1. Adapted from [44], with permission. B) Changes in monolayer area due to the insertion of KR9C into monolayers of the indicated compositions. C) Changes in the zeta potential of large unilamellar liposomes after adding KR9C to the solution. B) and C) were adapted from [29] with permission.

Besides the lower inclusion of molecules from solution, when peptides insert in membranes with phase coexistence they localize preferentially in the LD phase. Figure 3A shows that the transition surface pressure from expanded to compact phase state for DPPC monolayers increases as the amount of peptide in the monolayer increases, indicating that the peptide stabilizes the more expanded phase, and thus mixes preferentially with lipids in the expanded phase [44].

Despite the slight insertion of peptides into compact membranes, they may adsorb on the membrane-solution interface and alter membrane properties. As an example, Figure 3B shows the area change induced on monolayers at 30 mN/m due to the insertion of KR9C. The three lipid compositions present similar charge density. The peptide is added to the solution under monolayers initially at 30 mN/m. The larger the change in the area, the larger the perturbation promoted by peptide incorporation, which is detected in monolayers composed of unsaturated lipids (DOPG/DOPC) forming LD membranes. Membranes with cholesterol (LO phase) render no peptide incorporation, and consequently, no film area change is observed upon adding peptide to the media [29]. However, liposomes composed of DOPC/CHOL/DOPG show the greatest changes in zeta potential, which goes from negative to positive values due to peptide adsorption [29]. The preference for peptide adsorption to rigid membranes may be explained by considering electrostatics, since local charge density is usually higher in compact regions of the membrane than in relaxed regions. Another factor affecting the preferential adsorption of peptides on rigid membranes is the smaller decrease in entropy upon adsorption, as rigid membranes are already ordered before the adsorption, while order is induced by adsorption in disordered membranes [45,46].

4- The influence of the chemical composition of the lipid bilayer in peptide-membrane interactions

There is a great variety of lipids, and these are chemically diverse and present in various amounts and proportions. The question of why the universe of chemical structures of these molecules is so vast is currently unanswered, but it is clear that this is required since alterations of membrane lipid homeostasis are linked to various diseases [47].

Thus, not only is the phase state of membranes important but also their specific chemical identity, and even their minority components are subtly regulated. This is very relevant in the context of AMPs, since there is indisputable evidence that bacteria modify their membranes to reduce the lytic effects of these peptides. The physiological response of bacteria to AMPs involves changes in their lipid composition in terms of both head group and acyl chain structure, which significantly impact membrane properties such as net surface charge and membrane fluidity [9,48].

We therefore evaluated possible differences caused by lipid composition, using MP1 and LO membranes. The importance of the LO regions was first proposed in eukaryotic membranes. The formation of this phase state depends crucially on the ordering properties of sterols (cholesterol in mammals, ergosterol in fungi and phytosterols in plants). The induction of LO regions in eukaryotes has been considered a fundamental step during the evolution of cellular complexity. Conversely, it was suggested that bacteria and archaea do not require such a sophisticated organization of their cellular membranes. However, it was later discovered that many signal transduction, protein secretion, and transport processes in bacteria depend on the presence of LO phases [49]. This led to the search for sterol surrogates in bacteria, and hopanoids have been indicated as candidates. Hopanoids are diverse pentacyclic molecules derived from the cyclization of squalene, which shares the same hydrocarbon skeleton as the compound hopane. It was shown that diplopterol, the simplest bacterial hopanoid, is able to induce a LO phase with similar properties to that induced by other sterols [50–53], and hopanoids are now accepted as bacterial sterol surrogates, with the ability to order saturated lipids and to form a LO phase in model membranes.

We studied the interaction of the peptide MP1 with membranes containing cholesterol or diplopterol, in order to test the possible chemical sensitivity of the peptide in LO membranes. We found that MP1 permeates membranes with diplopterol more effectively than those with cholesterol (Figure 4A) [30]. Furthermore, monolayer perturbation by the peptide was stronger in membranes with diplopterol than with cholesterol, and the adsorption of the fluorescently labeled peptide was faster and more extensive on bilayers with diplopterol than those with cholesterol. In other words, MP1 is able to discriminate the chemical composition of LO membranes and to distinguish between mammal-like and bacterial-like compositions.

It has been proposed that in systems in which electrostatic effects can be neglected, as in this case (neutral membrane and low charged peptide), peptide aggregation in the membrane is driven by membrane deformations [54–56]. Therefore, subtle differences in membrane mechanical properties (which are not distinguished using biomimetics systems) may lead to differences in the mechanism of peptide-membrane interactions, and thus in the consequences of the interactions, as will be discussed in the next section.

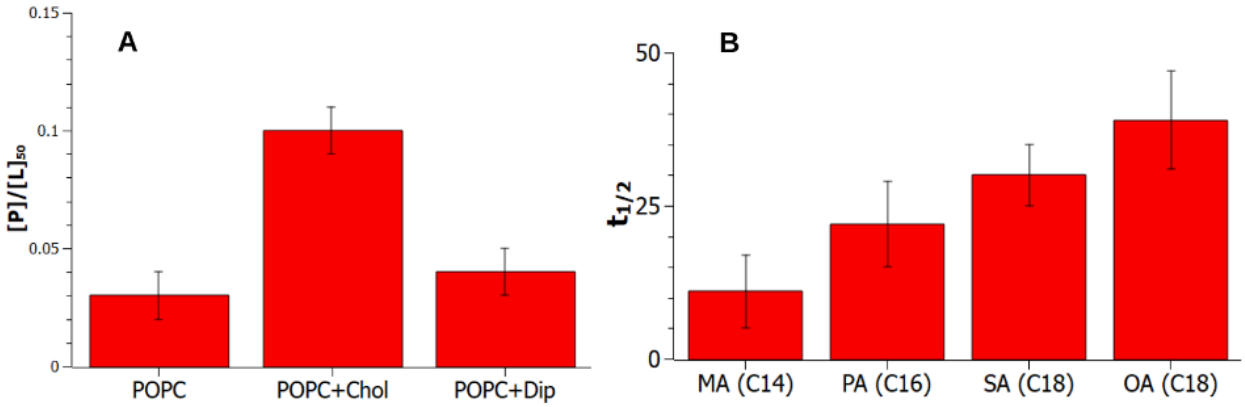

Figure 4. Membrane composition and peptide-membrane interaction. A) MP1-to-lipid molar ratio at which carboxyfluorescein leakage is 50%. Adapted from [30], with permission. B) Time for half insertion of KR9C into lipid monolayers. Adapted from [26]"ISSN":"15205827","abstract":"Cell-penetrating peptides (CPPs, with permission.

The polar groups of the lipid molecules are also important for the activity of cationic peptides. It has been shown that poly-arginine CPPs are chelated by the phosphate or the carboxylic acid of the polar head-groups of lipids, forming complexes that decrease the energy cost needed to internalize the peptide inside the membrane [11]. Thus, poly-arginine peptides show an increased affinity for membranes with lipids that contain these functional groups exposed for interaction. Aside from the lipid class, the hydrocarbon chain affects peptide-membrane interaction, influencing phase state, lipid motility, and the exposure of the functional groups. For instance, poly-arginine peptides were shown to penetrate POPG monolayers [57] and only adsorb without penetrating into DMPG monolayers [26]. We observed that the penetration rate for KR9C into membranes is faster when the membranes are composed of lipids with one hydrocarbon chain rather than with two [14]. In this regard, comparing different fatty acids, peptide insertion into monolayers is faster, the shorter the hydrocarbon chain, as shown in Figure 4B [26]). This may be explained as an adaptative mechanism for the insertion of this peptide inside the membrane, being favorable in energy terms to form a lipid-peptide complex with single-chain lipids than with lipids with two hydrocarbon chains.

5- Consequences of peptide-membrane interactions on the membrane properties

A clear consequence of the interaction of the peptide with membranes is the dramatic change in surface electrostatics when anionic membranes acquire a positive surface potential. This effect occurs even when the peptide does not incorporate into the membrane, permeate, or damage it, as shown in Figure 3C for DOPC/CHOL/DOPG membranes and KR9C.

Another clear effect that is detected in almost all membrane compositions for most AMPs is a change in the deformability of the membrane upon shape change. This property was studied in our laboratory for different membrane compositions faced with KR9C or MP1. Two methods were employed, both using GUVs: registration of thermal shape fluctuation, and kinetic retraction of membrane nanotubes.

Briefly, the analysis of shape fluctuations of membranes and vesicles is based on collecting time sequences of snapshots obtained by optical microscopy. The thermally induced fluctuations around equilibrium form are monitored, and the mean square values of shape deviations are determined. This method is less demanding from an experimental point of view because it is based on direct video microscopy observation of giant vesicles. A disadvantage is that, as the vesicles should exhibit visible fluctuations, this method cannot be applied to rigid vesicles. The difficulty of the method is in the analysis of the videos: first, the vesicle contour in the equator must be determined, and from the contour, the radius is obtained as a function of the polar angle for each frame in a video (Figure 5). This allows the amplitude of the shape fluctuation to be quantified, from which the bending rigidity is obtained. This procedure requires a software for image processing, which was developed by S. V. Amante and P. E. Scurti and is available for use at https://github.com/GatitoNegro/Determinacion-de-rigidez-de-biomembrana-usando-GUVs [58].

In biology, it is not only the energy cost of a process that is important, but also the velocity at which the process will happen. Therefore, as well as bending rigidity, viscosity terms are of interest. In this regard, membranes can be deformed with stress, and the kinetic relaxation will give an insight into both membrane rigidity and viscosity. For this analysis, we prepare membrane nanotubes from GUVs attached to the cover glass, separating the membrane from a micro-sphere adhered to the membrane by means of optical tweezers. The nanotube is stretched until the desired length is reached,

and then the laser is turned off. Dynamics for nanotube relaxation can be determined from videos of this process, by determining the position of the center of the GUV and the micro-sphere in each frame, giving rise to plots of nanotube length as a function of time. This allows us to determine a characteristic time for nanotube relaxation, as shown in Figure 6 [29,30].

In the case of KR9C, we observed different behaviors in the composition of the three membranes studied. Membranes in the LO phase were not affected by peptide adsorption, while rigid membranes ruptured after peptide addition. In contrast, in LD membranes, where peptides adsorbed and subsequently translocated, a softening of the membrane was detected using the latter method [29]. This implies that the CPP is not as innocuous for the membrane as is desirable for a CPP.

MP1 showed more drastic results, leading to membrane rupture for LD membranes and LO membranes with cholesterol. Membranes in LO phases induced by diplopterol showed an interesting behavior: immediately after adding the peptide, a fast softening was observed, and subsequently, an increase in rigidity was detected. Therefore, in the longer term, the membranes were similar to those in the absence of the peptide. This was detected using thermal fluctuations for high MP1 concentrations (visible fluctuations were registered for 6 μM peptide, see Figure 5), and by the kinetics of nanotube retraction for 0.6 μM peptide, as summarized in Figure 6.

Based on these results (Figures 5 and 6) and others, we propose the mechanism schematized in the graphical abstract. At short times, a low amount of peptide accumulated in the external hemilayer in a diluted regime. This first stage is followed by the formation of peptide dimers/multimers until pores/defects form, allowing vesicle leakage and the passage of the peptide to the vesicle lumen. The pores/defects may be formed by lipids and peptides (disordered toroidal pores), or with one peptide at each hemilayer, since the thickness of the bilayers is twice the length of the peptide. When peptides are in the outer hemilayer in a diluted regime, they may increase the membrane's spontaneous curvature because, at this stage, membranes would be asymmetric, with peptides only in the external leaflet. When peptides reach a threshold concentration at the interface, they would form dimers/multimers, and eventually, pores. This is accompanied by a decrease in the characteristic time for nanotube retraction, which could be due to an increase in the spontaneous curvature (since membrane symmetry would be recovered). In addition, a decrease in shear viscosity and an increase in the bending rigidity of the membrane may occur in the presence of pores.

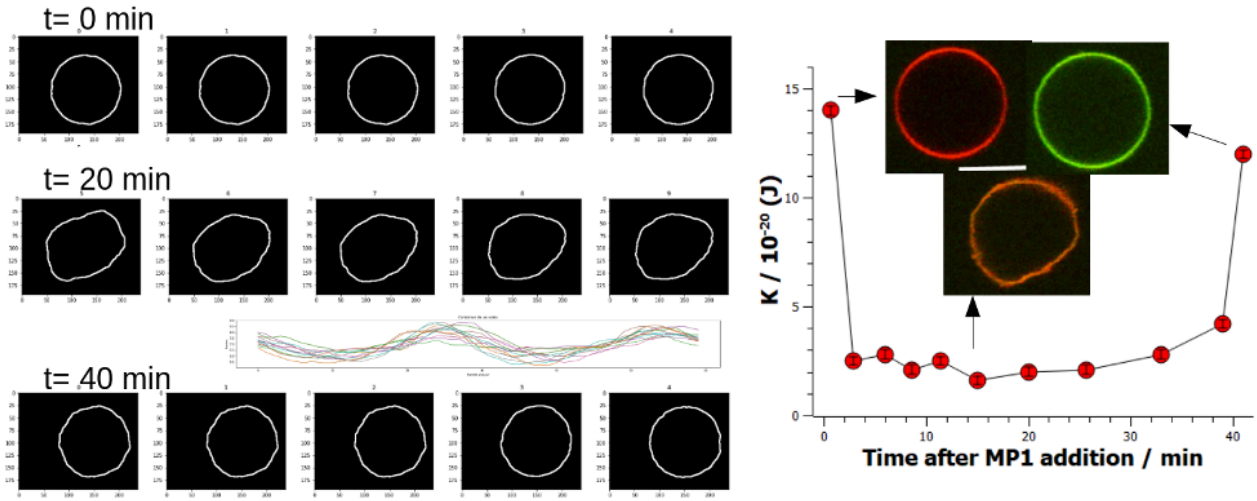

Figure 5. Consequences of membrane-peptide interaction on membrane bending. Vesicles are composed of POPC/diplopterol (6:4) in the presence of 6 mM MP1. Left: Sequential images recorded immediately before peptide addition and at 20 or 40 min after adding the peptide. Resolution: 0.1 mm/px. Central plot: vesicle radius as a function of the polar angle for each frame at 20 min after adding the peptide. Right: Bending rigidity as a function of time after peptide addition, determined from the thermal shape fluctuations. Inserted images: three selected frames for different times after peptide addition. Images are the merge of red and green channels, representing membrane and peptide, respectively. Scale bar: 10 mm.

In summary, membrane behavior in the presence of the peptide MP1 is very different in the case of cholesterol-containing membranes than in that of diplopterol-containing membranes, despite both membranes being initially similar. This is important since it may be one of the reasons for the different action of peptide in mammal than in bacterial cells and this is now being studied deeply.

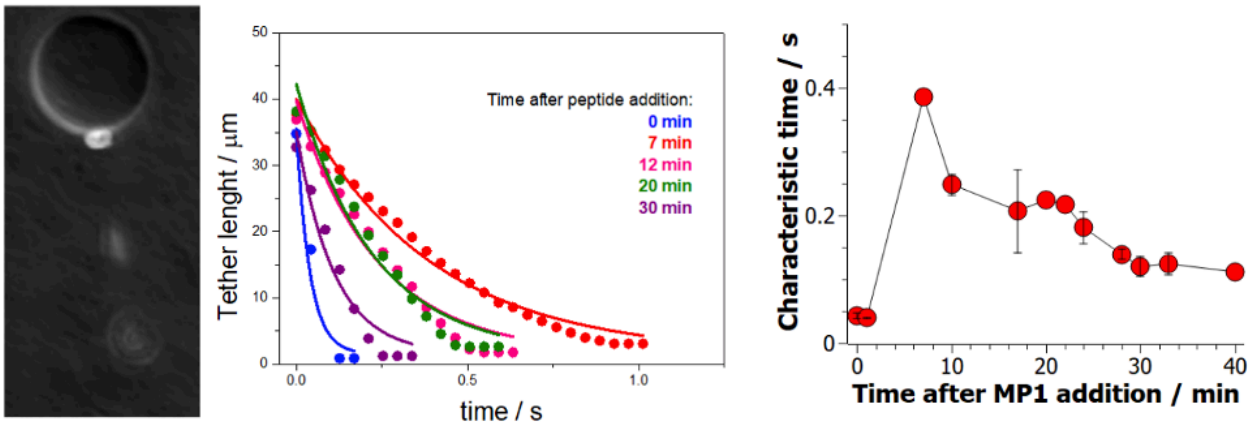

Figure 6. Consequences of membrane-peptide interaction on membrane bending. Vesicles are composed of POPC/diplopterol (6:4) in the presence of 0.6 mM MP1. Left: Accumulated images showing the motion of a bead attached to the tip of a membrane nanotube. Center: Representative data for nanotube retraction of tethers extracted from a GUV after the indicated times of adding the peptide. Right: Characteristic time for the kinetics of nanotube retraction as a function of time after peptide addition. Adapted from [30], with permission.

6- Cell membranes

As already mentioned, it is proposed that cell membranes are very dynamic and heterogeneous in regard to their composition, and consequently, local electrostatics and mechanical properties will dynamically vary from one region to another of the membrane. It was shown in our laboratory that hopanoid-lacking and sterol-lacking bacteria increased their permeability, as well as their tolerance to traditional antibiotics that act at the membrane level, upon preincubation with the sterol, cholesterol, or the hopanoid, diplopterol. This indicates that the lipids are incorporated from the media by the bacteria and included in their membranes, affecting membrane properties [52]. These bacteria also showed an increased tolerance toward MP1 (Figure 7), and this effect was higher in bacteria incubated with cholesterol than with diplopterol [30]. Our studies indicate that both lipids protect cells from the action of MP1, but not to the same degree. This result is in line with those found in the biomimetic systems previously discussed, and points to the importance of cholesterol as a key factor for cell distinction by AMPs. The presence of this sterol may help to explain the high resistance of red cells to the lysis induced by MP1, with 50% hemolysis at peptide concentrations above 0.1 mM. In comparison, the peptide concentration needed for provoking the death of 50% of a *Pseudomonas aeruginosa* culture is 1.5 µM (unpublished results). Concentrations as low as 2 µM MP1 cause an 80% decrease of *Pseudomonas aeruginosa* population, but not hemolysis (Figure 8).

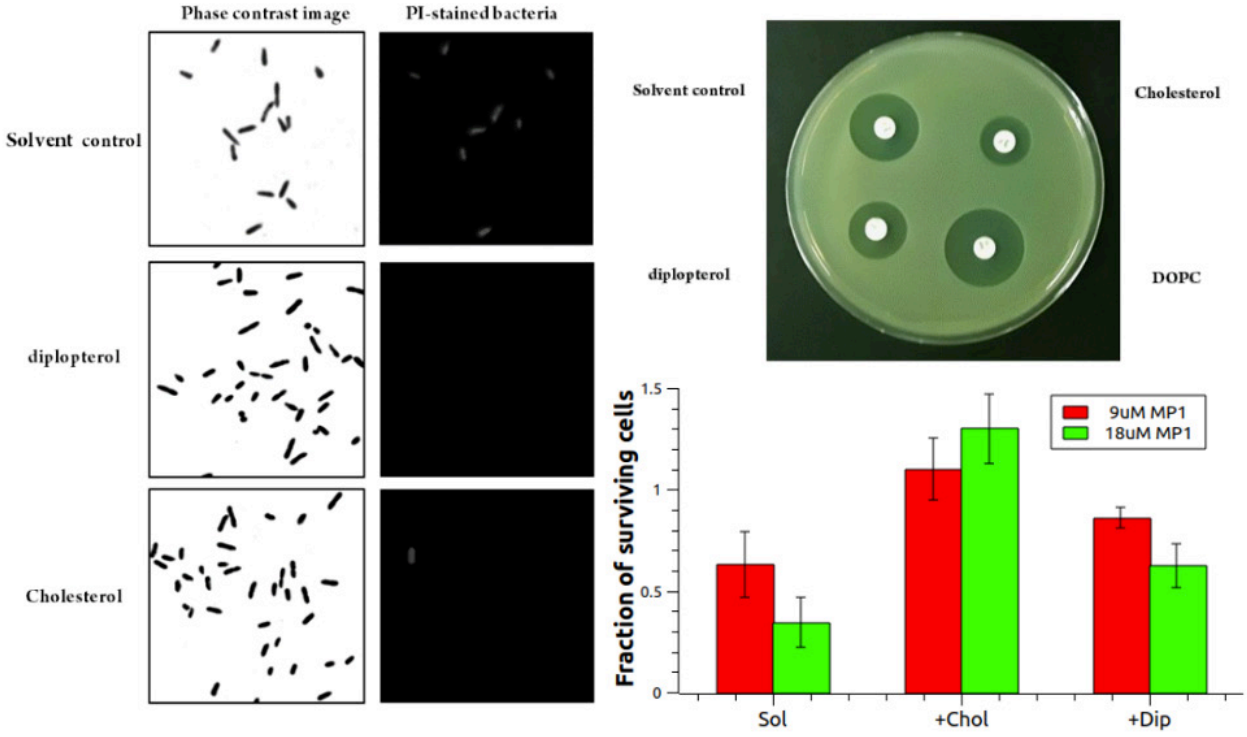

Figure 7. Cell membranes and peptide-membrane interaction. Left images: permeability of *P. aeruginosa* exposed to chloroform:methanol, diplopterol or cholesterol dissolved in the solvent. Permeability was determined with propidium iodide. Right image: disk diffusion test with imipenem embedded with cholesterol, diplopterol, DOPC or the solvent mixture (chloroform:methanol). Plot: Fraction of surviving cells incubated in the solvent (Sol), or a solution of cholesterol (+Chol), or diplopterol (+Dip) after 3 h of exposure to 9 μM (red) or 18 μM (green) of MP1. Adapted from [30] and [52], with permission.

It is interesting to note here that, unlike reports from other AMPs, MP1 appears not to sense membrane electrostatics. Bacteria have a higher proportion of anionic lipids than mammal cells, and it has been proposed that AMPs differentiate membrane targets from others due to electrostatic interactions. However, MP1 slightly alters the membrane surface charge upon adsorption to neutral membranes [30], and does not alter the surface charge of *Pseudomonas aeruginosa* (unpublished results). Besides, bacteria death is similar in media with high salt content to that in media without salt (Figure 8), also suggesting a non-electrostatic peptide-membrane attraction.

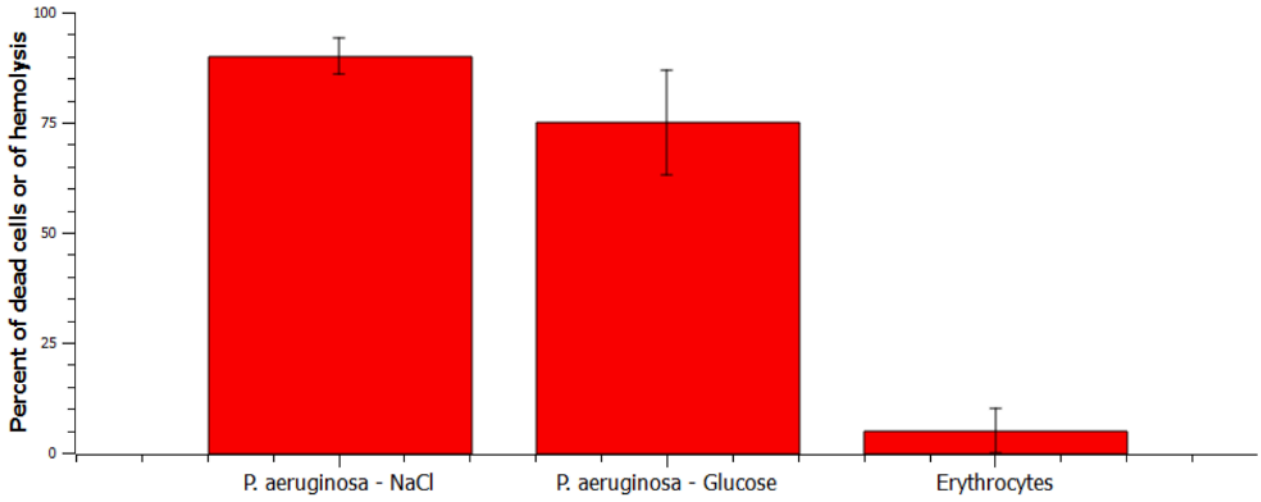

Figure 8. Cell membranes and peptide-membrane interaction. Percentage of cell death or hemolysis for cells exposed to 2 mM MP1. Cells correspond to *P. aeruginosa* suspended in 0.15 M NaCl or 0.3 M glucose, or to human erythrocytes.

Conclusions

Peptide-membrane interactions have been widely studied using both biomimetic systems and cells. Despite some progress, details about the mechanisms involved are still unknown. Of particular importance are the reasons for the higher interaction and consequent peptide-induced lysis of bacteria compared to mammal cells, since this is the most important parameter for using peptides in therapy.

A second important factor to be understood in order to use peptides in therapy is what happens at sub-lethal peptide concentrations. This is of paramount importance to avoid the acquisition of resistance by bacteria.

Our studies show that all membrane properties modulate peptide affinity. Anionic membranes show an enhanced interaction with cationic peptides due to electrostatic interactions but, at physiological ionic strength, the phase state becomes equally or even more important. Phase state defines the degree of incorporation of the peptide, and although the surface affinity may be higher to liquid-ordered membranes, peptides are usually not able to penetrate these membranes. For membranes with comparable charge density and in the same phase state, chemical composition subtly modulates peptide affinity.

Not only do membrane-peptide affinity and the degree of peptide penetration depend on membrane properties, but also the fate of the membrane subjected to the presence of the peptide. The same peptide can exert a softening effect, promote membrane lysis, or not affect the membrane, depending on membrane characteristics.

Since cell membranes are not homogeneous, but with patches of different characteristics coexisting in a dynamic fashion, peptides may cause different effects simultaneously, and the whole picture is complex. Therefore, an understanding of the mechanism and regulation of peptide-membrane interactions in a simple system is required, as well as the potential extrapolation of these results to cell membranes in living organisms.

Bibliography.

[1] S.J. Singer, G.L. Nicolson, The fluid mosaic model of the structure of cell membranes., Science. 175 (1972) 720–31. https://doi.org/10.1126/science.175.4023.720.

[2] G.L. Nicolson, The Fluid - Mosaic Model of Membrane Structure: Still relevant to understanding the structure, function and dynamics of biological membranes after more than 40 years, Biochim. Biophys. Acta - Biomembr. 1838 (2014) 1451–1466. https://doi.org/10.1016/j.bbamem.2013.10.019.

[3] A. Kusumi, T.K. Fujiwara, R. Chadda, M. Xie, T.A. Tsunoyama, Z. Kalay, R.S. Kasai, K.G.N. Suzuki, Dynamic organizing principles of the plasma membrane that regulate signal transduction: Commemorating the fortieth anniversary of singer and nicolson's fluid-mosaic model, Annu. Rev. Cell Dev. Biol. 28 (2012) 215–250. https://doi.org/10.1146/annurev-cellbio-100809-151736.

[4] E.A. Evans, Structure and Deformation Properties of Red Blood Cells: Concepts and Quantitative Methods, Methods Enzymol. 173 (1989).

[5] N. Malanovic, L. Marx, S.E. Blondelle, G. Pabst, E.F. Semeraro, Experimental concepts for linking the biological activities of antimicrobial peptides to their molecular modes of action, Biochim. Biophys. Acta - Biomembr. 1862 (2020) 183275. https://doi.org/10.1016/j.bbamem.2020.183275.

[6] S.T. Henriques, M.N. Melo, M.A.R.B. Castanho, Cell-penetrating peptides and antimicrobial peptides: How different are they?, Biochem. J. 399 (2006) 1–7. https://doi.org/10.1042/BJ20061100.

[7] I. Alves, A. Walrant, C. Bechara, S. Sagan, Is There Anybody in There? On The Mechanisms of Wall Crossing of Cell Penetrating Peptides, Curr. Protein Pept. Sci. 13 (2012) 658–671. https://doi.org/10.2174/138920312804142174.

[8] M. Di Pisa, G. Chassaing, J.M. Swiecicki, Translocation mechanism(s) of cell-penetrating peptides: Biophysical studies using artificial membrane bilayers, Biochemistry. 54 (2015) 194–207. https://doi.org/10.1021/bi501392n.

[9] H.G. Sahl, Y. Shai, Bacterial resistance to antimicrobial peptides, Biochim. Biophys. Acta - Biomembr. 1848 (2015) 3019–3020. https://doi.org/10.1016/j.bbamem.2015.08.009.

[10] H.J. Kaiser, M.A. Surma, F. Mayer, I. Levental, M. Grzybek, R.W. Klemm, S. Da Cruz, C. Meisinger, V. Müller, K. Simons, D. Lingwood, Molecular convergence of bacterial and eukaryotic surface order, J. Biol. Chem. 286 (2011) 40631–40637. https://doi.org/10.1074/jbc.M111.276444.

[11] H.D. Herce, A.E. Garcia, M.C. Cardoso, Fundamental molecular mechanism for the cellular uptake of guanidinium-rich molecules, J. Am. Chem. Soc. 136 (2014) 17459–17467. https://doi.org/10.1021/ja507790z.

[12] H.D. Herce, A.E. Garcia, J. Litt, R.S. Kane, P. Martin, N. Enrique, A. Rebolledo, V. Milesi, Arginine-rich peptides destabilize the plasma membrane, consistent with a pore formation translocation mechanism of cell-penetrating peptides, Biophys. J. 97 (2009) 1917–1925. https://doi.org/10.1016/j.bpj.2009.05.066.

[13] B.M. Souza, M.A. Mendes, L.D. Santos, M.R. Marques, L.M.M. César, R.N. a Almeida, F.C. Pagnocca, K. Konno, M.S. Palma, Structural and functional characterization of two novel peptide toxins isolated from the venom of the social wasp Polybia paulista, Peptides. 26 (2005) 2157–2164.

[14] M.A. Via, N. Wilke, L.S. Mayorga, M.G. Del Pópolo, Surface charge density and fatty acids enhance the membrane permeation rate of CPP-cargo complexes, Soft Matter. 16 (2020) 9890–9898. https://doi.org/10.1039/d0sm00673d.

[15] N.B. Leite, D. dos Santos Alvares, B.M. de Souza, M.S. Palma, J. Ruggiero Neto, Effect of the aspartic acid D2 on the affinity of Polybia-MP1 to anionic lipid vesicles, Eur. Biophys. J. 43 (2014) 121–30.

[16] M.P. Dos Santos Cabrera, D.S. Alvares, N.B. Leite, B. Monson De Souza, M.S. Palma, K.A. Riske, J. Ruggiero Neto, New insight into the mechanism of action of wasp mastoparan peptides: Lytic activity and clustering observed with giant vesicles, Langmuir. 27 (2011) 10805–10813.

[17] P. Mueller, D.O. Rudin, H.T. Thien, W.C. Wescott, Reconstitution of Cell Membrane Structure in vitro and its transformation into an Excitable System, Nat. Int. J. Sci. 196 (1962) 1048–1050.

[18] A.D. BANGHAM, B.A. PETHICA, G. V. SEAMAN, The charged groups at the interface of some blood cells., Biochem. J. 69 (1958) 12–19. https://doi.org/10.1042/bj0690012.

[19] Y.-H.M. Chan, S.G. Boxer, Model Membrane Systems and Their Applications State of the field, Curr. Opin. Chem. Biol. 11 (2007) 581–587. https://www.ncbi.nlm.nih.gov/pmc/articles/PMC2196400/pdf/nihms35927.pdf.

[20] A. Mangiarotti, N. Wilke, Energetics of the Phase Transition in Free-Standing versus Supported Lipid Membranes., J. Phys. Chem. B. 119 (2015) 8718–24.

[21] A. Mangiarotti, B. Caruso, N. Wilke, Phase coexistence in films composed of DLPC and DPPC: A comparison between different model membrane systems, Biochim. Biophys. Acta - Biomembr. 1838 (2014) 1823–1831. http://www.sciencedirect.com/science/article/pii/S0005273614000765 (accessed May 26, 2017).

[22] N. Wilke, Lipid Monolayers at the Air–Water Interface: A Tool for Understanding Electrostatic Interactions and Rheology in Biomembranes, in: Adv. Planar Lipid Bilayers Liposomes, 1st ed., Elsevier Inc., 2014: pp. 51–81.

[23] N. Wilke, Monomolecular Films of Surfactants with Phase-coexistence: Distribution of the Phases and Their Consequences, in: Compr. Guid. Nanocoatings Technol. Charact. Reliab., 2015.

[24] G.L. Gaines, Insoluble monolayers at liquid-gas interfaces, Interscience Publishers, New York, 1966.

[25] R.J. Clarke, The dipole potential of phospholipid membranes and methods for its detection., Adv. Colloid Interface Sci. 89–90 (2001) 263–81. https://doi.org/10.1016/S0001-8686(00)00061-0.

[26] M.A. Via, M.G. Del Pópolo, N. Wilke, Negative Dipole Potentials and Carboxylic Polar Head Groups Foster the Insertion of Cell-Penetrating Peptides into Lipid Monolayers, Langmuir. 34 (2018). https://doi.org/10.1021/acs.langmuir.7b04038.

[27] R.A. Demel, W.S.M. Geurts van Kessel, R.F.A. Zwaal, B. Roelofsen, L.L.M. van Deenen, Relation between various phospholipase actions on human red cell membranes and the interfacial phospholipid pressure in monolayers, BBA - Biomembr. 406 (1975) 97–107.

[28] D. Marsh, Lateral pressure in membranes, Biochim. Biophys. Acta - Rev. Biomembr. 1286 (1996) 183–223.

[29] M.A. Crosio, M.A. Via, C.I. Cámara, A. Mangiarotti, M.G. Del Pópolo, N. Wilke, Interaction of a polyarginine peptide with membranes of different mechanical properties, Biomolecules. 9 (2019). https://doi.org/10.3390/biom9100625.

[30] D.S. Alvares, M.R. Monti, J. Ruggiero Neto, N. Wilke, The antimicrobial peptide Polybia-MP1 differentiates membranes with the hopanoid, diplopterol from those with cholesterol, BBA Adv. 1 (2021) 100002. https://doi.org/10.1016/j.bbadva.2021.100002.

[31] D.S. Alvares, N. Wilke, J. Ruggiero Neto, Effect of N-terminal acetylation on lytic activity and lipid-packing perturbation induced in model membranes by a mastoparan-like peptide, Biochim. Biophys. Acta - Biomembr. 1860 (2018) 737–748. https://doi.org/10.1016/j.bbamem.2017.12.018.

[32] C.I. Cámara, F.E. Lurgo, M.L. Fanani, N. Wilke, Mechanical Stability of Lipid Membranes Decorated with Dextran Sulfate, ACS Omega. 3 (2018) 11673–11683. https://doi.org/10.1021/acsomega.8b01537.

[33] D.S. Alvares, T.G. Viegas, J. Ruggiero Neto, The effect of pH on the lytic activity of a synthetic mastoparan-like peptide in anionic model membranes, Chem. Phys. Lipids. 216 (2018) 54–64. https://doi.org/10.1016/j.chemphyslip.2018.09.005.

[34] V.V. Galassi, N. Wilke, On the coupling between mechanical properties and electrostatics in biological membranes, Membranes (Basel). 11 (2021) 1–24. https://doi.org/10.3390/membranes11070478.

[35] J.M. Kleijin, H.P. van Leeuwen, Electrostatic and Electrodynamic Properties of Biological Interphases, in: Phys. Chem. Biol. Interfaces, 2000: pp. 49–83.

[36] D.S. Alvares, N. Wilke, J. Ruggiero Neto, M.L. Fanani, The insertion of Polybia-MP1 peptide into phospholipid monolayers is regulated by its anionic nature and phase state, Chem. Phys. Lipids. 207 (2017) 38–48. https://doi.org/10.1016/j.chemphyslip.2017.08.001.

[37] D. Andelman, F. Broçhard, J.-F. Joanny, Phase transitions in Langmuir monolayers of polar molecules, J. Chem. Phys. 86 (1987) 3673.

[38] M.A. Via, J. Klug, N. Wilke, L.S. Mayorga, M.G. Del P´opoloa, Interfacial electrostatic potential modulates the insertion of cell- penetrating-peptides into lipid bilayers†, Phys. Chem. Chem. Phys. 3 (2018) 10715–10722. https://doi.org/10.1039/b000000x.

[39] E.A. Liberman, V.P. Topaly, Permeability of biomolecular phospholipid membranes for fat-soluble ions., Biofizika. (1969) 452–61.

[40] T. Heimburg, Thermal Biophysics of Membranes, 2007.

[41] O.G. Mouritsen, L.A. Bagatolli, Life as a Matter of Fat: Lipids in a Membrane Biophysics Perspective, 2016. https://doi.org/10.13140/RG.2.1.1190.4723.

[42] O.G. Mouritsen, M.J. Zuckermann, What`s So Special About Cholesterol, Lipids. 39 (2004) 1101–1113.

[43] B.J. Belin, Di.K. Newman, N. Busset, E. Giraud, A. Molinaro, A. Silipo, Di.K. Newman, Hopanoid lipids: From membranes to plant-bacteria interactions, Nat. Rev. Microbiol. 16 (2018) 304–315. https://doi.org/10.1038/nrmicro.2017.173.

[44] D.S. Alvares, M.L. Fanani, J. Ruggiero Neto, N. Wilke, The interfacial properties of the peptide Polybia-MP1 and its interaction with DPPC are modulated by lateral electrostatic attractions, Biochim. Biophys. Acta - Biomembr. 1858 (2016) 393–402. https://doi.org/10.1016/j.bbamem.2015.12.010.

[45] M.L. Fanani, N. Wilke, Regulation of phase boundaries and phase-segregated patterns in model membranes, Biochim. Biophys. Acta - Biomembr. 1860 (2018) 1972–1984. https://doi.org/10.1016/j.bbamem.2018.02.023.

[46] C.I. Cámara, N. Wilke, Interaction of dextran derivatives with lipid monolayers and the consequential modulation of the fi lm properties, Chem. Phys. Lipids. 204 (2017) 34–42.

[47] T. Harayama, H. Riezman, Understanding the diversity of membrane lipid composition, Nat. Rev. Mol. Cell Biol. 19 (2018) 281–296. https://doi.org/10.1038/nrm.2017.138.

[48] J.M. Henderson, N.S. Iyengar, K.L.H. Lam, E. Maldonado, T. Suwatthee, I. Roy, A.J. Waring, K.Y.C. Lee, Beyond electrostatics: Antimicrobial peptide selectivity and the influence of cholesterol-mediated fluidity and lipid chain length on protegrin-1 activity, Biochim. Biophys. Acta - Biomembr. (2019). https://doi.org/10.1016/j.bbamem.2019.04.011.

[49] M. Bramkamp, Exploring the Existence of Lipid Rafts in Bacteria, Microbiol. Mol. Biol. Rev. 79 (2015) 81–100.

[50] J.P. Saenz, E. Sezgin, P. Schwille, K. Simons, Functional convergence of hopanoids and sterols in membrane ordering, Proc. Natl. Acad. Sci. 109 (2012) 14236–14240. https://doi.org/10.1073/pnas.1212141109.

[51] J.P. Sáenz, D. Grosser, A.S. Bradley, T.J. Lagny, O. Lavrynenko, M. Broda, K. Simons, Hopanoids as functional analogues of cholesterol in bacterial membranes, Proc. Natl. Acad. Sci. 112 (2015) 11971–11976. https://doi.org/10.1073/pnas.1515607112.

[52] A. Mangiarotti, D.M. Genovese, C.A. Naumann, M.R. Monti, N. Wilke, Hopanoids, like sterols, modulate dynamics, compaction, phase segregation and permeability of membranes, Biochim. Biophys. Acta - Biomembr. 1861 (2019) 183060. https://doi.org/10.1016/j.bbamem.2019.183060.

[53] A. Mangiarotti, V. V. Galassi, E.N. Puentes, R.G. Oliveira, M.G. Del Pópolo, N. Wilke, Hopanoids Like Sterols Form Compact but Fluid Films, Langmuir. 35 (2019) 9848–9857. https://doi.org/10.1021/acs.langmuir.9b01641.

[54] A. Zemel, A. Ben-Shaul, S. May, Membrane Perturbation Induced by Interfacially Adsorbed Peptides, Biophys. J. 86 (2004) 3607–3619.

[55] A. Zemel, A. Ben-Shaul, S. May, Perturbation of a lipid membrane by amphipathic peptides and its role in pore formation, Eur. Biophys. J. 34 (2005) 230–242. https://doi.org/10.1007/s00249-004-0445-9.

[56] A. Zemel, A. Ben-shaul, S. May, Modulation of the Spontaneous Curvature and Bending Rigidity of Lipid Membranes by Interfacially Adsorbed Amphipathic Peptides, J. Phys. Chem. B. 112 (2008) 6988–6996.

[57] N.A. Alhakamy, A. Kaviratna, C.J. Berkland, P. Dhar, Dynamic measurements of membrane insertion potential of synthetic cell penetrating peptides, Langmuir. 29 (2013) 15336–15349. https://doi.org/10.1021/la403370p.

[58] P.E. Amante, Sofia Veronica; Scurti, Determinación de la rigidez a la flexión de biomembranas mediante el análisis de la fluctuación de su forma a partir de imágenes provenientes de videos de microscopía. *Proyecto integrador para optar al título de Ingeniería Biomédica.* Universidad Nacional de Córdoba, 2022.

Bios

Natalia Wilke

I am Bachelor in Chemistry 1998 ("Premio Universidad" best average award), and PhD in Chemical Science in 2003 at the National University of Córdoba. I was awarded Fellowships by the Fullbright Foundation (2007, USA) and by the Von Humboldt Foundation (Germany, 2015-2017) to carry out studies on assembling and use of optical tweezers in biophysics, I implemented these techniques in Córdoba in 2010.

I am Principal Researcher (CONICET). I lead a research group that inquires about how different organisms regulate the biophysical properties of their membranes, and how they adapt to stress situations. We use several biophysical techniques (optical tweezers among them), and our research focuses on both artificial biomembranes and living micro-organisms.. In 2021 I received the "Premio "Houssay 2021 (biological and biochemical science)" from the National Department for Science, Technology and Innovation. A complete list of my publications can be obtained at:

https://www.conicet.gov.ar/new_scp/detalle.php?keywords=&id=24476&articulos=yes or https://scholar.google.com/citations?user=2Fnxr8wAAAAJ&hl=es&oi=ao

Together with research, teaching was important in my carrier. I am currently Full Professor and vice-director of the Bachelor's degree in Chemistry (National University of Córdoba).

Science Reviews
from the end of the world

Vol. 2, No. 3, October 2023 // pp. 39-51 /

Magnetic nanoparticles for purification of biomolecules: challenges and opportunities

Claudia Rodríguez Torres*[1], Luciana Juncal[1], Elisa De Sousa[1], Odín Vazquez Robaina[1], Natalia Capriotti[2], Karen Salcedo Rodríguez[1], Alberto Nicolás Barrera Illanes[2], Nicolás Mele[1], Carla Layana[2], Lautaro Bracco[3], Juan Pablo Malito[3], Pedro Mendoza Zélis[1], Sheila Ons[2]

[1] *IFLP-CCT-La Plata-CONICET and Departamento de Física, Facultad de Ciencias Exactas, C. C. 67, Universidad Nacional de La Plata, 1900 La Plata, Argentina*
[2] *Laboratorio de Neurobiología de Insectos (LNI), Centro Regional de Estudios Genómicos, Facultad de Ciencias Exactas, Universidad Nacional de La Plata, CENEXA, CONICET, La Plata, Buenos Aires, Argentina*
[3] *INCUINTA, Centro Nacional de Investigaciones Agropecuarias, INTA, Hurlingham, Buenos Aires, Argentina*

** Corresponding author. E-mail: torres@fisica.unlp.edu.ar*

Abstract

The purification and/or concentration of biomolecules from complex mixtures constitutes one of the fundamental steps in the processes involved in biotechnology and, in particular, in the diagnostic methods of human and veterinary diseases. Most purification procedures are based on the interaction between a solid phase and the biomolecule to be purified (RNA, DNA, proteins, etc.), involving several steps with dependence on the method used. Among the different approaches, the use of functionalized magnetic nanoparticles (MNPs) has become of increasing interest due to its efficiency, practicality and the possibility of automation. In this work we present preliminary results on the use of MNPs for the purification of nucleic acids and recombinant proteins.

Keywords: silica coated nanoparticles, nucleic acids, purification methods, recombinant proteins, magnetic nanoparticles

Introduction

In recent decades, the frequency of emerging virus outbreaks has increased, probably as a result of human activity on the environment and the consequent increase in risk of zoonotic transmission. Due to globalization, emerging viruses have a pandemic potential, which has materialized in the case of SARS-CoV2. A pandemic, such as the one experienced, generates an overload of the health systems all over the world, as well as a strong economic and social impact with long-term consequences. Also, climate change has expanded the distribution range of arthropod vectors of pathogenic agents, such as mosquitoes, kissing bugs and ticks. In that context, the inputs for the prevention of the expansion of diseases (diagnosis, treatment and immunization) are scarce globally. Therefore, it is crucial for the sanitary sovereignty of the countries to count with technologies that can allow rapid innovation and national production of supplies for timely diagnosis. In the case of COVID-19, as well as other diseases, although there are certain diagnostic methods that do not require purification of the sample, those more sensitive are based on the identification of viral RNA/DNA by

means of qPCR or isothermal amplifications. For these methods, a purification step of the genetic material is necessary. This purification step is a limitant in the processivity of diagnosis. For this reason, it is necessary to count with robust, high-performance, cost-efficient and locally produced purification methods. This is necessary for the diagnosis of both infectious and genetic diseases, genomics and also in research laboratories.

Currently available commercial kits present a number of drawbacks, such as low throughput in terms of samples per hour, high cost/efficiency ratio, need for specific equipment (such as refrigerated centrifuges), and/or low disponibility in moments of high global demand. Magnetic nanoparticles (MNPs) functionalized in order to efficiently and specifically adsorb biological molecules have aroused growing interest, in view of its low production cost and the possibility of being separated by a magnetic field. Iron oxide MNPs have a large surface area relative to their volume, and offer physicochemical properties that make them ideal candidates for purification in diagnostics and in the pharmaceutical industry, as well as for applications such as immunotherapy, controlled release of drugs (drug delivery), cancer therapy by hyperthermia, etc [1,2]. In particular, the MNPs of iron oxide have a superparamagnetic behavior, which allows the separation of biological molecules adsorbed by applying a magnetic field. This type of particle has been used to adsorb proteins, nucleic acids, lipids, and polysaccharides (reviewed recently in reference [3]).

The purification of recombinant proteins is relevant in a multiplicity of applications, both in the pharmaceutical industry and in biotechnology. For this, the use of labels (tag) of Histidine (His6) in affinity chromatography is a gold standard, and is based on the strong affinity of this sequence by metals such as Ni^{2+}, Cu^{2+}, Zn^{2+} and Co^{2+}. The use of MNPs coated with any of these metals would be a more efficient, fast, economical and sustainable method than chromatography [4, 5].

In this work we present results regarding the efficiency of MNPs for the purification of nucleic acids and preliminary studies using the recombinant anti-Spike-SARS-CoV nanobody protein as a model.

1. Nucleic acid purification

1.1 Synthesis of silica coated magnetite nanoparticles

Magnetic Fe_3O_4 nanoparticles (core, MNPs) were prepared by co-precipitation method from a mixture of $FeCl_2$ and $FeCl_3$ (1:2 molar ration) upon addition of NH_4OH (25% wt) [6]. The resulting black product (bare MNPs) was collected with a magnet and washed several times with deionized water. Subsequently, as-prepared bare MNPs were dispersed in ethanol after 30 minutes of sonication. The reaction mixture was placed in a round bottom flask and ammonium hydroxide solution (25% wt) was added. The SiO_2 functionalization was performed using the protocol provided by [7]. Briefly, SiO_2 functionalization was achieved by the hydrolysis of tetraethyl orthosilicate (TEOS) that was added into the solution mixture dropwise. The mixture was heated up to 80 °C under vigorous magnetic stirring allowing the formation of silica layers on the surface of MNPs. Afterwards, the silica-coated MNPs (MNPs@SiO_2) were collected with a magnet and then washed with ethanol first and then deionized water several times to remove residual TEOS.

1.2 Physico chemical characterization

Several batches of MNPs and MNPs@SiO_2 were prepared following the procedure described above. The quality controls did not show significant differences in the structure and properties of the particles of the different batches, indicating the reproducibility of the method of synthesis. The MNPs@SiO_2 total concentrations (wt/vol) in the colloids were estimated from the weighted mass of dried samples, and the Fe concentration in the samples was determined by means of the so-called thiocyanate method [8]. The silica percentage of microparticles used for nucleic acid purifications is around 40 %. Dynamic light scattering (DLS, Malvern ZetasizerNanoZS) was used to measure the hydrodynamic size and Z-potential at room temperature and $_pH$=7, MNPs@SiO_2 are in water solution. It was determined that they have a hydrodynamic size between 0.8 and 1.2 µm, and a Z potential between -30 and -42 mV. The microstructure of the resulting particles was confirmed by optical microscopy and atomic force microscopy (see Figure 1). A drop of ferrofluid was dried from a microscope slide and observed using a Leica DM IL LED 1000 microscope with a Nikon D3100 camera attached (**Fig. 1a)**. Using ImageJ software, ellipses were drawn manually of 102 particles, and the mean radius of each particle was collected. Mean value and standard deviation were obtained from this set of values, in addition particle size histogram was fitted with a log-normal function **(Fig. 1b)**. A mean diameter of 1.4 µm with a standard deviation (σ) of 0.17 µm was obtained. In **Fig. 1c** is shown a typical topographic AFM image showing one silica coated microparticle and in **Fig. 1d** is shown the cross section along the line indicated in **Fig. 1c**. It can be seen that lateral dimensions are in the order of microns while the normal one is around 300 nm, indicating that the particles had obloid spheroid shapes. A closed inspection also showed that the silica coated microparticles were composed of several bare MNPs.

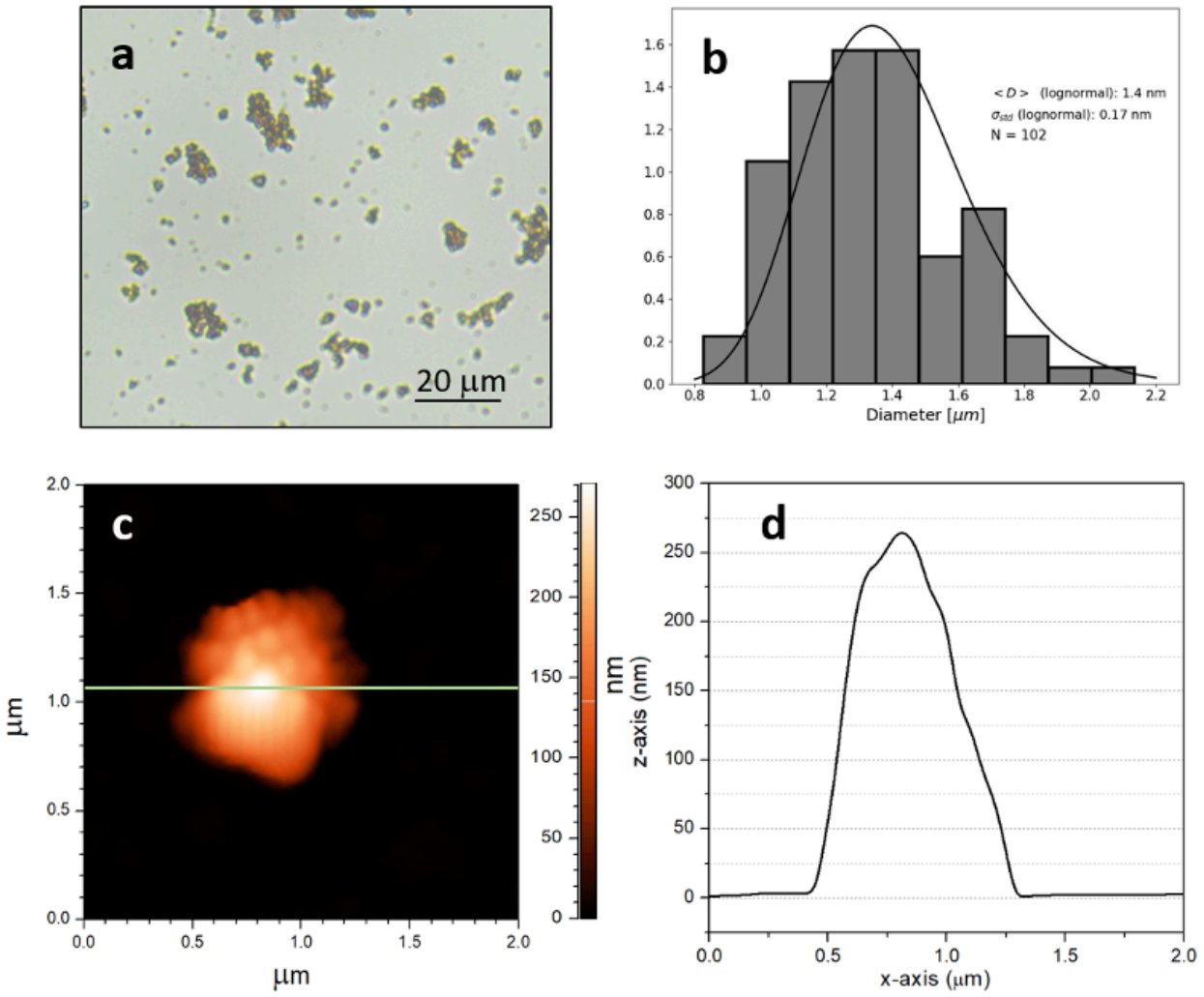

Fig. 1. a) Dried drop of particles of MNPs@SiO_2 observed using a Leica DM IL LED 1000 microscope. **b)** Particle size histogram obtained from image **a)** and the corresponding fit using a log-normal function. **c)** Typical topographic AFM image of one MNPs. **d)** Cross section along the line indicated in **c**.

To evaluate the capture efficiency of MNPs and MNPs@SiO_2 using permanent magnets we measure the force that can be exerted on them when they are exposed to a magnetic field, called magnetic force. In **Fig 2.a** is shown a schematic diagram of the arrangement used to measure magnetic force. The sample is suspended over the center of a $Nd_2Fe_{14}B$ permanent magnet resting on an analytical balance. The attraction force exerted on the magnet by the sample modifies its apparent weight. The experiment was performed using a magnet as used in magnetic racks designed for manual purification. The results are shown in **Fig 2.b.** as the vertical components of magnetic force per unit weight vs. sample-magnet distance. The gray zone represents the working zone in manual extraction experiments, showing that in this region the MNPs are subjected to forces that exceed their weight by at least one order of magnitude, thus ensuring their successful capture. **Fig 2.b.** (inset) shows a zoom corresponding to the region where the magnetic force per unit weight exceeds the unity, a distance that defines the capture region. Any MNP within 14.5 mm will be captured by the magnet allowing an efficient purification ensuring the capture of all the MNP inside the vessel. In **Fig 2.c.** two MNP solutions are shown, one as it is obtained from the synthesis and the other one exposed to a magnet. Additionally, the magnetic properties of bare MNPs and MNPs@SiO_2 samples were investigated using a Lake Shore 7400 vibrating sample magnetometer (VSM). Hysteresis loops were taken at room temperature with a maximum applied field of 1.9 T (**Fig 2.d.**). The saturation magnetization (MS) of MNPs and MNPs@SiO_2 are about 70 and 40 emu/g, respectively while the remanence and coercivity are almost zero in both cases, as expected for the single magnetic domain in the superparamagnetic regime. The nanometer size of the particles results in a single domain structure with superparamagnetic behavior. This characteristic is fundamental for two reasons: it ensures a high magnetic response to small applied fields, while in the absence of field the MNPs do not present a net magnetic moment due to thermal fluctuations avoiding their spontaneous agglomeration and its consequent decantation.

A solution with a concentration of 10 mg/mL was prepared to carry out the extraction tests.

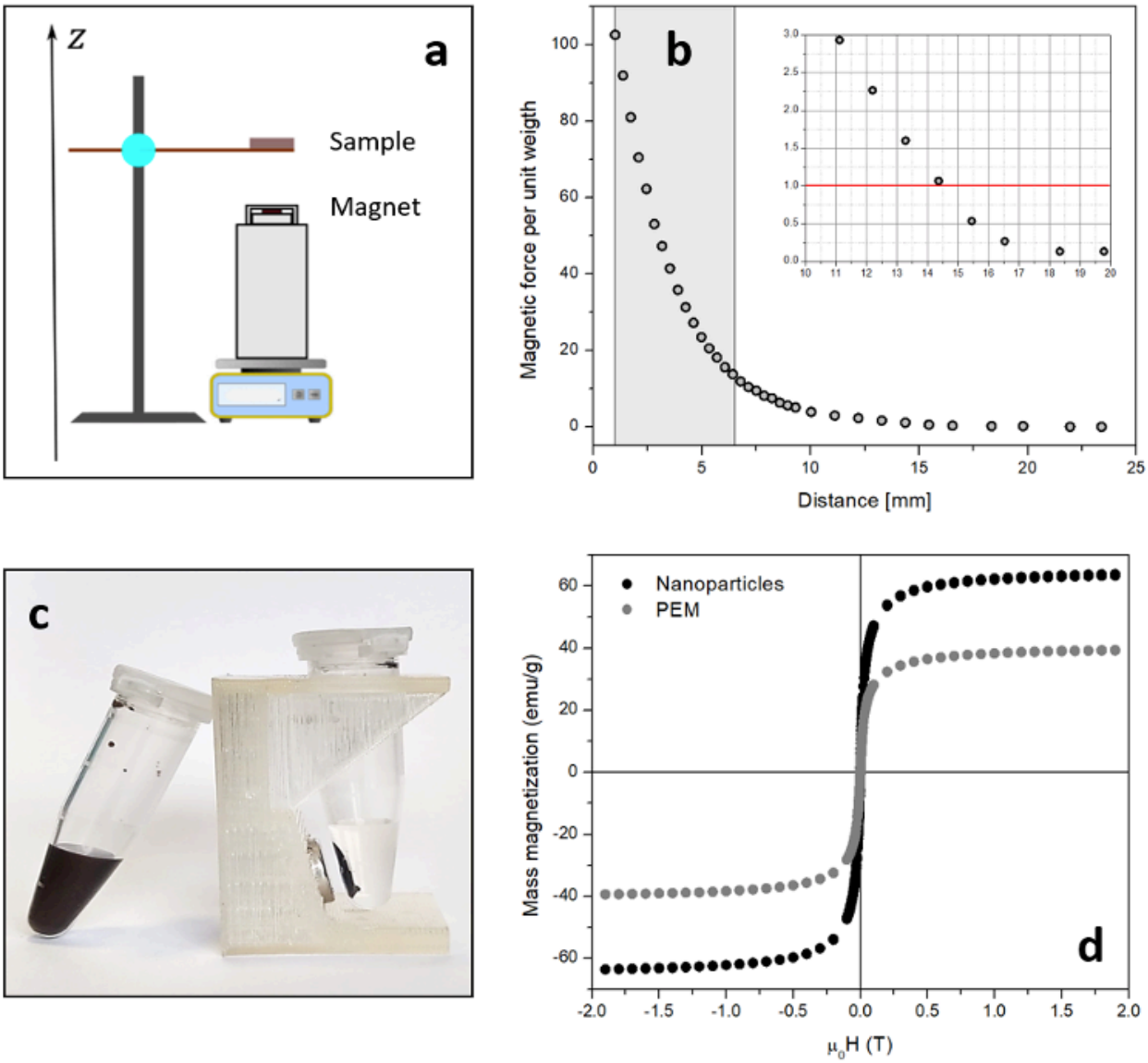

Fig. 2. a) Schematic diagram of the arrangement used to measure magnetic force. **b)** Vertical components of magnetic force per unit weight vs. sample-magnet distance. The gray zone represents the working zone in manual extraction experiments. Inset: detail of the region where the magnetic force per unit weight exceeds the unity (capture region) **c)** Two MNPs solutions, one exposed to the magnetic field generated by the home-made magnetic rack used for manual purification. **d)** Hysteresis loops at room temperature of bare nanoparticles and silica coated nanoparticles.

1.3 RNA purification

In order to assess the performance of MNP@SiO_2 for RNA extraction, we tested a protocol that, briefly, involves a step of biological sample solubilization in a lysis buffer, binding of the MNP with RNA, isopropanol and ethanol washes and resuspension of the purified RNA. Once obtained RNA, the corresponding DNase (PB-L, Productos Biologicos, Argentina) treatment was carried out to eliminate genomic DNA and the subsequent synthesis of the cDNA with the M-MLV (PB-L, Productos Biologicos, Argentina) reverse transcriptase was performed. The samples were used as a template for the detection of a housekeeping gene through the qRT-PCR technique. We assayed this protocol on different insect tissues as biological samples, derived from the insect model *Drosophila melanogaster*, the haematophagous *Rhodnius prolixus* and the phytophagous *Nezara viridula*. Firstly, we evaluate different conditions to optimize the protocol and the

quality of the RNA purified with *D. melanogaster* as biological starting material (pools of 3 insects per treatment) and specific primers for the amplification of tubulin transcript (primer sequences: 5'-TGTCGCGTGTGAAACACTTC-3´ and 5´-AGCAGGCGTTTCCAATCTG-3´). **Fig 3.a.** shows cycle threshold (Ct) values obtained with different concentrations of guanidine isothiocyanate (GITC) in the lysis buffer (2M, 4M and 6M) showing that GITC 4 M gave the better yield, with a mean in Ct value of 21.65±1.23. Also, we compare different detergent compositions in lysis buffer, i.e Triton or Sarkosyl 3% obtaining $Ct_{(Triton)}$ 32.58±1.85 vs. $Ct_{(Sarkosyl)}$ 25.84±2.32 (**Fig 3.b)**. Subsequently, we evaluated if the use of Proteinase K and Ditiotreitol (DTT) in the lysis buffer improved the yield of the purified RNA. Results showed that the addition of either proteinase K or DTT to the lysis buffer did not improve it **(Fig 3.c.).** The MNP methodology was sensitive in the detection by RT-qPCR even for small starting material, such as 0.5 *D. melanogaster*: Ct 28.13±0.68 **(Fig 3.d.)**.

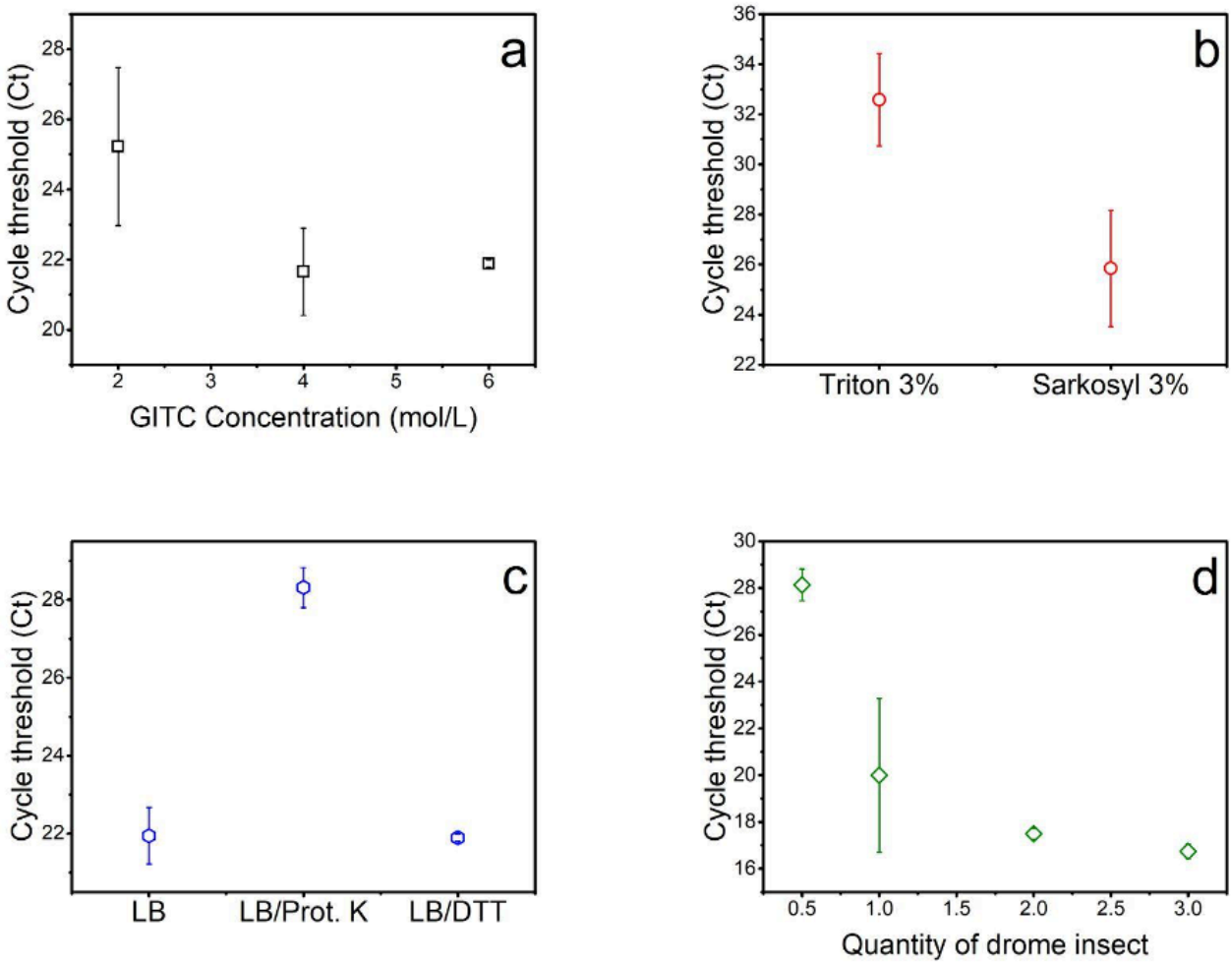

Fig. 3. Performance of MNP in RNA extraction under different conditions.

In the case of *R. prolixus* and *N. viridula*, we dissected one insect per treatment to obtain "soft tissue" (without cuticle). RNA was extracted in parallel with Trizol Reagent (Ambion, USA) following manufacturer instructions and MNP method. We included a step of centrifugation before MNP addition, in order to discard cell debrises that could interfere with the reaction. We obtained amplification of the *Rpro*β- actin gene (primer sequences: 5'-ATCTGTTGGAAGGTGGACAG-3' and 5'-CCATGTACCCAGGTATTGCT-3') and *Nvir*β- actin gene (primer sequences: 5'-CTGTACTCTCCCTCTATGCCTCC-3' and 5'-CACGTCCAGCAAGATCCAG-3') by both methods with similar Ct. As far as NPM protocols were concerned, it was useful for RNA extraction and was useful for use in qPCR detection **(Fig 4).**

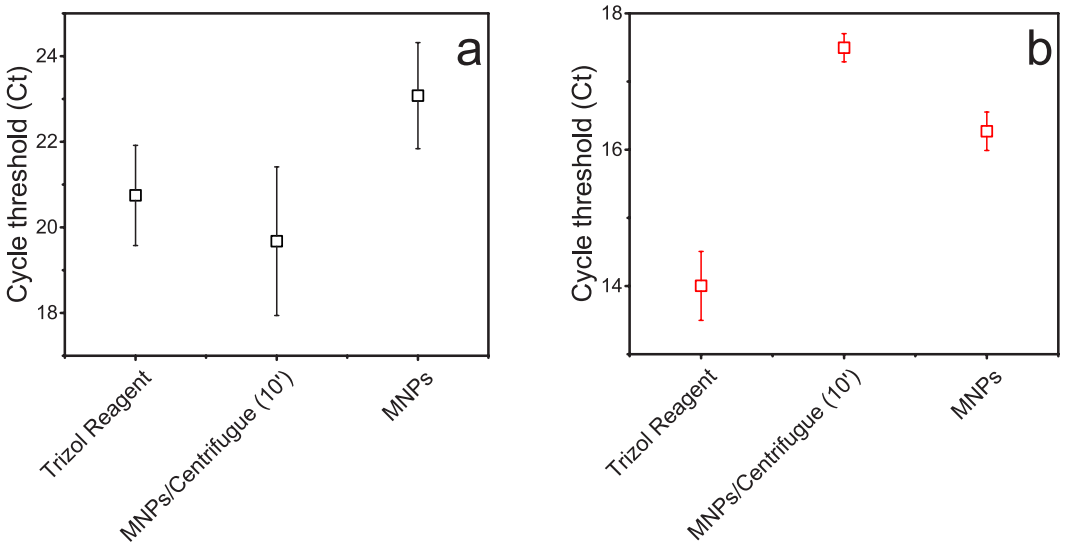

Fig. 4. Comparison of TRIzol reagent and NPM method in RNA purification of **a)** *R. prolixus* and **b)** *N. viridula* "soft tissue".

1.4 DNA purification

For DNA purification, we used a single *Ae. aegypti* mosquito for each replicate (N=3 per treatment). We compared two protocols: one of them using RNAse (DNA protocol), and the other without the use of RNAse (total nucleic acids protocol). In each of them, we also compared 2 Lysis buffer conditions: pH 6 and pH 8. Besides, we used different commercial kits, to compare yield and quality of DNA **(Fig. 5a.)**. We also performed RT-qPCR using primers that amplify on a genomic region of the voltage-gated sodium channel gene (primer sequences: 5'-CAAATTGTTTCCCACTCGCACAG-3' and 5'-AGTAAGTATTCCGTTTGGAAGTTC-3'). We observed that the MNP method, in both protocols and both pH buffer conditions, presented a better performance in terms of lower Ct values, when compared with the three commercial methods. Besides, no difference in Ct values nor DNA yield were observed among the different protocols based on MNPs (**Fig. 5**).

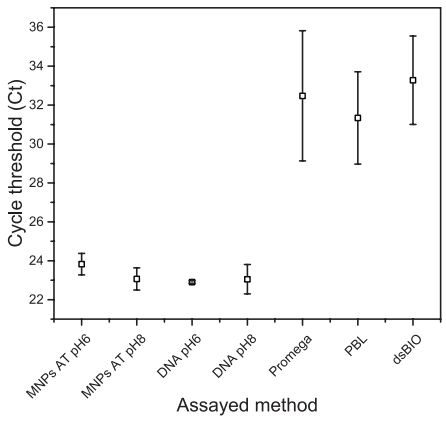

Fig. 5. Comparison of performance in RT-qPCR from different protocols to extract DNA from an *Ae. aegypti* adult mosquito. AT: protocol for total nucleic acids; DNA: protocol for DNA obtention only. Different commercial kits were used.

2. Protein purification

2.1 Synthesis of Ni^{2+} coated magnetite nanoparticles

MNPs were prepared following the synthesis route descriptive in section 1.1. For the following steps a modified route to that reported for [9] and [10] was followed. Briefly, for silica coating, MNPs were magnetically separated and washed with deionized water and dispersed in ethanol. TEOS was added dropwise to the above mentioned mixture. After magnetically stirring at room temperature for 6 h, the product ($MNP@SiO_2$) was separated and washed with a ethanol and deionized water mixture. Next, the particles were amino-functionalized dispersing $MNP@SiO_2$ in a mixture of ethanol and water (1:1) and then APTES was added slowly. The solution was heated to 60 ºC with vigorous stirring for 36 h. The final product ($MNP@SiO_2@NH_2$) was separated by magnetic decantation and washed with deionized water and ethanol. In order to coat the $MNP@SiO_2@NH_2$ with 2-amino benzamide, $MNP@SiO_2@NH_2$ were suspended in ethanol and sonicated to form a uniform dispersion. To this mixture isatoic anhydride was added and the resulting mixture was refluxed for 12 h. The prepared functionalized magnetic nanoparticles ($MNP@SiO_2@NH_2@AB$) were separated magnetically and then washed with ethanol several times to remove unreacted reactives. The last step was the immobilization of nickel. For this purpose, $MNP@SiO_2@NH_2@AB$ particles were ultrasonically dispersed in ethanol and then $NiCl_2.6H_2O$ solution was added. The mixture was refluxed for 12 h. The product ($MNP@SiO_2@NH_2@AB@Ni^{2+}$) was washed several times with ethanol and dried under vacuum.

2.2 Physicochemical characterization

In order to check the functionalization in the different steps of the synthesis we performed DLS (solution in water), XRD and FT-IR measurements. As can be seen in **Fig 6 (a)** after reaction with TEOS molecules the surface charge of magnetic $MNP@SiO_2$ nanoparticles is -7.7 ± 0.1 mV which confirms the formation of more OH groups on the surface of MNP. Subsequently, the addition of APTES changed the zeta potential to a more positive value, 3.6 ± 0.1 mV as a result of the increase of amino groups on the surface $MNP@SiO_2$. The coat with 2-amino benzamide practically does not change the surface charge of $MNP@SiO_2@NH_2@AB$, 4.7 ± 0.3 mV, in comparison to $MNP@SiO_2@NH_2$ since each 2-aminobenzamide molecule supplies one amine group. However, the immobilization of Ni^{2+} increases the zeta potential of $MNP@SiO_2@NH_2@AB$ by an order of magnitude which confers stability to the colloidal system.

The XRD patterns (**Fig. 6 (b)**) show that the crystal structure of Fe_3O_4 of bare nanoparticles is preserved for $MNP@SiO_2@NH_2$ and $MNP@SiO2@NH_2@AB@Ni^{2+}$ after surface modification with TEOS and APTES; also, good crystallinity is achieved. FT-IR spectra of $MNP@SiO_2@NH_2$ and $MNP@SiO_2@NH_2@AB@Ni^{2+}$ were shown in **Fig. 6 (c)**. The highest intense bands located around 3418 cm^{-1} and 1620 cm^{-1} were assigned to the vibration of OH groups [9]. Also, the absorption peak at 1620 cm^{-1} is overlapped with asymmetric COO– stretching and is related to the N–H bending group [11]. In addition, the band at 3428 cm^{-1} corresponds to the N–H stretching vibration of the $-NH_2$ group [12]. Furthermore, the bands at 1080 cm^{-1} and 460 cm^{-1} Si-O-Si corresponding to dissymmetric stretching vibration and the Si-O bond bending vibration [13], evidencing the formation of SiO_2 shell over Fe_3O_4 core; while the pronounced peak at 580 cm^{-1} was assigned to Fe-O bond vibration [14]. According to [15] the peak around 1536 cm^{-1} can be assigned to C-N stretching vibrations while the deformation vibration absorption peak of N-H appeared at 1558 cm^{-1} (observed like a shoulder in $MNP@SiO_2@NH_2@AB@Ni^{2+}$ spectrum). As reported by [16], the coupling of APTES group is confirmed by the stretching vibration of C–H at 2865 cm^{-1} and 2923 cm^{-1}. The above confirms the formation of APTES layer over SiO_2 cap. At last, the bands located between 1470–1570 cm^{-1} are attributed to bending motion of the N-H coupled to C-N stretching [17].

The saturation magnetization (see **Fig 6 (d)**) varies depending on the coverage of MNPs being around 60 emu/g for the final product. In all cases remanence and coercivity are almost zero, as expected for the single magnetic domain in the superparamagnetic regime.

Thermogravimetric analysis was performed in a Shimadzu TG-50H Thermogravimetric analyzer, in order to evaluate the coating formation on the surface of the MNP and their thermal stability. **Fig. 6 (e)** shows TGA curves of $MNP@SiO_2@NH_2$ and $MNP@SiO_2@NH_2@AB@Ni^{2+}$ samples. Bare Fe_3O_4 MNPs showed good thermal stability, and about 7.1% weight loss was observed, which perhaps was due to loss of physically adsorbed water molecules and surface hydroxyl

groups on the Fe_3O_4 particles (not shown here). In the case of MNP@SiO_2@NH_2 NPs (red curve), a 0.4% weight loss can be observed between 30°C and 200 °C and is due to loss of physically adsorbed water molecules on the surface, while the weight loss due to APTES coating (between 200 °C and 800 °C) was about 3.4%. TGA analysis of a sample of MNP@SiO_2@NH_2@AB@Ni^{2+} (blue curve) shows a total weight loss of 7.6% , where around 4.4% is due to 2AB coating.

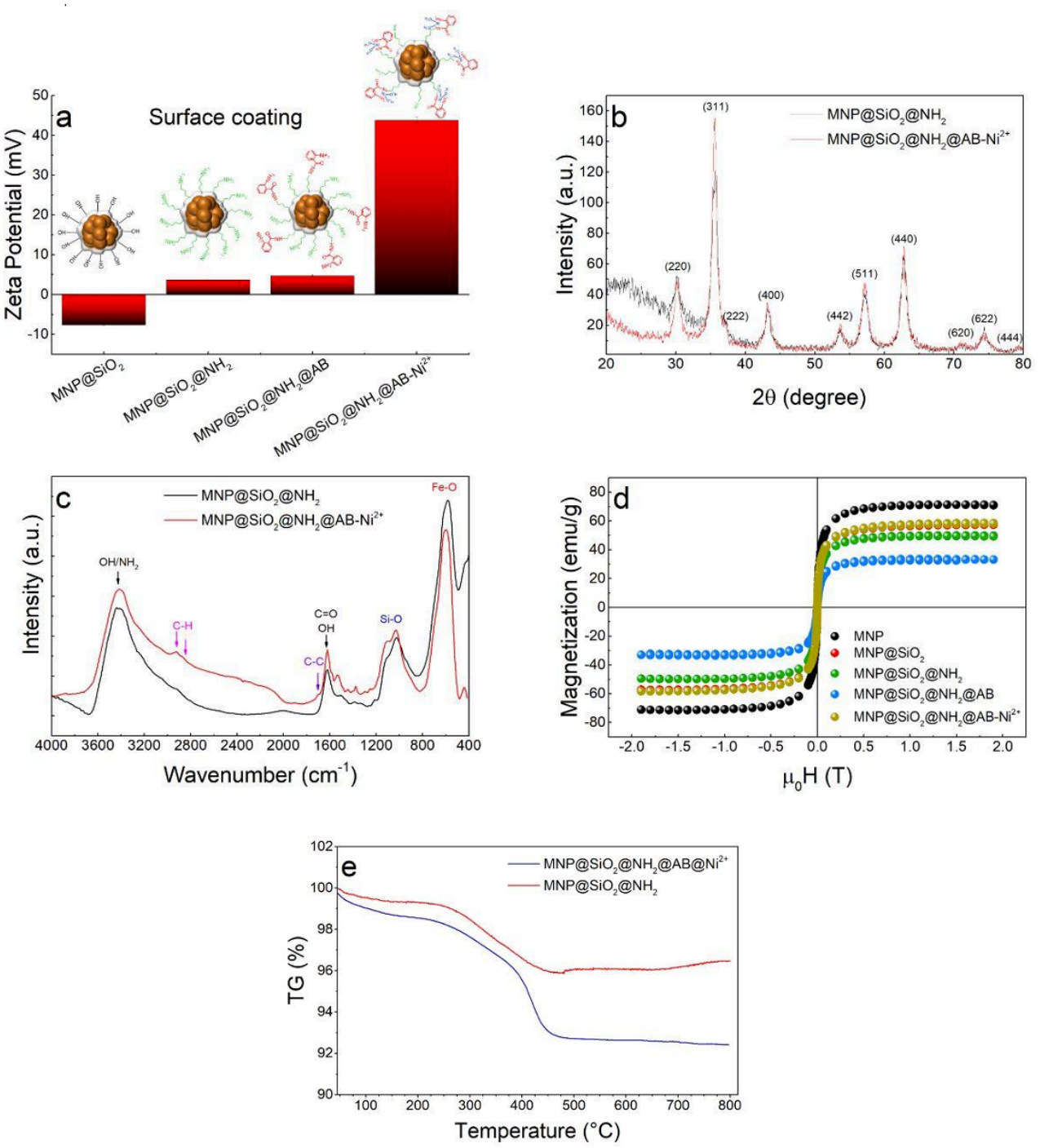

Fig. 6. a) Zeta potential and magnetization curves of microparticles in the different steps of the synthesis. **b)** and **c)** XRD patterns and FT-IR spectra of MNPs@SiO_2@NH_2 and MNPs@SiO_2@NH_2@AB–Ni^{2+}, respectively; **d)** magnetization curves of microparticles depending on the steps of the synthesis. **e)** TGA curves of MNP@SiO_2@NH_2 (red line) and MNP@SiO_2@NH_2@AB@Ni^{2+} (blue line).

The microstructure of the resulting particles were characterized by AFM and SEM measurements. **Fig. 7 (a)** shows the AFM image of a scanned area of 10x10 μm of the NP@SiO_2@NH_2@AB-Ni^{2+} sample and **Fig. 7 (b)** shows the histogram

of the sphere-equivalent particle diameter (D_s), corresponding to 141 particles manually selected in **fig 7 (a)** using the length tool of NT-MDT analysis software. The data was fitted using a log-normal function obtaining a mean value ($<D_s>$) of 272 nm and a standard deviation of 2 nm. Besides, some agglomerates can be observed too, which have a D_s around 250 nm. In **figure 7 (c)** could be observed an individual nanoparticles at lower scan scale area. **Fig. 7 (d)** shows SEM image with the topographic features of an individual nanoparticle.

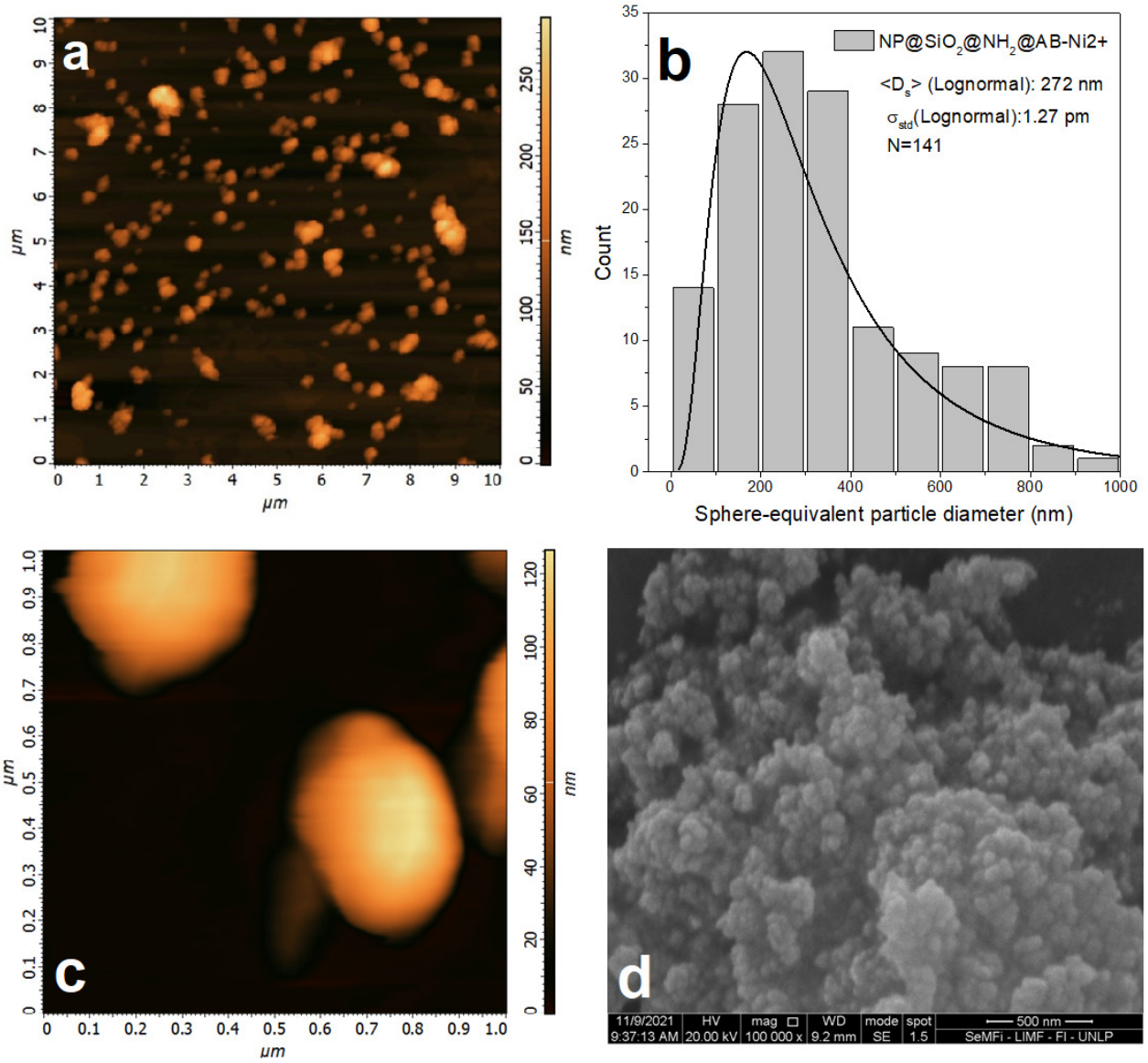

Fig. 7. Topographical analysis of MNP@SiO_2@NH_2@AB-Ni^{2+}: **(a)** AFM image of an overview (10 x 10 μm) sample area. **(b)** Sphere-equivalent particle diameter of the amount of particles observed in (a). **(c)** AFM image of an overview (1 x 1 μm) sample area. **(d)** SEM image obtained from the powder of the sample.

2.3 Protein purification

An anti-Spike-SARS-CoV nanobody derived from llama (Nb39) was expressed in *E. coli* WK6 by transformation using a Phen6 plasmid. After induction with IPTG 1 mM (DO = 0.6), culture was incubated O.N. at 28°C and then harvested by centrifugation at 350 x g for 10 minutes at room temperature. Then, pellet was resuspended in PBS 1X and disrupted using a high-pressure homogenizer Panda 2000 GEA-Niro Soavi, and the cell debris was removed by deep-filtering.

Then, Nb39 was purified using Ni Sepharose™ 6 FF, followed by size exclusion chromatography Sephacryl™ S-100 HR (SEC). Once purified the Nb39 was diluted to a concentration 1,0 mg/mL. On the other hand, MNPs were suspended by sonication in ice for 30 minutes, at 40% power in Washing Buffer (WB: TRIS 20 mM, NaCl 500 mM, Imidazole 20 mM, pH 7.5). MNPs were sonicated in WB for 30 minutes with occasional mixing. Later, 0.17 mL of Nb39 (1.0 mg/mL) were confronted with 0.33 mL of suspended MNPs at the following concentrations: 1 , 2 , 3.75 , 5 or 7.5 mg/mL.

Magnetic separations were carried out for 20 minutes using a GE rack (MagRack6). Pass-through was separated from MNP by pipetting. MNP were then washed twice for 10 minutes using 0.33 mL of WB. Then, the following elution steps were performed (Fig 8a):

1. MNPs were confronted with 85 µL Elution Buffer 1 (TRIS 20 mM, NaCl 500 mM, Imidazole 300 mM, pH 7.5; E1) for 30 minutes at room temperature. After magnetic separation, E1 was removed by pipetting and stored in a clean tube.

2. MNPs were confronted with 83 µL Elution Buffer 2 (TRIS 20 mM, NaCl 500 mM, Imidazole 1000 mM, pH 7.5; E2) for 30 minutes at room temperature. After magnetic separation, E2 was removed by pipetting and stored in a clean tube.

3. MNPs were confronted again with 83 µL Elution Buffer 2 (TRIS 20 mM, NaCl 500 mM, Imidazole 1000 mM, pH 7.5; E2) for 30 minutes at room temperature. After magnetic separation, E2 (duplicate) was removed by pipetting and stored in a clean tube.

Eluted and pass-through fractions were visualized in a polyacrylamide gel electrophoresis stained with coomassie blue (**Fig. 8 b,c**). We observed that the eluted fractions with NMPs contained a notorious amount of 15 kDa Nb39 protein, indeed the elution was better with stronger (1000mM Imidazol, Elution buffer 2) than weaker elution conditions. Also, 2 mg/mL nanoparticles were enough to remove all Nb39 from 1 mg/mL solution, as it is shown in **Fig. 8b**. On the other hand, the amount of MNPs used does not seem to influence the elution performance up to concentrations of 5mg/ml. However, we observed that with high concentrations of NMPs (7.5 mg/ml) no protein is obtained in the eluates. In this case, a high NMPs concentration could make magnetic recuperation and elution difficult. Then, the better condition was 3.75 mg/mL MNPs. These results are a first approach to generate protein purification protocols with these NMPs.

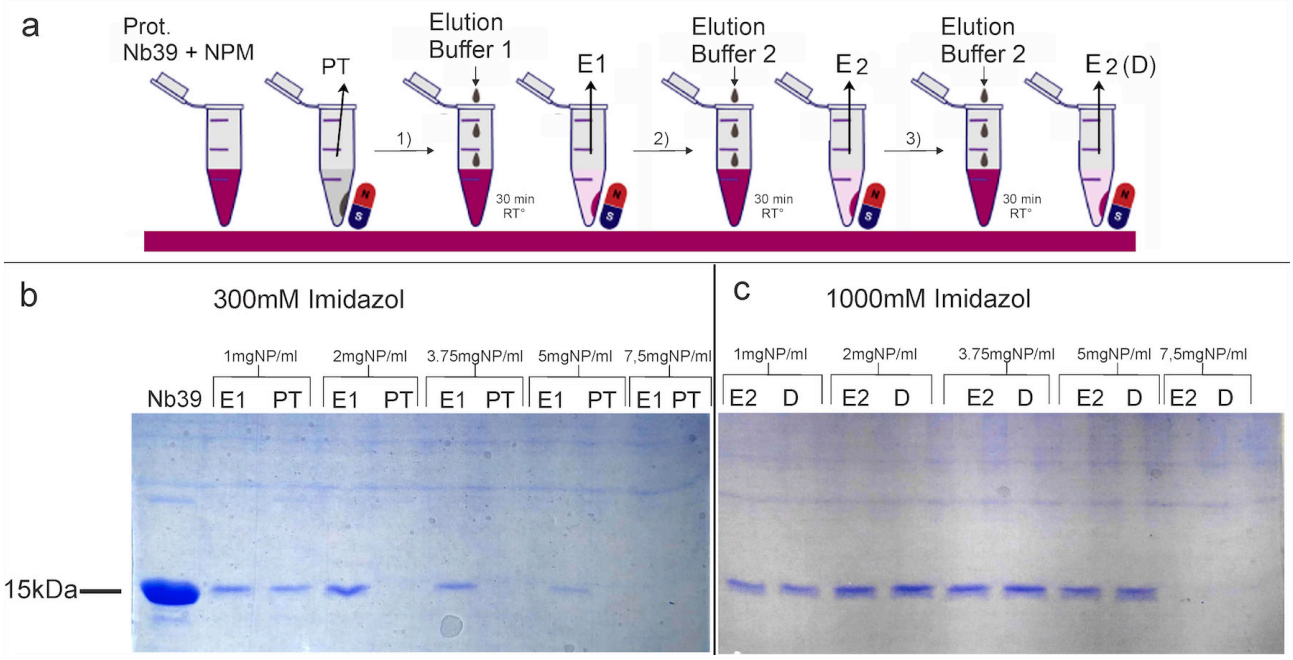

Fig. 8. a) Protein purification protocol. **b,c)** Polyacrylamide gel electrophoresis of eluted and pass-through fractions. **b)** Eluted with Elution Buffer 1, E1: elution PT: Pass-through **c)** Eluted with Elution Buffer 2, E2: elution D: duplicate. Bar size: 15 kDa.

Conclusions

Magnetic separation through nanoparticles plays a promising role in the purification and convenient, selective, and sensitive detection of biomolecules. We present results on the use of functionalized magnetic nanoparticles for the purification of nucleic acids and recombinant proteins. Silica coated magnetic particles synthesized by coprecipitation followed by hydrolysis of tetraethyl orthosilicate were tested for RNA purification on different insect tissues as biological samples, derived from the insect model *Drosophila melanogaster*, the haematophagous *Rhodnius prolixus* and the phytophagous *Nezara viridula* and also for DNA purification from a single adult mosquito of *Ae. aegypti,* vector of dengue disease. Synthesized particles are micrometric size and each microparticle was composed of several bare nanoparticles. Samples presented an appropriate magnetic response maintaining their superparamagnetism properties even after SiO_2 coating. Measurements of magnetic force per unit weight show that in the working zone in manual extraction experiments, magnetic forces exceed MNPs weight by at least one order of magnitude, thus ensuring their successful capture. The results of the purification test show that the obtained coated MNPs are efficient for RNA extraction. We evaluate different conditions of our MNPs based method in order to optimize the protocol, obtaining good qualitative and quantity of RNA. We also observed that for DNA purification, using a single *Ae. aegypti* mosquito, MNPs method using silica coated particles presented a better performance in terms of lower Ct values, when compared with the three commercial methods.

Concerning recombinant proteins purification, we test Ni^{2+} functionalized microparticles synthesized following a chemical route that include several steps in order to obtained silica coated MNPs with 2-aminobenzamide covalently immobilized on their surface to be able to form stable complexes with Ni^{2+} ions. Several experimental techniques were used to check the correct functionalization in each step. The purification assays were performed using anti-Spike-SARS-CoV nanobody derived from llama (Nb39), a 15 kDa recombinant protein expressed and purified from *E. coli* cultures. The results of the purification test show that the MNPs obtained are efficient for total protein extraction from a 1 mg/mL solution of Nb39.

ACKNOWLEDGMENTS

This work was supported with grants from CONICET, AGENCIA I+D+I, and UNLP.

References

[1] Nhiem Tran and Thomas J. Webster, Magnetic nanoparticles: biomedical applications and challenges, J. Mater. Chem., 2010, 20, 8760–8767. DOI: 10.1039/c0jm00994f

[2] Vanessa Fernandes Cardoso, António Francesko, Clarisse Ribeiro, Manuel Bañobre-López, Pedro Martins, Senentxu Lanceros-Mendez, Volume7, Issue5, (2018) 1700845

[3] Abarca-Cabrera, L., Fraga-García, P., Berensmeier, S., 2021. Bio-nano interactions: binding proteins, polysaccharides, lipids and nucleic acids onto magnetic nanoparticles. Biomater. Res. 25, 1–18. https://doi.org/10.1186/s40824-021-00212-y

[4] López-Laguna, H., Voltà-Durán, E., Parladé, E., Villaverde, A., Vázquez, E., Unzueta, U., 2021. Insights on the emerging biotechnology of histidine-rich peptides. Biotechnol. Adv. (2021) https://doi.org/10.1016/j.biotechadv.2021.107817

[5] Jiang, X., Diraviyam, T., Zhang, X., 2016. Affinity purification of egg yolk immunoglobulins (IgY) using a human mycoplasma protein. J. Chromatogr. B Anal. Technol. Biomed. Life Sci. 1012–1013, 37–41. https://doi.org/10.1016/j.jchromb.2016.01.012

[6] De Sousa, M. E., Fernandez van Raap, M. B., Rivas, P. C., Mendoza Zélis, P., Girardin, P., Pasquevich, G. A., Alessandrina, J. L., Muraca, D., & Sánchez, F. H. (2013). Stability and relaxation mechanisms of citric acid coated magnetite nanoparticles for magnetic hyperthermia. The Journal of Physical Chemistry C, 117(10), (2013) 5436-5445. DOI: 10.1021/jp311556b

[7] Oberacker, P., Stepper, P., Bond, D., Hipp, K., Hore, T. A., &Jurkowski, T. P. (2019). Simple Synthesis of Functionalized Paramagnetic Beads for Nucleic Acid Purification and Manipulation. Bio-protocol, 9(20). DOI: 10.21769/BioProtoc.3394

[8] Vogel, A. I., & Jeffery, G. H. (1989). Vogel's textbook of quantitative chemical analysis. Wiley. https://libgen.lc/

edition.php?id=136632479

[9] Rashid, Zahra and Naeimi, Hossein and Zarnani, Amir-Hassan and Nazari, Mahboobeh and Nejadmoghaddam, Mohammad-Reza and Ghahremanzadeh, Ramin, Fast and highly efficient purification of 6×histidine-tagged recombinant proteins by Ni-decorated $MnFe_2O_4$@SiO_2@NH_2@2AB as novel and efficient affinity adsorbent magnetic nanoparticles, RSC Adv., 2016,6, 36840-36848. https://doi.org/10.1039/C5RA25949E

[10] Minkner, R., Xu, J., Takemura, K., Boonyakida, J., Wätzig, H., Park, E.Y., 2020. Ni-modified magnetic nanoparticles for affinity purification of His-tagged proteins from the complex matrix of the silkworm fat body. J. Nanobiotechnology 18, (2020) 1–13. https://doi.org/10.1186/s12951-020-00715-1

[11] Rashid, Z., Naeimi, H., Zarnani, A.-H., Mohammadi, F., & Ghahremanzadeh, R. (2017). Facile fabrication of nickel immobilized on magnetic nanoparticles as an efficient affinity adsorbent for purification of his-tagged protein. Materials Science and Engineering: C, 80, 670–676. doi:10.1016/j.msec.2017.07.014

[12] Yimin, D., Danyang, L., Jiaqi, Z., Shengyun, W., & Yi, Z. (2019). Facile preparation of amidoxime-functionalized Fe_3O_4@SiO_2-g-PAMAM-AO magnetic composites for enhanced adsorption of Pb(II) and Ni(II) from aqueous solution. RSC Advances, 9(16), 9171–9179. doi:10.1039/c9ra00128j

[13] Fang, G., Chen, H., Zhang, Y., & Chen, A. (2016). Immobilization of pectinase onto Fe_3O_4@SiO_2–NH_2 and its activity and stability. International Journal of Biological Macromolecules, 88, 189–195. doi:10.1016/j.ijbiomac.2016.03.059

[14] Shahabi Nejad, M., Seyedi, N., Sheibani, H., & Behzadi, S. (2018). Synthesis and characterization of Ni(II) complex functionalized silica-based magnetic nanocatalyst and its application in C–N and C–C cross-coupling reactions. Molecular Diversity. doi:10.1007/s11030-018-9888-2

[15] Xu, J., Ju, C., Sheng, J., Wang, F., Zhang, Q., Sun, G., & Sun, M. (2013). Synthesis and Characterization of Magnetic Nanoparticles and Its Application in Lipase Immobilization. Bulletin of the Korean Chemical Society, 34(8), 2408–2412. doi:10.5012/bkcs.2013.34.8.2408

[16] Abbas, M. (2014). Fe3O4/SiO2 Core/Shell Nanocubes: Novel Coating Approach with Tunable Silica Thickness and Enhancement in Stability and Biocompatibility. Journal of Nanomedicine & Nanotechnology, 05(06). doi:10.4172/2157-7439.1000244.

[17] Hayashi, T., & Mukamel, S. (2007). Vibrational−Exciton Couplings for the Amide I, II, III, and A Modes of Peptides. The Journal of Physical Chemistry B, 111(37), 11032–11046. doi:10.1021/jp070369b

Bios

Claudia Rodríguez Torres

Bachelor of Physics from the Faculty of Exact Sciences, UNLP. PhD in Physics with a focus on Hard Ferromagnets. She conducted postdoctoral research on the topic of Recrystallization of Cold-Rolled Steels. Currently, she is a Principal Researcher at CONICET (National Scientific and Technical Research Council) and a Professor in the Department of Physics at the National University of La Plata. She is responsible for the Magnetism in Oxides (MagOx) group at the Institute of Physics La Plata and the Thin Film Growth Laboratory (IFLP). Her research area covers topics in solid-state physics, such as semiconductor physics, magnetism, and nanotechnology. Her current main focus is the exploration and design of new materials for spintronics, catalysis, and biotechnology applications. In the context of the COVID-19 pandemic, she led a research project for the development of a viral RNA extraction kit based on magnetic nanoparticles. This project led to the creation of a technology-based company called Magnolia Nanotech SA, of which she is a co-founder.

Science Reviews
from the end of the world

Vol. 2, No. 3, October 2023 // pp. 52-60 /

Nanotechnological tools for the groundwater remediation: From lab to the real environments

Verónica Lassalle

Grupo de Nanomateriales Híbridos Aplicados (NanoHiAp)
Instituto de Química del Sur(INQUISUR), Dpto. De Química, UNS.
Avda Alem 1253, Bahía Blanca, Buenos Aires, Argentina.

E-mail: velassalle@gmail.com

Abstract

The presence of nanomaterials in our everyday life has largely grown during the last years. They have emerged as relevant tools to find solutions to old problems. Among the areas where nanotechnology and nanomaterials have shown value, environmental remediation appears as an important one. The capability to tune the nanomaterial´s properties and characteristics to confer specific properties to eliminate target pollutants, accentuates the potential of these materials. The purification of water for human consumption or industrial process is currently of priority due to the increasing demand and reduction of the available water sources. This point of view article intends to show that the assays performed in the lab are not sufficient to validate large scale processes. Removal of contaminants in real aqueous environments require that due consideration is given to the behavior of the nanomaterial in field processes, because changes in efficiency and lack os stability may result in these conditions.

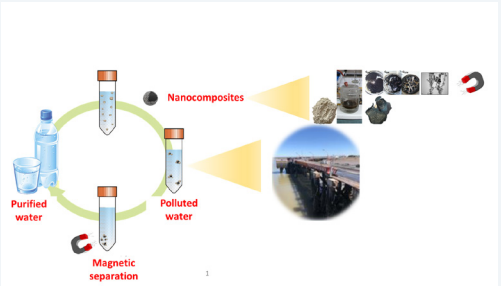

Keywords: nanocomposites, biomass, iron oxide nanoparticles, hydroxyapatite, arsenic, fluoride

Introduction

Water available for consumption is a very limited resource, essential for urban, industrial and agricultural needs. With the continuous growth of population and economic activities, the use and demand for water is increasing more and more [1]. Therefore, approximately 0.32% of the total water inventory is available for consumption, which represents 112,000 cubic kilometers, of which 90%, that is, 100,800 cubic kilometers, corresponds to groundwater. Furthermore, this amount is unevenly distributed and large regions of the world suffer from water scarcity. For the case of Argentina, see [2]. With the increasing demand for drinking water, groundwater has become the exclusive source of supply for many regions, as it is generally considered to be of better quality than surface water and is often consumed untreated as it does not contain high levels of microbial contamination. However, its quality can be affected by natural (geogenic) contaminants such as arsenic, fluoride and other metals [3].

Currently there are various designs of treatments for contaminant removal, such as electrolysis, ion exchange, chemical precipitation, membrane filtration and adsorption, the latter being one of the most effective and applicable technologies due to its efficiency, low cost and simplicity [4].

The advance of nanotechnology has open new challenges and opportunities to overcame the limitations associated to the water availability. Different kinds of nanomaterials have demonstrated to be suitable for remediation of water by

eliminating pollutant of diverse nature. Inorganic nanomaterials appear as most promising due to the properties they expose after their reduction in size; and mainly by their versatility. These nanomaterials have been widely studied as candidates to eliminate different kinds of pollutants from water by two main mechanisms: adsorption, photocatalytic degradation (or the combination of both).

The design of nanomaterials with specific properties to bind pollutants of different origin is a challenge that may derive in the generation of more efficient remediation tools.

This Point of view article deals with the analysis of literature concerning the design of novel nano-based materials to the remediation of water with special emphasis in their perspective to be effectively validated in real environments.

Nano-based materials in water remediation

Nanomaterials promoting water remediation by adsorption mechanisms

Adsorption is a process that involves the enrichment of one or more species (adsorbate), which are initially in the liquid phase, on the surface of a solid (adsorbent) forming an interfacial layer. The term desorption denotes the reverse process. This phenomenon originates from the unsaturation of the surface atoms. allowing the interaction with the molecules of the environment. Based on the forces involved in the process, it is possible to distinguish between three types of adsorption: physical, chemical and ion exchange. Physical adsorption or physisorption is the result of weak interactions between the adsorbate and adsorbent by Van der Waals forces or electrostatic interaction. Since no electrons are shared or transferred, the species retain their chemical nature, making this process totally reversible. The capture of the ions will depend largely on the surface area and the charge development in a given medium. Chemical adsorption or chemisorption is a consequence of bond formation between the species involved, leading to changes in the chemical identity of them. It is generally irreversible, and more specific than the physisorption.

Finally, ion exchange is a fast and reversible process, in which ions of the adsorbent are displaced by those of the solution [5].

The adsorbent-adsorbate interaction forces are modulated by the environment in which they are immersed, and thus the environment has a significant influence on the efficiency of the adsorption processes. The conductivity of the medium, temperature, pH, in addition to the nature of the adsorbent and the adsorbate are variables of great incidence [6].

Nanomaterials employed in water remediation that function by adsorption mechanisms have diverse structure and nature. Magnetic nanoparticles (MNPs) deserves special interest regarding their surface reactivity, easy handling and separation from the aqueous media. The selected coating of MNPs may improve their adsorptive properties conferring specificity for certain contaminants groups. Recent works deals with the use of low-cost green materials to generate a stabilization and a synergy with the magnetic phase [7].

Derivatives of minerals such as clays, or zeolites, other inorganic minerals like hydroxyapatite, and some biomass residues have been selected and tested as adsorbents of inorganic contaminants in model water samples. Figure 1 summarizes different combinations that lead to nanocomposites from magnetically responsible iron oxide nanoparticles with biomass and mineral components.

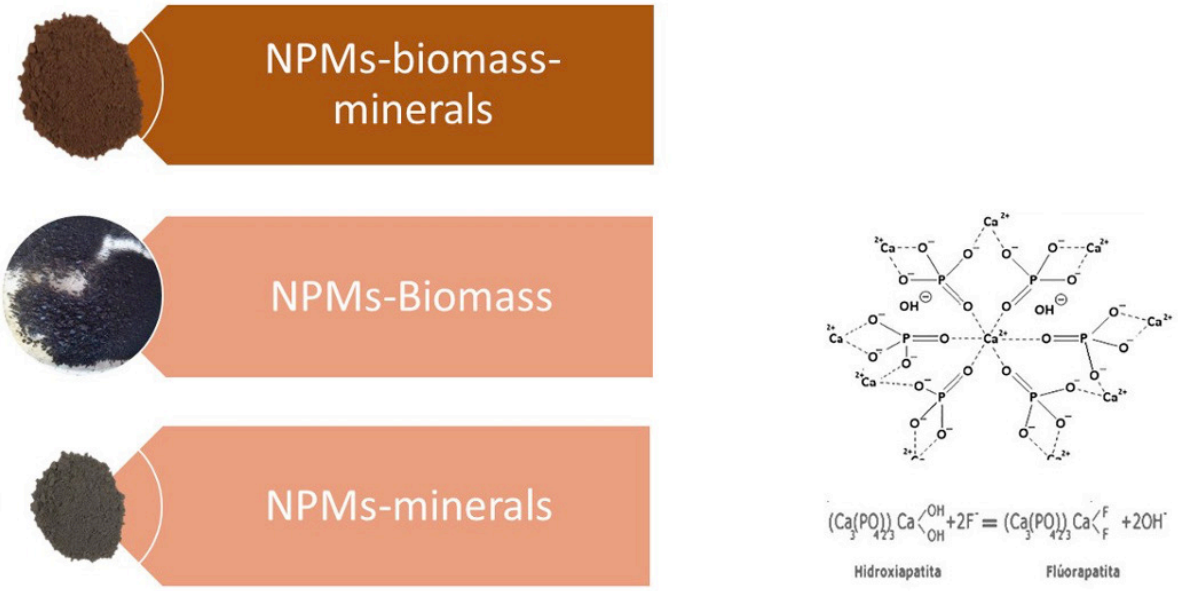

Figure 1. Schematic representation of different combinations of raw materials to obtain magnetic nanocomposites.

Studies developed in aqueous model solutions demonstrated that nanocomposites with improved capabilities may be achieved by combining the raw materials above mentioned. The functionality resulting in these nanocomposites allows the elimination of the most critical pollutants present in groundwater. Table 1 compares the performance of different nanocomposites registered in model solutions employing aqueous solution of As and F^-, as representative pollutants of groundwater matrix. The removal efficiency is expressed as mg pollutant g^{-1} adsorbent.

Table 1. Efficiency of different nanocomposites to eliminate As and F- from aqueous solutions.

Nanocomposite	As *	F-**	Reference
NPMs	0.180	ND	[8]
Zeolite	ND	ND	-
NPMs-zeolite	0.176		[8]
Hydroxyathithe	ND	12.1	[9]
Hydroxyapatite-biomass	ND	10.9	[9]

*Initial concentration: 200µg/L.
**Initial concentration: 3-80mg/L.

The initial concentrations were selected based on the content of these species in real groundwater samples. From these data it is clear that the magnetic phase is responsible for the As capture inducing mainly the formation of coordination linkages between Fe and As species. Electrostatic interactions are not favored due to the surface charge exhibiting the nanocomposites at the pH of the aqueous solution [8]. Concerning F^- removal, hydroxyapatite is the best option. The capacity of nanocomposites without HAp for fluoride removal is limited. However, zeolite-NPMs nanocomposites were satisfactory surface modified with Al and Ca moieties that generate greater affinity for F^-. However, the leaching of metallic moieties was evidenced after certain treatment time [10].

The stability of nanomaterials is not frequently tested in studies of water remediation, even though stability is a highly relevant characteristic.

Nanomaterials promoting water remediation by photocatalytic degradation and other combined mechanisms

Nanoscale semiconductors, such as TiO_2, CdS, ZnO and ZnS, have been extensively studied in photocatalysis applications from water splitting to pollutant degradation. Hence, their suitability to photodegradate organic pollutants (dyes, hydrocarbons, pharmaceuticals) in water has been extensively demonstrated by robust literature [11]. Photocatalytic degradation, one of the advanced oxidation processes (AOPs), is well known for its advantages being an energy-efficient method and relatively green procedure.

Various properties of nanosystems, such as size and morphology, strongly impact on the performance as photocatalysts. Hexagonal ZnO nanorods have a higher surface area and stability in comparison to spherical nanoparticles, leading to a more efficient photo-oxidation process [12]. For further improvement of photocatalytic activities of ZnO, metals, non-metals, and carbon materials can be deposited on ZnO to modify their optical characteristics and to improve electron-hole pair separation, which is essential for enhancing the photocatalytic process [13]. Studies have shown that the overall photocatalytic efficiency can be improved by depositing platinum to reduce electron-hole pair recombination and enhance visible light absorption. [14,15].

The application of these nanomaterials for the remediation of groundwater deals, mainly, with the elimination of organic matter affecting the conditions of water for human consumption. In this regard, the efficiency of ZnO, TiO_2 in the nanosize have been demonstrated against organic pollutants as dyes, aromatic polycyclic compounds and other; as well as against different types of bacteria [16,17].

However, the information concerning semiconductors based nanomaterials to eliminate inorganic species affecting the water quality is restricted. For instance, few articles deal with the use of ZnO-TiO_2 nanomaterials for the elimination of nutrients (mainly N and P species) from water. It is worth mention that nutrients involving N species such as nitrites, nitrates, ammonium; as well as phosphates species cause serious damages related to the eutrophication of water sources [18]. Own studies were developed by combining experimental assays and DFT theoretical calculations, demonstrating satisfactory yields in the removal of ammonium from water samples employing ZnO nanoparticles. The achieved findings revealed that non-electrostatic interactions took place but instead of that hydrogen and coordination bonds were the preferential interactions between ZnO NPs and ammonium. These data further indicated other abilities, besides photocatalytic degradation, of semiconductor nanomaterials to function as water remediators.

According to the reported information, it is noted that some inorganic pollutants such as heavy metals can be found in groundwater environments combined with other organic pollutants such as the polycyclic aromatic hydrocarbons (PAHs), pesticides, etc. In such cases, simultaneous removal mechanisms have been reported by means of semiconductor based nanomaterials. One of them is related to the preparation of phenanthroline/TiO_2 nanocomposites rich in oxygen vacancy defects exhibiting multiple functions as pollutant detection, adsorption, and degradation [19].

Other researches deal with the removal of heavy metals from aqueous effluents, which may also be present in combination with some organic compounds. In this case, semiconductors nanomaterials may be used for removal by advanced oxidation processes. In a second step, the ionic reduction of heavy metals can be induced by photocatalysis, typical of metal oxides such as TiO_2, ZnO, ZrO, Fe_3O_4, etc. [20]. These materials function as heterogeneous photocatalysts having a relatively narrow band gap width between the conduction band (CB) and the valence band (VB), in the presence of light of the appropriate wavelength (usually <370 nm) the photons are absorbed by the oxide, exciting the electrons to CB an crating a hole in VB. The existence of the electron-hole (e^-/h^+) pair enables redox-type reactions [21]. As mentioned, in water OH and superoxide radicals are formed. These last are responsible for the reduction of heavy metals to lower oxidation states which, in some cases, are less toxic for the environment; such is the case of Cr(VI) to Cr(III) [22,23]. In fact, it has been shown that the reduction of heavy metal ions is more effective when it is carried out simultaneously with the removal of organic contaminants [24,25].

These results may substantiate the use of semiconductors nanomaterials (mainly ZnO and TiO_2) for the remediation of groundwater in rural environments where sewerage is precarious or almost inexistent.

Effect of water matrix in the efficiency of nanomaterials in water remediation

Removal of pollutants from aqueous sources depends crucially on experimental conditions that have to be necessarily taken into account. For instance, in the case of adsorption mediated pollutant´s elimination, the adsorption time affects the process in different ways depending on the adsorbate particle size, the amount of active preferential sites on the surface, as well as changes in the chemical composition on the surface of the adsorbent material [26]. The pH plays a key role in the adsorption of ionic species, as it modifies the rate of the process as well as it can induce changes in the active sites

of the adsorbent, modifying the selectivity against different adsorbates. [27]. Temperature is another important variable, in the case of adsorption mechanism. If the adsorption process is exothermic the adsorption efficiency will be lower as temperature increase, due to a decrease in the intensity of attractive forces between surface-active sites and adsorbate particles [28].

In general, after a survey of the current literature, one can find that most of the studies tending to provide insights regarding the strategies, mechanisms, etc. to water remediation are carried out under ideal conditions of pH, conductivity, temperature; even more normally, pollutant´s concentrations employed for these assays are not in line with those found in real environments. Therefore, model studies, as are normally defined, exhibit moderated utility when the aim is finding concrete solutions to a real problem.

Simulated water samples

A recommended practice is to use in the laboratory water samples replicating the conditions found in the aqueous environment to be remediated. For instance, magnetic nanoparticles (MNPs), based on iron oxide (magnetite) and ferrogel of gelatin and MNPs, were employed to remove heavy metals and nutrients from water samples. In a first step, an exhaustive adsorption study was conducted in batch using model solutions aiming to adjust the adsorption conditions, exploring the capability of these nanomaterials to remove Cu, NO_3^-, and NO_2. Adsorption studies using water simulating the real samples were also performed. In this case the simulated samples were prepared in laboratory by adjusting the conditions and composition in order to replicate an aqueous sample from the Bahía Blanca estuary. The components were ionic salts such as $NaNO_3$, $CaCl_2.2H_2O$, $MgSO_4.7H_2O$ Na_2CO_3, K_2HPO_4, $FeCl_3$, $CuSO_4.5H_2O$, $ZnSO_4.7H_2O$. The solution was adjusted to pH around 6.44 and conductivity of 4.98 mS. Both nanomaterials, MNPs and ferrogels, demonstrated an efficiency between 60 and 80% for the removal of heavy metals and 85% for NO_3^- and NO_2. [29]

In another study marine water was also simulated aiming to determine the ability of microplastics to accumulate heavy metals. In this case replicated marine-water was obtained from the commercially available “Marinium” that was diluted in distilled water by magnetic stirring [30]. The composition was mainly given by Na, Mg, Ca, Sr and K chlorides, bromides, sulfates and fluorides; to this milieu known concentrations of heavy metals were added [31].

The simulation of effluents from an urban discharge plant was also done, by the enrichment of aqueous samples with nutrients species such as ammonium and phosphates. Concentrations around 40-100 mg L^{-1} of NH^{4+} were employed adjusting the pH between 8-9 [32].

Substantial changes in nanomaterials stability can occur under simulated conditions. Therefore, it stability must be evaluated in experiments simulating the aqueous media, measuring also the possible leaching of nanomaterial´s components. Figure 2 depicts the sequential steps that should be followed in trying to close the lab investigation to real application in the water remediation field.

Figure 2. Representation of the steps involving in the validation of (nano)materials for water remediation.

Real water samples

The validation of novel technologies developed in the laboratory may be achieved by studying the behavior of such (nano)materials in the real environments where they will be employed. As it was earlier mentioned, significant surface modifications can occur leading to differences in the expected efficiency of those materials.

Even though the focus of this contribution is on the groundwater, it is useful to show the incidence of different media of nanomaterials. Table 2 summarizes data on pollutant removal by adsorption from marine, surface and ground water. Different kinds of pollutants are found depending on the type of water; hence diverse interaction involving in different elimination mechanism can occur.

Table 2. Efficiency of different nanomaterials in real water remediation ny adsorption

Water source	Nanomaterial	Pollutant	Efficiency (% of pollutant removal)	Reference
Groundwater	Nanocomposites zeolite-iron oxide	As	94	[8]
Groundwater*	Nanocomposites zeolite-iron oxide	As	61	[8]
Groundwater	Nanocomposites hydroxyapatite-magnetite	F-	56	[33]
Marine water	Gum Arabic co- ated iron oxide nanoparticles	NO_3^-, NO_2^- Pb_2+	29 44 36	[29]
Marine water	Ferrogels	NO_2^- Pb_2^+	56 47	[29]
Groundwater	Hydroxiapatite-biomass nanocomposites	F-	77	[9]
Surface water**	Iron oxide biomass Nanocomposites	As Ca^{2+} Na^+	81 14 9.2	[34]
Surface water***	Iron oxide biomass Nanocomposites	As Ca^{2+} NO_2- and NO_3^-	73 29 82	[34]

*Continuous remediation process
** Water samples collected in Sauce Grande river
***Water samples from El Divisorio brook

Another point deserves attention is the design of the experiments able to reliably represent the remediation process in a domestic, industrial or rural environment. It is important to highlight that the information listed in Table 2 mostly refers to batch assays where the nanomaterial was incubated with the real water sample by the ´preset time according to previous basic or simulated assays. Any modification in the remediation process, which can be required in each specific case, necessary leads to differences in the pollutant removal efficiency. This issue is reflected in the data included in the Table as *. In such case the assays performed in entry 1 were replicated by employing a lab-made flux system, as shown in Figure 3, where the water sample is pumped in a continuous flux to a vessel containing packed adsorbent nanomaterial.

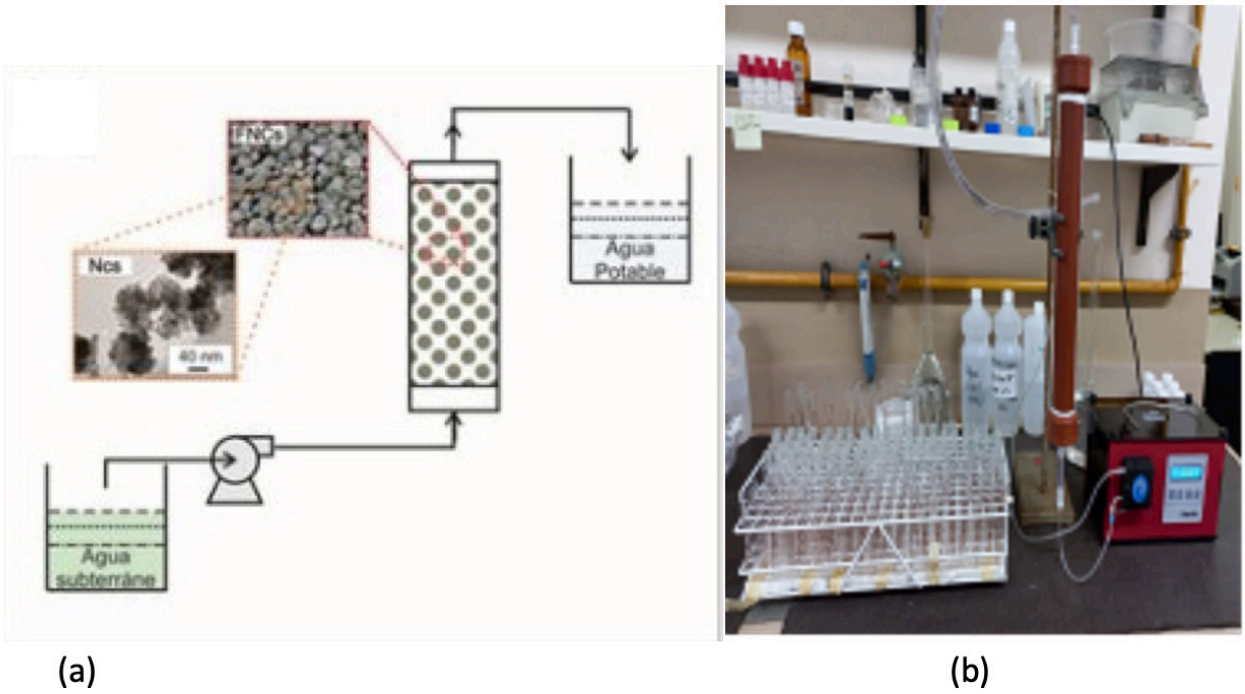

Figure 3. a. Schematic representation of a continuous in flux system to remediate groundwater; b. Photograph of a lab-made continuous system.

Special attention is further required to check the stability of the nanomaterial in continuous systems. The decay of the efficiency is not the only issue that has to be careful considered, but also the possibility of leaching of components of the nanomaterials. Continuos reutilization of the nanomaterial requires that enough information has to exist in order to predict the number of reutilization cycles or the volume of fresh water that the system will be able to remediate.

Concluding remarks

This point of view article aimed to concretely show the impact of nanomaterials in the water purification area. Even when the literature is abundant, this article focuses on the precautions required to translate the experiments in the lab to field processes. The knowledge of the relationship between nanomaterial´s properties and remediation mechanisms is mandatory and data concerning the stability of the nanomaterials in the media where they will be employed are also required. The need to analyze the behavior of nanomaterials in media and conditions where they actually will be employed appears as a key issue. Therefore, a sequence of basic assays using model aqueous solutions, followed by assays in simulated water should be suitable to lastly develop remediation assays in real water samples. Finally, the need to a multidisciplinary focus is highlighted in relation to the design of a suitable and efficient process which will be specific for the water source, and most important, for the site where the remediation will be implemented.

References

[1] X. Lu, L. Liu, R. Liu, and J. Chen, “Textile wastewater reuse as an alternative water source for dyeing and finishing processes: A case study,” Desalination, vol. 258, no. 1–3, pp. 229–232, 2010.

[2] M.H. Badii; J. Landeros; E. Cerna, “El recurso de agua y sustentabilidad,” Rev. Daena (International J. Good Conscienc., vol. 3, no. 1, pp. 661–671, 2008.

[3] A. Bretzler and C. A. Johnson, “The Geogenic Contamination Handbook: Addressing arsenic and fluoride in drinking water,” Appl. Geochemistry, vol. 63, pp. 642–646, 2015.

[4] L. Chen, K. S. Zhang, J. Y. He, W. H. Xu, X. J. Huang, and J. H. Liu, “Enhanced fluoride removal from water by sulfate-doped hydroxyapatite hierarchical hollow microspheres,” Chem. Eng. J., vol. 285, pp. 616–624, 2016.

[5] Tejada Tovar, C., Villabona Ortiz, Á. & Ruiz Rangel, V. Biomasa residual para remoción de mercurio y cadmio: una revisión. *Ingenium* 6, 11–21 (2012).

[6] García Asenjo, N. Una nueva generación de carbones activados de altas prestaciones para aplicaciones medioambientales. 217 (2014).

[7] M.F Horst, V.L.Lassalle, M.L Ferreira,Review: Nanosized magnetite in low cost materials for environmental remediation of wastewater polluted with toxic metals, azo- and antraquinonic dyes", Frontiers of Environmental Science and Engineering. October 2015, Volume 9, Issue 5, pp 746-769 .

[8] V.N. Scheverin, M. Grünhut, M.F. Horst, S. Jacobo and V.L. Lassalle, Novel iron-based nanocomposites for arsenic removal in groundwater: A real case study, Environmental Earth Sciences, 2022 v.81 no.7, 188 https://doi.org/10.1007/s12665-022-10286-z.

[9] V.N. Scheverin, M.F. Horst and V.L. Lassalle Novel Hydroxyapatite-biomass nanocomposites for fluoride adsorption, Results in Engineering, 16 (2022) 100648.

[10] Verónica N. Scheverin, Analía V. Russo, María F. Horst, Silvia Jacobo, Verónica L. Lassalle Design of magnetic nanotechnological devices for the removal of fluoride from groundwater,Cleaner Engineering and Technology, 3, 100097 (2021) doi.org/10.1016/j.clet.2021.100097.

[11] Kezhen Qi, Bei Cheng, Jiaguo Yu, Wingkei HoReview on the improvement of the photocatalytic and antibacterial activities of ZnO Journal of Alloys and CompoundsVolume 727, 15 December 2017, 792-820

[12] Tofa, T.S.; Kunjali, K.L.; Paul, S.; Dutta, J. Visible light photocatalytic degradation of microplastic residues with zinc oxide nanorods. Environ. Chem. Lett. 2019.

[13] Bora, T.; Dutta, J. Plasmonic photocatalyst design: Metal-semiconductor junction a_ecting photocatalytice_ciency. J. Nanosci. Nanotechnol. 2019, 19, 383–388.].

[14] Lin, J.M.; Lin, H.Y.; Cheng, C.L.; Chen, Y.F. Giant enhancement of bandgap emission of ZnO nanorods byplatinum nanoparticles. Nanotechnology 2006, 17, 4391–4394;

[15] Wang, P.; Huang, B.; Dai, Y.; Whangbo, M.H. Plasmonic photocatalysts: Harvesting visible light with noble metal nanoparticles. Phys. Chem. Chem. Phys. 2012, 14, 9813–9825

[16] María Belén Perez Adassus, C.V. Spetter and V.L. Lassalle, Biofabrication of ZnO nanoparticles from Sarcocornia ambigua as novel natural source: A comparative analysis regarding traditional chemical preparation and insights on their photocatalytic activity , Journal of Molecular Structure, 1256 (2022) 132460 https://doi.org/10.1016/j.molstruc.2022.132460

[17] T. O. Ajiboye, O. A. Oyewo, and D. C. Onwudiwe, "Simultaneousremoval of organics and heavy metals from industrialwastewater: a review," Chemosphere, vol. 262, article128379, 2021.

[18] Xiaojing Zhang, Nan Zhang, Haoqiang Fu, Tao Chen, Sa Liu, Shuhua Zheng, Jie Zhang,Effect of zinc oxide nanoparticles on nitrogen removal, microbial activity and microbial community of CANON process in a membrane bioreactor,Bioresource Technology,Volume 243,2017,Pages 93-99,ISSN 0960-8524,https://doi.org/10.1016/j.biortech.2017.06.052.

[19] P. Chen, H. Zheng, H. Jiang et al., "Oxygen-vacancy-richphenanthroline/TiO2 nanocomposites: an integrated adsorption,detection and photocatalytic material for complex pollutantsremediation," Chinese Chemical Letters, vol. 33,no. 2, pp. 907–911, 2022.

[20] T. Naseem and T. Durrani, "The role of some important metal oxide nanoparticles for wastewater and antibacterial applications: a review," Environmental Chemistry and Ecotoxicology,vol. 3, pp. 59–75, 2021.

[21] X. Kang, S. Liu, Z. Dai, Y. He, X. Song, and Z. Tan, "Titanium dioxide: from engineering to applications," Catalysts, vol. 9,no. 2, p. 191, 2019.

[22] Z. Zhao, H. An, J. Lin et al., "Progress on the photocatalyticreduction removal of chromium contamination," The Chemical Record, vol. 19, no. 5, pp. 873–882, 2019.

[23] V. Dhiman and N. Kondal, "ZnO Nanoadsorbents: a potentmaterial for removal of heavy metal ions from wastewater,"Colloid and Interface Science Communications, vol. 41, article100380, 2021.

[24] T. O. Ajiboye, O. A. Oyewo, and D. C. Onwudiwe, "Simultaneousremoval of organics and heavy metals from industrialwastewater: a review," Chemosphere, vol. 262, article128379, 2021.

[25] L. Liu, R. Li, Y. Liu, and J. Zhang, "Simultaneous degradationof ofloxacin and recovery of Cu(II) by photoelectrocatalysiswith highly ordered TiO2 nanotubes," Journal of Hazardous Materials, vol. 308, pp. 264–275, 2016.

[26] F. Cherono, N. Mburu, and B. Kakoi, "Adsorption of lead,copper and zinc in a multi-metal aqueous solution by wasterubber tires for the design of single batch adsorber," Heliyon,vol. 7, no. 11, article e08254, 2021.

[27] M. Sharma, D. Choudhury, S. Hazra, and S. Basu, "Effectiveremoval of metal ions from aqueous solution by mesoporousMnO2 and TiO2 monoliths: kinetic and equilibrium modelling,"Journal of Alloys and Compounds, vol. 720, pp. 221–229, 2017.

[28] Ş. Taşar, F. Kaya, and A. Özer, "Biosorption of lead(II)ions from aqueous solution by peanut shells: equilibrium,thermodynamic and kinetic studies," Journal of EnvironmentalChemical Engineering, vol. 2, no. 2, pp. 1018–1026, 2014.

[29] Maria Fernanda Horst, Aldana Pizzano, Carla Spetter and Verónica Lassalle, Magnetic nanotechnological devices as efficient tools to improve the quality of water: analysis on a real case, Environ Sci Pollut Res (2018) 25, pages 28185–28194. https://doi.org/10.1007/s11356-018-2847-8.

[30] López Greco, L.S., Sánchez, V., Nicoloso, G.L., Medesani, D.A., Rodríguez, E.M., (2001). Toxicity of cadmium and copper on larval and juvenile stages of the estuarine crab Chasmagnathus granulata (Decapoda, Grapsidae). Archieves of Environmental Contamination & Toxicology 41, 333–338.

[31] Tesina de Licenciatura en Ciencias Ambientales, Mateo Fabiani, Dpto. de Qca. UNS, mayo 2021.

[32] M.S. Dantas, L.F. de Morais Silva, H.H. Utida Novaes, and S.C. Oliveira: *Water Sci. Technol.*, 2022, vol. 85, pp. 3479–92.

[33] Tesina de Licenciatura en Química, Lucía Schmidt, Dpto. de Qca., UNS.

[34] Verónica Natalia Scheverin, Elisa Mariel Diaz, Ana María Martínez, Verónica Lassalle and María Fernanda Horst, Impacto del uso de materiales compuestos sobre la remediación de As y otros contaminantes del Río Sauce Grande y Arroyo El Divisorio, , Jornadas de Aguas del Sudoeste bonaerense (JASOB), 2019.

Bio

Verónica Lassalle

She's a researcher in the area of chemistry of materials, orienting her work to the design of nanomaterials with specific properties to be applied in the biomedical and environmental remediation fields. She received her PhD in Chemistry from National University of South in 2006, performing her studies in PLAPIQUI (UNS-CONICET), Bahía Blanca. After her postdoctoral studies, she moved to INQUISUR(UNS-CONICET, Bahía Blanca) as CONICET Assistant researcher. Currently she is the head of the Applied Hybrid Nanomaterials (NanoHiAp) group and is Associated Professor of Department of Chemistry in UNS.

Science Reviews
from the end of the world

Vol. 2, No. 3, October 2023 // pp. 61-69 /

Synthesis, characterization and application of a mesoporous nanomaterial integrated in a bioanalytical microsensor with electrochemical detection for the determination of mycotoxin T2 in samples of agri-food interest

Alex Simioli[a,*], Jhonny Villarroel Rocha[b], Martin Fernandez Baldo[c]

[a]*Laboratory of Environmental Measurements, Institute of Chemical Technology (INTEQUI), National University of San Luis, Av. Ejército de los Andes 950, San Luis, 5700, Argentina.*
[b]*Laboratory of Porous Solids (LabSoP), INFAP-CONICET, National University of San Luis, Av. Ejército de los Andes 950, San Luis, 5700, Argentina.*
[c]*INQUISAL. Chemistry Department. National University of San Luis, CONICET. San Luis, Argentina.*

** Corresponding author. E-mail: alexsimioli@hotmail.com*

Abstract

An ordered mesoporous material (OMM) type SBA-16 was synthesized from sol gel type reactions and the self-assembly of surfactants. Once SBA-16 was obtained, it was functionalized with APTES (3-aminopropyltriethoxysilane) on the one hand and with MEA (monoethanolamine) on the other. Subsequently, the characterization of these nanomaterials was carried out using Scanning Electron Microscopy (SEM), Energy Disperse Spectroscopy (EDS), Infrared Spectroscopy (FTIR), N2 adsorption-desorption and X-ray Diffraction (XRD). In addition, a biosensor was developed where the central channel was modified with the material obtained SBA-16 (MEA) and a commercial ELISA Kit (enzymatic immunoassay) was used for a quantitative determination of the mycotoxin T-2 and compared with the analytical results of our generated biosensor.

Keywords: nanomaterial, biosensor, agroalimentario, contaminación, toxina T2

Introduction

In recent years, conventional analytical techniques have experienced a marked trend towards miniaturization [1]. The development of bioanalytical sensors since its inception has been focused primarily on the environmental, chemical, biochemical, pharmaceutical, agri-food fields, among others, because their use entails innumerable advantages such as: high sensitivity, selectivity, reproducibility, low cost for small volumes of sample and reagents required, short analysis times and, fundamentally, the detection limit can be reduced by modifying the sensor electrode with silica nanomaterials as a platform in order to amplify the analytical signal, this being a possible innovation in the development of sensors endowed with a larger effective electrochemical area. With which in the present work a new specific, sensitive and fast analytical methodology is proposed, which through the use of nanomaterials in bioanalytical sensors, allow the quantitative evaluation of an analyte of agri-food interest such as mycotoxin T2, which as a contaminant It produces serious complications for human health [2-4].

Materials and methods

The SBA-16 material was synthesized from the sol-gel process [5], once obtained we functionalized it with APTES (3-aminopropyltriethoxysilane) and MEA (monoethanolamine).

Functionalization of the SBA16 with APTES

The functionalization of the MMO SBA-16 with APTES (3-aminopropyltriethoxylan) is carried out by reflux where the SBA-16 obtained is dried for 24hs at 80°C, later we add 1g of SBA-16, 1ml of APTES, 100ml in a round bottom flask of toluene we leave it for 24hs under agitation at 90°C. After 24hs, the supernatant solid is washed with toluene and then dried for 24hs at 80°C in an oven.

Functionalization of the SBA16 with MEA

This functionalization process is carried out in a 50ml beaker where we add 10ml of methanol, 0.42ml of MEA (monoethanolamine), mix for 0.5h, then deposit 1g of SBA16 in the solution, mix for 60min, the solid obtained is washed with methanol and dried for 24hs in the oven at 80°C.

Characterization of the materials obtained

Scanning Electron Microscopy (SEM)

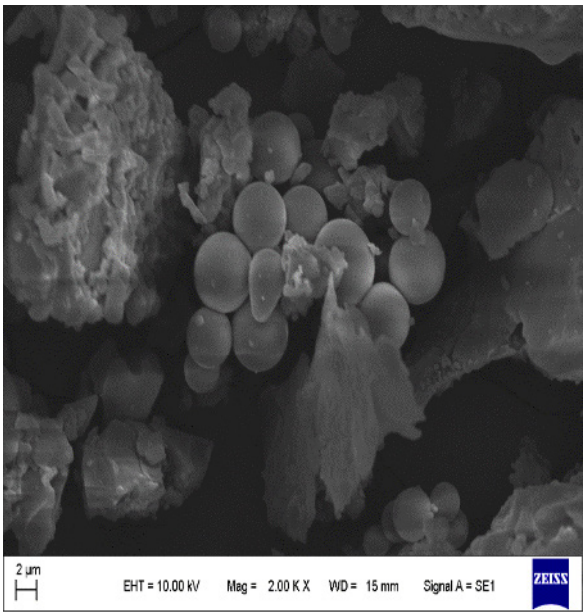

Figure 1. SEM micrographs of SBA-16 materials

In the figure we can see the SEM micrographs of the mesoporous silica SBA-16 where it can be seen that the particles of said material have spherical shapes of very uniform size and the rest of the material that does not have a spherical shape is part of the material that was not functionalized [7].

Energy Dispersive Spectroscopy (EDS)

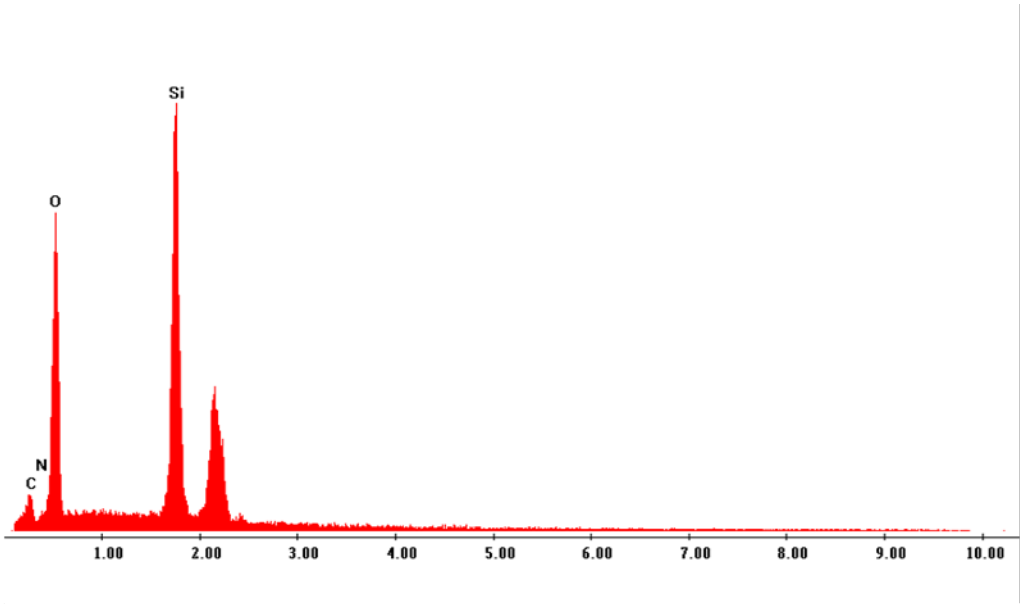

Figure 2. Chemical analysis by EDS of the material SBA-16

Figure 2 shows the spectrum of microanalysis carried out on the functionalized and impregnated SBA-16 material. As you can see, there is the presence of the chemical elements that are silicon and oxygen indicating that this material is SiO_2.

Adsorption-desorption of N_2 at 77K

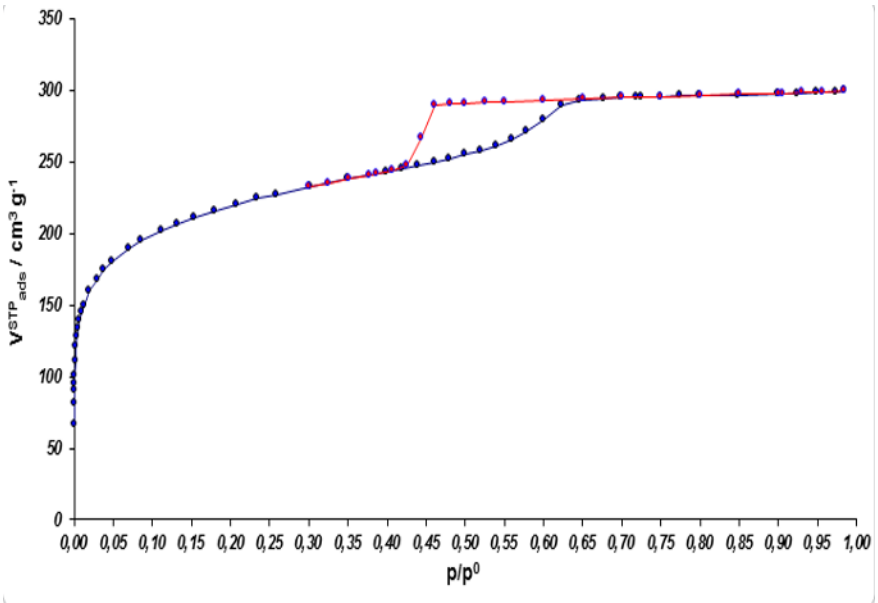

Figure 3. Isoterma de adsorción-desorción de N_2 de la SBA-16

Figure 3 shows the experimental N_2 adsorption-desorption isotherm at 77 K of the SBA-16 material under study. A type IV isotherm is observed, indicating that it is a mesoporous material. In addition, the presence of an H2 type hysteresis loop can be observed, indicating that this material presents an important degree of ordering of its pores, which are characteristic of this type of material [8].

Pore size distribution (PSD)

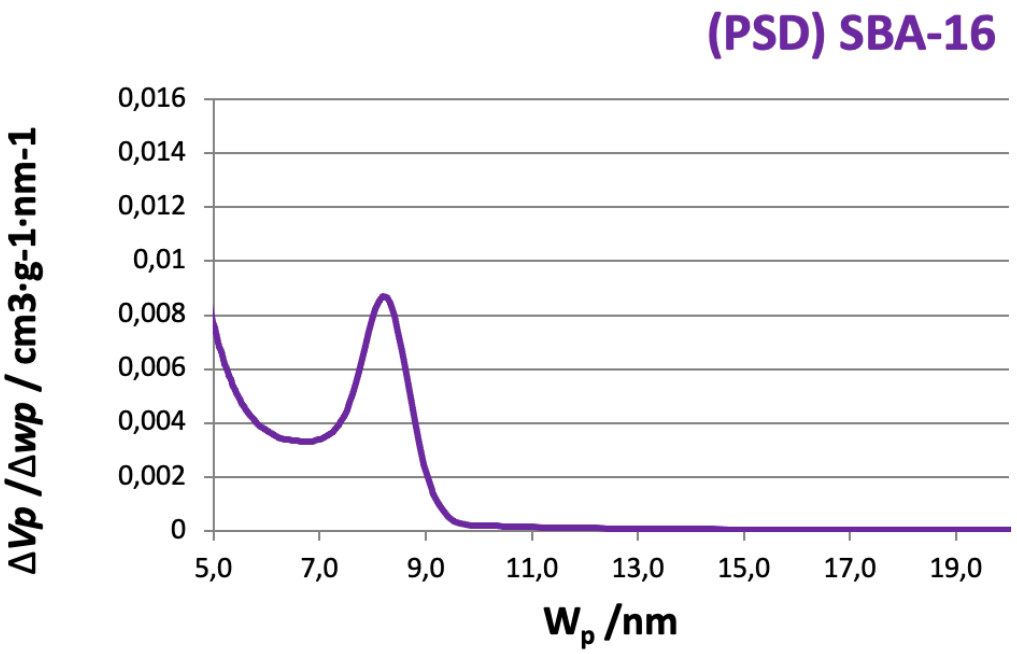

Figure 4. Pore size distribution of the SBA-16 material.

Figure 4 shows the pore size distribution of the MMO SBA-16 that was obtained using data from the adsorption branch. Said pore size distribution presents a uniform distribution of mesopore sizes, centered approximately at 8.1nm.

Infrared analysis by Fourier transform. (FTIR)

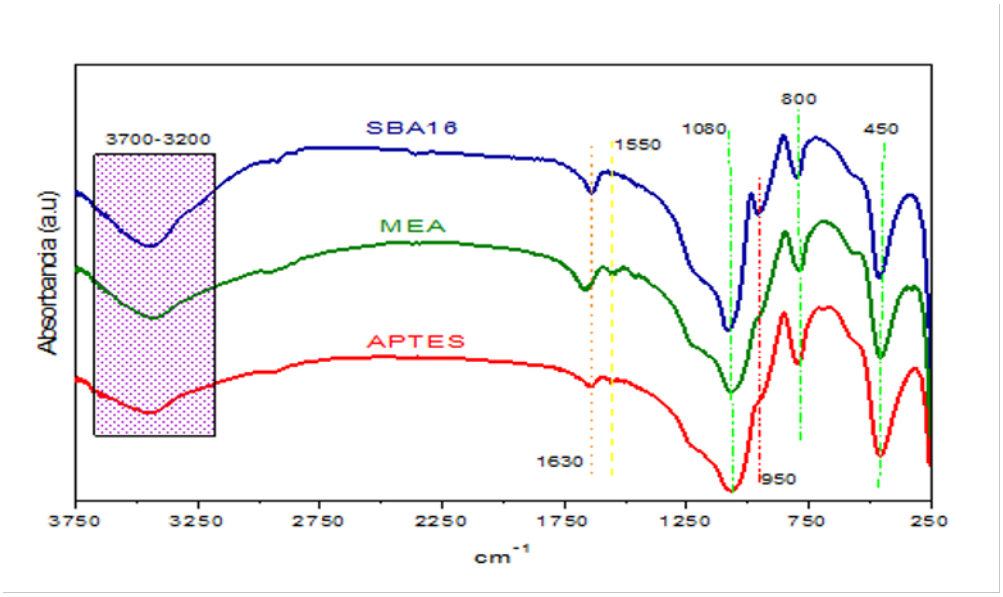

Figure 5. Infrared Spectrum of pure SBA-16 functionalized with MEA and APTES

Figure 5 shows the IR spectrum of the samples under study, where it can be seen that the stretching band of the bond of the Si-OH group (silanol group) located at 950cm-1 decreases after SBA-16 was functionalized with APTES and with MEA, indicating that in the functionalized materials the amino groups could be anchored in the –OH groups of the silanols.

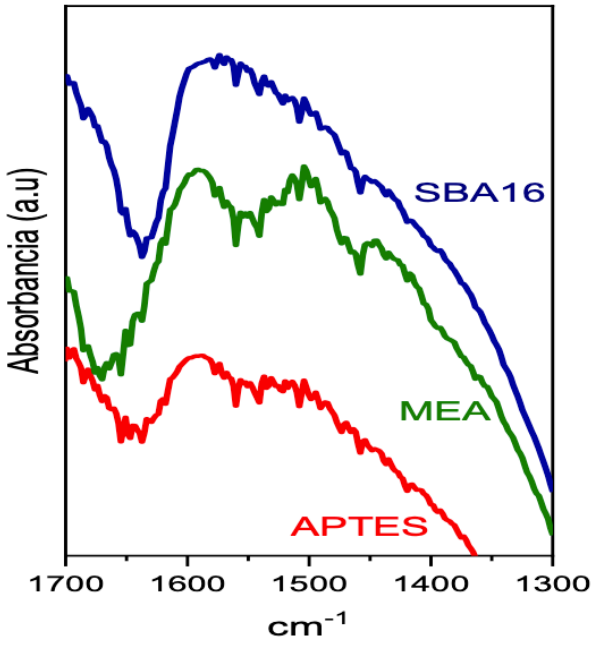

Figure 6. Representation of the band spectrum of the NH_2 amino groups.

The previously mentioned can also be observed in figure 6, since this spectrum (which is only from the region where the bands of the amino groups appear) we can observe that the functionalization of SBA-16 with MEA and APTES has been effective. due to the fact that in the functionalized materials the 1550cm-1 band appears, which is characteristic of amino groups $–NH_2$, where the one with the greatest intensity of said band is the SBA-16 functionalized with MEA, demonstrating a greater anchorage of amino groups with said reagent [6].

Modification of the surface of the central channel

In the bioanalytical stage, we developed a microfluidic immunosensor [5] in which the central channel (CC) was modified with the functionalized material SBA-16-MEA. This material was chosen as the nanoplatform since it presented a higher band intensity in FTIR and this confirms that more groups (NH2) were anchored in the SBA-16.

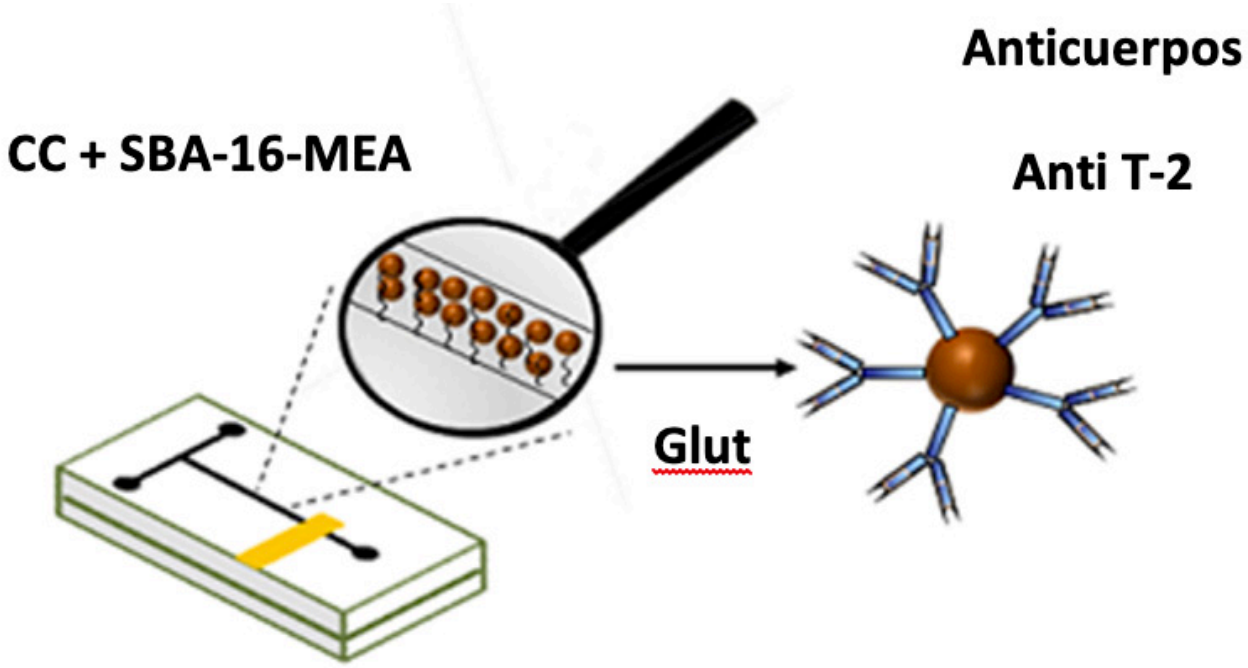

Figure 7. Central channel (CC) modification representation

Determination of mycotoxin T2 by commercial Elisa

A series of standards covering a concentration range from 0 to 400 µg kg-1, were provided by the RIDASCREEN®FAST ELISA Kit for T2 toxin. Thus, a calibration curve was built following the manufacturing protocol for spectrophotometry. The T2 toxin concentrations of the samples were determined using this commercial ELISA Kit and were detected spectrophotometrically by measuring the absorbance changes at 450 nm.

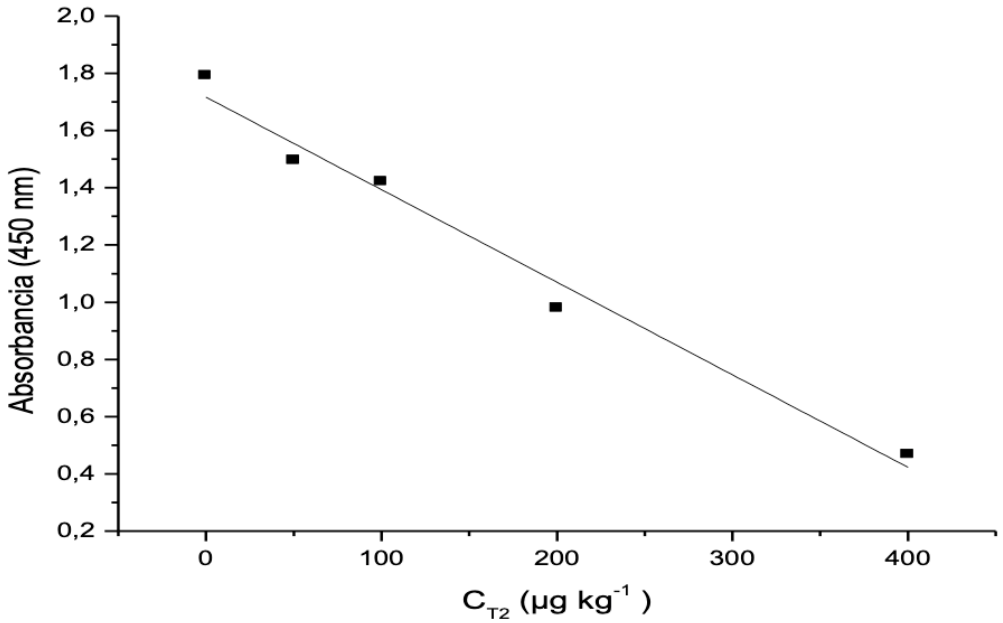

Figure 8. Calibration curve for the determination of T2 toxin by ELISA

In addition, the commercial ELISA was performed following the manufacturer's instructions. The absorbance changes versus the corresponding T2 toxin concentration were graphically represented in Figure 8. The linear regression equation was: A= 1.71 – 0.003* CT2 , with a linear regression coefficient r = 0.985 and a CV for the determination of 100 µg kg-1 of 6.78% T2 toxin (six replicates).

Determination of T2 toxin by amperometric analysis

A calibration curve was obtained to predict the concentration of T2 toxin present in the sample, which is linear in a concentration range of 0-400 µg kg-1. For its construction, the T2 toxin standards provided by the commercial ELISA Kit were used. The linear regression equation was: i = 214.50 – 0.46* CT2, with a linear regression coefficient r = 0.998, figure 9. The coefficient of variation (CV) for the determination of 100 µg kg-1 of T2 was less than 4 % (six replicates) with a Detection Limit of 0.05µg Kg-1. These results demonstrate that our microfluidic immunosensor can be used to quantify T2 toxin in unknown samples.

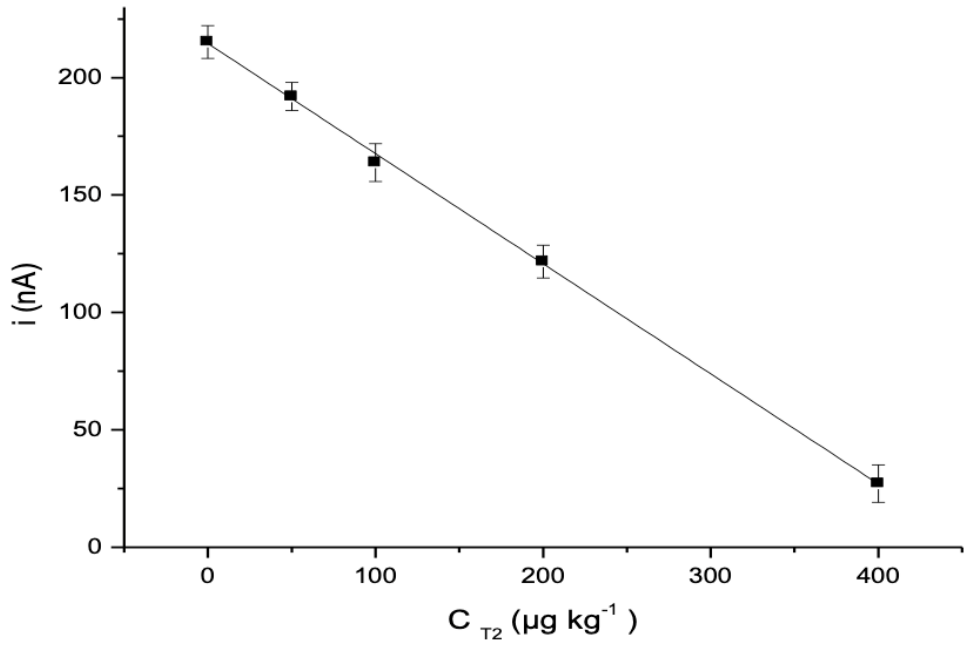

Figure 9. Curva de calibración para la determinación de T2 por el método amperométrico

Correlación con el método de ELISA comercial

The developed method was compared with the commercial spectrophotometric method for the quantification of T2 toxin in 20 samples of agri-food interest. The slope obtained was reasonably close to 1, indicating a good correlation between both methods Figure 10. Compared with the commercial ELISA, our method shows a significant increase in sensitivity, and this sensitivity is high enough to determine T2 toxin in unknown samples with very low levels of mycotoxin

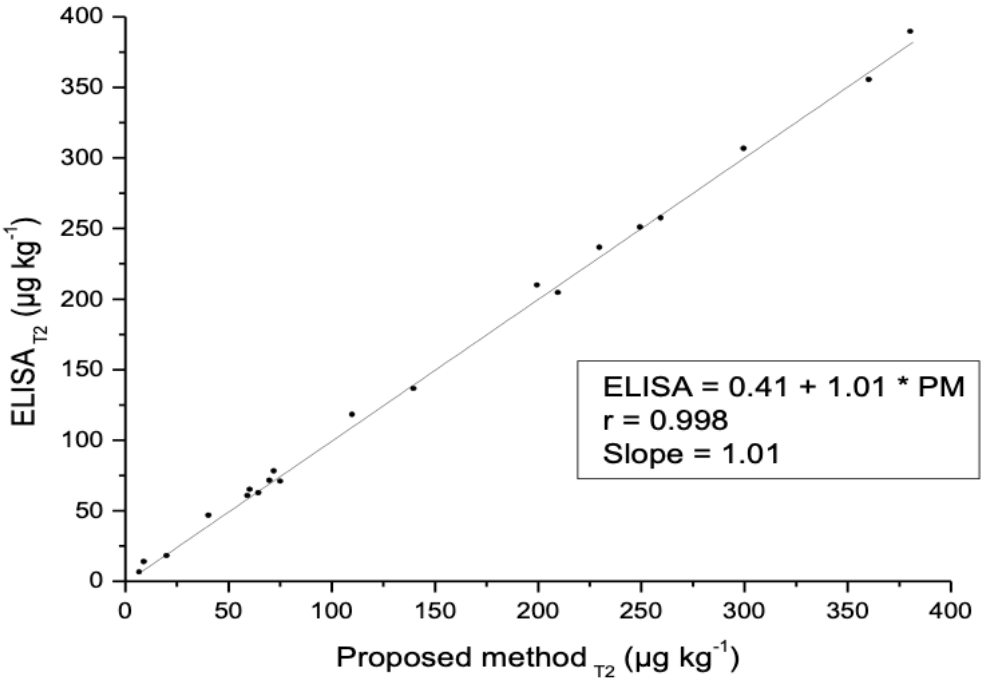

Figure 10. Correlación entre el método propuesto y el ensayo ELISA comercial

Conclusions

In this work, a microfluidic immunosensor coupled to a flow injection system with amperometric detection was developed to rapidly, sensitively and selectively quantify T2 toxin in samples of agri-food interest. The use of the selected nanoplatform modified with monoclonal anti-T2 antibodies allowed a significant increase in sensitivity without reducing selectivity, this being an important advantage. The increase in the reactive surface and the reduced diffusion distances of the present device allowed a total analysis time of 21 min, which was less than the time reported for the commercial ELISA Kit (40 min). In addition, this methodology, being a microfluidic-based device, minimized the cost of expensive reagents, showed physical and chemical stability, low background currents, a wide range of work potential and accuracy. Finally, we can propose this device as a possible analytical tool for its application in the agri-food industry in order to guarantee the safety and quality of these foods, as well as the health of consumers.

References

[1] 1- A. Turner, I. Karube, G. Wilson. Biosensors - Fundamentals and Applications, Oxford University Press: New York, USA, 1987, pp. 719-800.

[2] 2- A.I. Oliva Arias. Nuevas propiedades físicas de materiales nanoestructurados. Ingeniería Revista Académica, Universidad Autónoma de Yucatán, México 9, 2005, 39–46.

[3] 3- M. Regiart, O. Fernández, A. Vicario, J. Villarroel-Rocha, K. Sapag, G.A. Messina, J. Raba, F.A. Bertolino. Microchemical Journal. 141, 2018, 388-394.

[4] 4- A. Merkoçi, M. Pumera, X. Llopis, B. Pérez, M. del Valle, S. Alegret. Trends in Analytical Chemistry 24, 9, 2005, 826-838

[5] 5-Zanella R. (2012). Metodologías para la síntesis de nanopartículas: controlando forma y tamaño. Mundo Nano Vol. 5, No. 1, enero-junio, 2012. Recuperado el 17 de septiembre del 2020 de www.mundonano.unam.mx.

[6] 6-Silva, R. O., Freitas, J. C. R., Silva, M. F. R., Silva, P. C. B., Melo, E. J. M. V. C. F. y Freitas Filho, J.R.D. (2018). Development of decision-making competence in courses of spectrometric analysis of organic compounds. Educación química*, 29*, 35-47.

[7] 7-Faraldos, M., & Goberna, C. (Eds.). (2012). Técnicas de análisis y caracterización de materiales. Editorial CSIC Consejo Superior de Investigaciones Científicas.

[8] 8-"Adsoprtion by Powders and Porous Solids: Principles, Methodology andapplications",F. Rouquerol, J. Rouquerol, K.S.W. Sing,P.Llewwellyn and G.Maurin. AcademicPress 2014.

Bios

Alex Emmanuel Simioli

Alex Simioli carries out research in the field of volatile organic compounds (VOCs) and particulate matter, all related to atmospheric pollution and its determination using gas chromatography and mass spectrometry techniques. He has a master's degree in chemistry since 2022 from the National University of San Luis in which his final work was the determination of T2 toxin in samples of agri-food interest from a Biosensor. He has been a Chemical Analyst since 2015 from the National University of San Luis and since 2014 he has worked in the Environmental Measurements Laboratory at the Chemical Technology Research Institute (INTEQUI), which depends on the National University of San Luis and CONICET.

INSTRUCTIONS FOR AUTHORS

GUIDELINES

1. Length
Research reviews should not be less than 7000 words or more than 10,000 words (plus up to 15 figures and up to 50 references).

2. Structure
Whenever possible articles should adjust to the standard structure comprising:
(a) Graphical abstract,
(b) Abstract,
(c) Introduction describing the focus of the review,
(d) Article main body including assessment and discussion of available information (may be further subdivided),
(e) Conclusions,
(f) Bibliography.

3. Format
Authors must submit their articles in a Microsoft Word archive. Figures must be embedded in the article and also submitted in a separate .zip or .rar file.

4. References
References must be numbered in the text ([1] [2] [3]) and identified with the same numbers in the *References* section. Up to 50 references are allowed. The following are examples to take into account in each case.

BOOKS:
- *Single author*
Chung, R. *General Chemistry: Fundamental Knowledge,* 2nd ed.; McGuffin-Hill: Kansas City, 2003.
- *More than one author*
Chung, R.; Williamson, M. *General Chemistry: Fundamental Knowledge*, 2nd ed.; McGuffin-Hill: Kansas City, 2003.
- *Edited Book*
Kurti, F. Photodissociation and Reactive Scattering. In *The Rise of Chemical Physics*; White, AD, Ed.; Wilson: New Jersey, 2007; Vol. 128; p. 257.
- *Book in Series*
Goth, V. Polymer Chemistry. In *The Foundational Course in Organic Chemistry*; ACDC Symposium Series 1151; American Chemical Fraternity: Seattle, 2014; pp 123-149.
- *Article from a reference book*
Powder and Metallurgy. *Dictionary of Chemical Technology*, 3rd ed.; Wilson: New Jersey, 1971; Vol. 12, pp 68-82.
ARTICLES:
- *Article in a scientific journal*
Evans, A.; Stitch, M.; Smithers, ET; Nope, JJ Complex Aldol Reactions to the Total Synthesis of

Phorboxazole B. *J. Am. Chem*. Soc. 2012, 122, 10033-10046.
- Article in a popular/non-scientific magazine
Tatum, CJ Super Organics. *Wireless* , June 2001, pp 76-93.
- Article from an online journal
Turkey-Lopez, E. Inexact Solutions of the Quantum Double Square-Well Potential. *Chem. Ed.* [Online] 2007, 11, pp. 838-847. http://chemeducator.org/bibs/0011006/11060380lb.htm (accessed Aug 5, 2019).

PUBLICATION ETHICS

The journal considers that the primary objective of all submissions must be a contribution of relevant and appropriate content, and that all review processes must be structured based on that general criterion. Therefore, there is an emphasis on the concern to maintain the highest quality and ethics standards in the reception, evaluation and publication of articles. These standards include the three participants of the process: author, reviewer and editor.

1. Author's responsibilities

- Submitted manuscripts should maintain rigorous scientific criteria for data validation and conclusions.
- All data (Figures, Tables, etc.) reproduced from previous published articles must give the appropriate recognition to the source. Plagiarism is cause enough to reject the submission.
- Authorship must include all individuals who have contributed in a substantial way to the composition, prior investigation, and execution of the paper. Minor contributions must be acknowledged, but these contributors should not be listed as authors. The main author or authors of the article will make sure that all participants of the paper have approved the final version of the document submitted.
- All authors must reveal in their final manuscript any financial or other type of conflict of interests that might interfere with the results and interpretations in their research. All funding received to carry out the project must be acknowledged.
- After the article is published, in the event an author notices a crucial fault or inaccuracy, he or she should immediately report that fault or inaccuracy, so that an Erratum can be issued as soon as possible.

2. Reviewer's responsibilities

Reviewing is a time-consuming process that is carried out *ad honorem* by *bona fide* scientists conversant with the subject of the reviewed paper. The quality and the ethical standards of the journal depend critically on the quality of the reviewing process, and the following guidelines are established:

- All documents sent to the journal for review will be considered confidential documents and will not be discussed with external third parties.
- When invited, a potential reviewer should decline if: (a) the subject of the article is not within his/her area of expertise; (b) there is any kind of conflict of interest; (c) if the review cannot be finished within the period established by the journal.
- Any criticism or objections to the paper should be done in a neutral tone and based on reasonable grounds, not limited to simple opinions or purely subjective expressions.

3. Editor's responsibilities

- The editors are responsible for selecting the papers that will be published in the journal. The Editorial Management must comply with the ethical standards of the journal, as well as with all legal guidelines, including the prohibition of plagiarism and any other form of copyright infringement.
- The editors will evaluate and make decisions on the articles sent to the journal regardless of the

gender, sexual orientation, religious beliefs, ethnic origin, nationality or political ideology of the authors.

- Revealing information identifying reviewers is forbidden.
- The final version of all materials can be published only with the prior approval of their author.
- The editors will refrain from publishing manuscripts that imply a conflict of interests because of any possible connection with other institutions, companies and authors.
- Before deciding to send an article to a peer review, the editors are committed to thoroughly read all texts received and determine their appropriateness to the thematic universe of the journal.
- If a misbehavior or unethical action by an author or reviewer is identified, the editors must request the informer of such conduct or action to provide the evidence that may justify a possible investigation. All accusations will be handled seriously until reliable results are obtained regarding its truthfulness or falseness. If an investigation takes place, the editors are responsible for choosing the appropriate way in which it will be carried out. They can also request the advice and assistance from the Editorial Board, as well as from reviewers and authors.
- In the event a serious non-malicious mistake or a dishonest conduct by an author or a reviewer is proved, the editors shall act according to the nature and seriousness of the case. The actions the editors may take include, but are not limited to: notifying the author or reviewer of the existence of a serious mistake or misapplication of the ethical standards of the journal; writing a strong statement that reports and warns about a bad practice or unethical behavior; publishing that statement; unilaterally withdrawing the reported paper from the review or publication process; revoking the paper if it has already been published; communicating the journal's decision and the reasons behind it to the general public; and banning paper submissions by the people involved for a certain period of time.

PRIVACY STATEMENT

The names and email addresses entered in this journal site will be used exclusively for the stated purposes of this journal and will not be made available for any other purpose or to any other party.

ISSN 2683-9288

Science Reviews
from the end of the world

Centro de Estudios sobre Ciencia, Desarrollo
y Educación Superior
538 Pueyrredón Av. - 2° C – Second building
Buenos Aires, Argentina - C1032ABS
(54 11) 4963-7878/8811
sciencereviews@centroredes.org.ar
www.scirevfew.net